UNIVERSITAT POLITÈCNICA DE VALÈNCIA

DOCTORAL THESIS

EFFECT OF INLET CONFIGURATION ON THE PERFORMANCE AND DURABILITY OF AN AUTOMOTIVE TURBOCHARGER COMPRESSOR

PRESENTED BY:

MR. DANIEL TARÍ DE PACO

SUPERVISED BY:

DR. ROBERTO NAVARRO GARCÍA

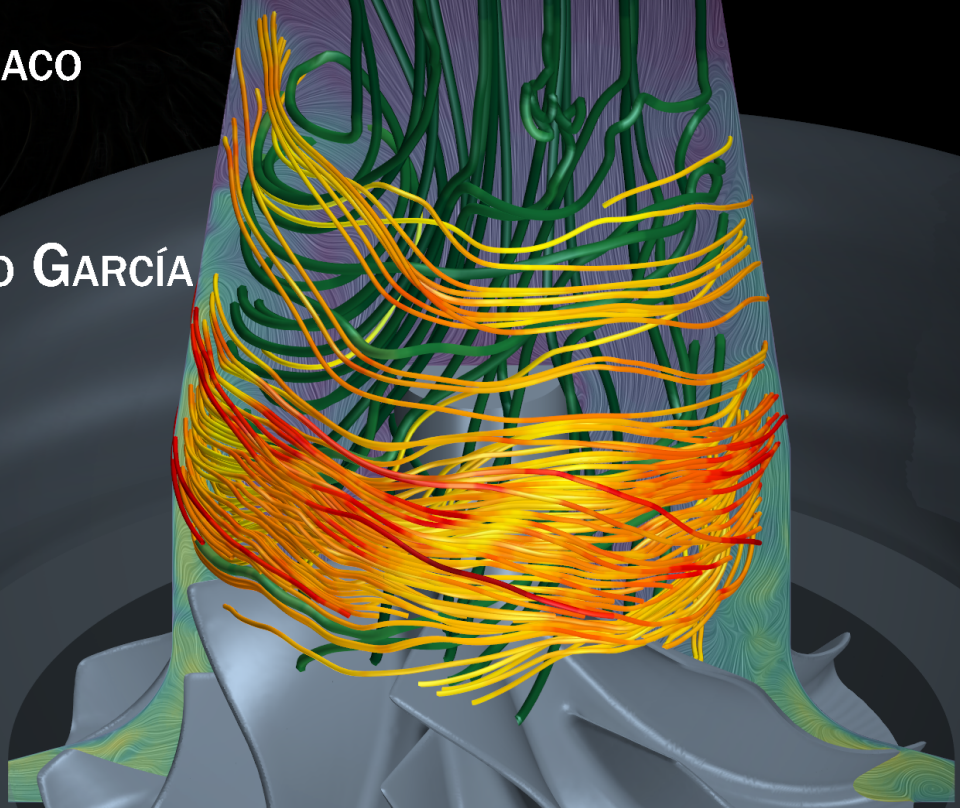

JUNE 2018

DEPARTAMENTO DE MÁQUINAS Y MOTORES TÉRMICOS

UNIVERSITAT POLITÈCNICA DE VALÈNCIA

Departamento de Máquinas y Motores Térmicos

DOCTORAL THESIS:

"Effect of inlet configuration on the performance and durability of an automotive turbocharger compressor"

Presented by: D. Daniel Tarí
Supervised by: Dr. D. Roberto Navarro

in fulfillment of the requirements for the degree of

Doctor of Philosophy

Valencia, June 2018

Doctoral Thesis

"Effect of inlet configuration on the performance and durability of an automotive turbocharger compressor"

Presented by: D. Daniel Tarí
Supervised by: Dr. D. Roberto Navarro

THESIS EXAMINERS

Dr. D. Antonio Arpaia
Dr. D. Mihai Mihaescu
Dr. D. Daniel Mira Martínez

DEFENSE COMMITTEE

Chairman: Dr. D. José Manuel Luján Martínez
Secretary: Dr. D. Oriol Lehmkuhl Barba
Member: Dr. D. Antonio Arpaia

Valencia, June 2018

Abstract

Popularization of turbochargers in internal combustion engines has been produced in the recent years due to a needful increase of awareness of pollutant emissions and their repercussion on the environment and the population. Pollutant emission regulations have tightened, causing techniques such Long Route Exhaust Gas Recirculation to operate under a wider range of operating conditions, with higher rates and even under very cold ambient conditions, which generates a potential problem of water condensation and compressor damaging. Additionally, the actual trend consisting in reducing the size of the engine to reduce fuel consumption, known as "downsizing", has caused the compressor to have to work close to the surge limit. Together with the aforementioned extension of LR-EGR usage range, these phenomena have induced an increase of the compressor design requirements, concerning durability and functionality. Both problems are governed by the geometrical configuration of the compressor inlet and can be, then, studied accordingly.

In this work, a predictive condensation model is proposed for being embedded in a computational fluid dynamics commercial code (STAR-CCM+). To allow a potential optimization of a given geometry, the model should introduce as low additional computational effort as possible, assuming certain limitations, though. For example, the characterization of water droplets is neglected. Once the model is implemented and verified, the results are compared with experimental data obtained from durability tests performed to assess the erosion of the compressor wheel under condensation generated by different LR-EGR T-joint configurations and operating conditions. After, the influence of the compressor on the mixing process and generation of condensates is addressed, proving that the simulation of the compressor can be decoupled from the T-joint numerical domain and reducing by two orders of magnitude the simulation time.

Concerning the impact of the inlet geometry on the surge margin and the other important compressor parameters, several simple geometries are proposed, and their influence is assessed. First, experimental tests performed on an engine test bench are carried out: steady measurements for obtaining efficiency and noise emission and transient tests for characterizing the surge limit. Then, 3D-CFD simulations are performed using similar geometries, studying the local phenomena that appear and proving thus the sensitivity of the inlet geometry to the surge margin and the performance of the compressor. It may

be highlighted the performance of the tapered duct, that produces a considerable positive shift of the surge margin without worsening the rest of the parameters and the convergent-divergent nozzle, which in addition to considerably improving the surge margin also enhances the isentropic efficiency of the compressor at low and mid mass flow rates. Nevertheless, the throat becomes a drawback at high mass flow rates, decreasing the compression ratio and efficiency under such conditions.

Keywords: Condensation; LR-EGR; CFD simulation; STAR-CCM+; Experimental validation; Surge margin

Resumen

La evidente generalización durante los últimos años del uso de turbocompresores en motores de combustión interna ha sido debida a un aumento necesario de la concienciación sobre las emisiones contaminantes y sus efectos sobre el medio ambiente y las personas. Las normativas sobre emisiones contaminantes se han endurecido, generalizando el uso de técnicas como la Recirculación de Gases de Escape de Ruta Larga bajo unas condiciones de operación más amplias, con una mayor tasa e incluso bajo condiciones ambiente frías, lo que ha generado potenciales problemas de condensación de agua y daño en el compresor. Además, la tendencia actual de reducir el tamaño del motor para reducir el consumo, llamada *"downsizing"*, ha provocado que el compresor tenga que funcionar muy cerca del límite de bombeo, lo que ha provocado, junto al descrito aumento de recirculación de gases de escape, una mayor exigencia en cuanto a durabilidad y funcionalidad del mismo. Los problemas comentados están claramente condicionados por la configuración geométrica de la entrada del compresor, ya sea por la condensación causada por los gases de escape al ser mezclados con aire fresco o por la influencia sobre el límite de bombeo y el resto de prestaciones.

En este trabajo se propone un modelo de predicción de condensación para ser integrado en un código comercial de mecánica de fluidos computacional (STAR-CCM+). Dicho modelo se plantea de forma que aumente en la menor medida posible el coste computacional, asumiendo ciertas limitaciones como la ausencia de caracterización de las gotas de agua. Una vez implementado, se contrastan los resultados frente a datos experimentales de ensayos de durabilidad: se correlacionan las predicciones del modelo frente al impacto de la condensación sobre el rodete del compresor en diferentes configuraciones geométricas y condiciones de operación. Posteriormente se estudia el impacto del propio compresor sobre el proceso de mezcla y la condensación, lo que permite después desacoplar el problema y reducir en dos órdenes de magnitud el tiempo de cálculo al poder obviar la simulación del compresor.

En cuanto a la influencia de la geometría en el margen de bombeo y resto de parámetros, se proponen varias geometrías sencillas y se analiza su impacto. Primero, se realizan ensayos experimentales en banco motor, tanto estacionarios para medir rendimiento y ruido como transitorios para definir el bombeo. Después, se ejecutan simulaciones CFD y se estudian los fenómenos locales que aparecen, en los que se evidencia una sensibilidad elevada de la geome-

tría sobre el margen de bombeo y el resto de parámetros. Se puede destacar el desempeño de la geometría de entrada cónica, que produce un aumento considerable del margen de bombeo sin repercusiones en el resto de condiciones de operación; y la tobera convergente-divergente, que aumenta el margen de bombeo pero, además, también aumenta ligeramente el rendimiento en el resto del mapa del compresor, aunque a costa de reducir moderadamente las prestaciones a alto gasto másico.

Resum

L'evident generalització durant els últims anys de l'ús de turbocompressors en motors de combustió interna ha estat deguda a un augment necessari de la conscienciació sobre les emissions contaminants i els seus efectes sobre el medi ambient i les persones. Les normatives sobre emissions contaminants s'han fet més restrictives, generalitzant l'ús de tècniques com la Recirculació de Gasos d'Escap de Ruta Llarga sota unes condicions d'operació més àmplies, amb una major taxa i fins i tot sota condicions ambient fredes, fet que ha generat potencials problemes de condensació d'aigua i danys al compressor. A més, la tendència actual de reduir la grandària del motor per millorar el consum, anomenada *"downsizing"*, ha provocat que el compressor haja de funcionar molt a prop del límit de bombeig, fet que ha provocat, junt amb el descrit augment de recirculació de gasos d'escap, una major exigència quant a la seua durabilitat i funcionament. Els problemes esmentats estan clarament condicionats per la configuració geomètrica de l'entrada del compressor, ja siga per la condensació causada pels gasos d'escap al ser barrejats amb aire fresc o per la influència sobre el límit de bombeig i la resta de prestacions.

En aquest treball es proposa un model de predicció de condensació per a ser integrat en un codi comercial de mecànica de fluids computacional (STAR-CCM+). Dit model es planteja de manera que augmente en la menor mesura possible el cost computacional, assumint certes limitacions com l'absència de caracterització de les gotes d'aigua. Una vegada implementat, es contrasten els resultats enfront de dades experimentals d'assajos de durabilitat: correlacionen les prediccions del model enfront de l'impacte de la condensació sobre el rodet del compressor en diferents configuracions geomètriques i condicions d'operació. Posteriorment, s'estudia l'impacte del mateix compressor sobre el procés de barreja i la condensació, cosa que permet després desacoblar el problema i reduir en dos ordres de magnitud el temps de càlcul, ja que pot obviar-se la simulació del compressor.

Quant a la influència de la geometria en el marge de bombeig i la resta de paràmetres, es proposen diverses geometries senzilles i s'analitza el seu impacte. Primerament, es realitzen assajos experimentals en banc motor, tant estacionaris per mesurar rendiment i soroll com transitoris per definir el bombeig. Després, s'executen simulacions CFD i s'estudien els fenòmens locals que apareixen, en els quals s'evidencia una sensibilitat elevada de la geometria sobre el marge de bombeig i la resta de paràmetres. Es pot destacar el rendi-

ment de la geometria d'entrada cònica, que produeix un augment considerable del marge de bombeig sense repercussions en la resta de condicions d'operació; i la tovera convergent-divergent, que augmenta el marge de bombeig però, a més, també augmenta lleugerament el rendiment en la resta del mapa del compressor, encara que a costa de reduir moderadament les prestacions a alt flux màssic.

List of publications

This thesis is based on the work contained in the following papers:

[1] J. R. Serrano, P. Piqueras, R. Navarro, D. Tarí, and C. M. Meano. "Development and verification of an in-flow water condensation model for 3D-CFD simulations of humid air streams mixing." *Computers & Fluids* 167 (2018), pp. 158 –165. ISSN: 0045-7930. DOI: 10.1016/j.compfluid.2018.02.032

[2] J. Galindo, P. Piqueras, R. Navarro, D. Tarí, and C. M. Meano. "Validation and sensitivity analysis of an in-flow water condensation model for 3D-CFD simulations of humid air streams mixing." *Manuscript submitted to scientific journal* (2018)

[3] J. Galindo, R. Navarro, D. Tarí, and G. García. "Centrifugal compressor influence on condensation due to Long Route-Exhaust Gas Recirculation mixing." *Manuscript submitted to scientific journal* (2018)

[4] J. Galindo, A. Tiseira, R. Navarro, D. Tarí, and C. M. Meano. "Effect of the inlet geometry on performance, surge margin and noise emission of an automotive turbocharger compressor." *Applied Thermal Engineering* 110 (2017), pp. 875–882. DOI: 10.1016/j.applthermaleng.2016.08.099

[5] J. Galindo, A. Gil, R. Navarro, and D. Tarí. "Analysis of the impact of the geometry on the performance of an automotive centrifugal compressor using CFD simulations." *Manuscript submitted to scientific journal* (2018)

Division of work between authors

The work leading up to this thesis was done in collaboration with other researchers. The respondent is the corresponding author of all papers on which this thesis is based (author signatures are in order of seniority). The respondent produced the set-up and post-processing of the compressor CFD simulations and the set-up and post-processing methodologies concerning the condensation model simulation, however Guillermo García is acknowledged for the processing of the cases exposed in Chapter 3 and Rubén Ibáñez is acknowledged for the help during the implementation of the condensation model. The respondent also participated in the experimental campaign performed on an engine test bench regarding the compressor inlet geometry and in a portion of the compressor wheel erosion durability tests performed in a continuous flow turbocharger tests bench. Methodology and results discussion were performed in collaboration with supervisor Dr. Navarro, Prof. Galindo and rest of co-authors.

Other publications by the respondent

The following are publications in which the respondent has been involved during his doctorate studies, but are not included in the thesis. These contributions deal with the development of a compressor map extrapolation model, which covers both the compression ratio and the efficiency parameters.

[6] J. Galindo, R. Navarro, L. M. García-Cuevas, D. Tarí, H. Tartoussi, and S. Guilain. "A zonal approach for estimating pressure ratio at compressor extreme off-design conditions." *International Journal of Engine Research* (2018). DOI: 10.1177/1468087418754899

[7] J. Galindo, A. Tiseira, R. Navarro, D. Tarí, H. Tartoussi, and S. Guilain. "Compressor Efficiency Extrapolation for 0D-1D Engine Simulations." In: *SAE Technical Paper*. SAE International, Apr. 2016. DOI: 10.4271/2016-01-0554

[8] J. Galindo, R. Navarro, L. M. García-Cuevas, and D. Tarí. "An approach for extrapolating turbocharger compression ratio maps for engine simulations." In: *Mathematical modelling in engineering and human behaviour 2015*. Ed. by L. Jódar, L. Acedo, J. C. Cortés, and F. Pedroche. 2015

Acknowledgments

In first place, I wish to thank Dr. Roberto Navarro for sharing his knowledge and guidance through the sinuous path that has been this thesis. Also for his endless patience with my off-topic comments and the mechanical clicky noises. I wish to thank CMT-Motores Térmicos and Universitat Politècnica de València for this great opportunity, as well.

I wish also acknowledge Prof. Galindo for enlighten the genesis of this research with his expertise and great imagination and Dr. Piqueras for introducing me the psychrometric side of combustion engines and the engineering of scientific publications. I would like to thank Cesare Meano for his thorough help and to his Advance Engineering team at GM for a very nice stay in Torino.

Special thanks to the people that have helped and allowed the completion of the different tasks this thesis covers: Vicente Boronat, Álvaro Zahinos and Alejando Hernández, in charge of the experimental tests; Rubén Ibáñez help with the implementation of the model; and Guillermo García with the assessment of the compressor influence on the condensation process. I wish also like to thank all the technicians, administration staff and maintenance people in charge of moving this institute on and on.

Many thanks to my friends as well, for joining and pushing me through this journey: Manu, Alberto, Ausias, Julián, Pablo (mi Pablo), Magui, Artem and Auñon a.k.a. the poliamigxs; Carlos, Javi, Iván, Aitor and Mónica (lxs 5+1); and, of course, the smartest (and my personal) psychologist, Andrea.

I would also like to mention my former roommates Antonio and Jorge for their support, Alba and Mari for proving that days can have more than 24 hours and finally, *The Telekolectiv* for adopting and introducing me into the Balkan world, opa!

And, of course, to my parents and sister, to whom I owe everything, I am infinitely grateful.

Valencia, June 2018.

"Every journey is a series of choices. The first is to begin the journey."

Antichamber.

Contents

List of Tables

List of Figures

List of symbols

Latin characters

a	speed of sound	$m \cdot s^{-1}$
c	absolute velocity	$m \cdot s^{-1}$
c_p	isobaric specific heat capacity	$J \cdot kg^{-1} \cdot K^{-1}$
D	diffusion coefficient	$m^2 \cdot s^{-1}$
f	additional terms	
fr	frequency	Hz
h	enthalpy	$J \cdot kg^{-1} \cdot K^{-1}$
I	sound intensity	$W \cdot m^{-2}$
i	incidence angle	$\circ$
L	latent heat	$J \cdot kg^{-1}$
l	characteristic length	m
M	Mach number	$-$
MW	molecular weight	$kg \cdot mol^{-1}$
$\dot{m}$	mass flow rate	$kg \cdot s^{-1}$
N	compressor rotational speed	rpm
p	pressure	bar
RH	relative humidity	%
r	radial coordinate	m
S	source term	
St	Strouhal number	
T	temperature	K
t	time	s
U	characteristic velocity	$m \cdot s^{-1}$
u	blade linear velocity	$m \cdot s^{-1}$
$\vec{u}$	velocity	$m \cdot s^{-1}$
V	volume	m^3
$\vec{v}$	velocity	$m \cdot s^{-1}$
W	compressor specific work	$J \cdot kg^{-1}$
w	relative velocity	$m \cdot s^{-1}$
w	specific humidity	$g_{H_2O} \cdot kg_{air}^{-1}$
x	coordinate in dominant direction	m
Y	mass fraction	

Greek characters

α	thermal diffusivity	$m^2 \cdot s^{-1}$
α	angle made by absolute velocity with the axial plane	
β	angle made by relative velocity with the axial plane	
Γ_φ	generic variable	
γ	ratio of specific heats	$-$
Δt	characteristic time	s
ϵ	relative difference	%
η	compressor efficiency	%
ν	kinematic viscosity	$m^2 \cdot s^{-1}$
$\Pi_{t,t}$	total-to-total pressure ratio	$-$
ρ	density	$kg \cdot m^{-3}$
φ	generic variable	
ω	rotational speed	$rad \cdot s^{-1}$

Sub- and Superscripts

$\hat{}$	normalized variable
0	stagnation variable
0	mean variable
a	axial component
abs	absolute
air	dry air
$back$	backward travelling wave
c	compressor
$comp$	complete
egr	egr flow
$ener.$	energy
$forw$	forward travelling wave
H_2O	liquid water
i	x,y,z cartesian components
in	intake flow
ind	inducer
$l.e.$	leading edge
m	mass
mix	mixing flow
$mom.$	momentum
out	outlet flow

p	momentum
red	reduced
ref	reference value
rel	relative
s	isentropic
sat	saturation
t	thermal
t	stagnation variable
u	tangential component
v	viscous
vap	vapor component
water	liquid water
ν	viscous

Acronyms

0D	zero dimensional
3D	three dimensional
A/T	After treatment
BEP	Best efficiency point
BSFC	Break specific fuel consumption
C, Conv	Convergent
C-D	Convergent-divergent
CAD	Computer-aided design
CFD	Computational fluid dynamics
CI	Compression ignited
CO	Carbon monoxide
CO_2	Carbon dioxide
DOC	Diesel oxidation catalyst
DPF	Diesel particulate filter
ECU	Engine control unit
EGR	Exhaust gas recirculation
HC	Hydrocarbon
ICE	Internal combustion engine
IGV	Inlet guide vanes
LDV	Laser doppler velocimetry
LES	Large eddy simulation
LIC	Line integral convolution
LR-EGR	Long-route EGR

MoC	Method of Characteristics
NO_x	Mono-nitrogen oxides
PIV	Particle image velocimetry
PSD	Power spectral density
RANS	Reynolds-Averaged Navier-Stokes
RH	Relative humidity
RO	Rotating order
SCR	Selective catalytic reduction
SI	Spark ignited
SIL	Sound intensity level
SPL	Sound Pressure Level
SR-EGR	Short-route EGR
Str.	Straight
Tap.	Tapered
TC	Turbocharger
VGT	Variable geometry turbine

Chapter 1

Introduction

Contents

1.1 Motivation

The will of having a greater freedom and autonomy has been pursued by mankind since the invention of the wheel. The creation of the automobile in Germany circa 1885 implied a revolution in how the world was perceived. The environment was severely modified for suiting the newborn technology. Millions of jobs became obsolete and many others were created. Industry, trading and even leisure activities changed, spectacularly shrinking the known universe. Since that moment, thousands of millions of combustion engine-powered automobiles have been made in the whole world. Only in 2016 around 95 million vehicles were produced, resulting in a total of around one billion vehicles in circulation.

However, Internal Combustion Engines (ICEs) are not only employed in automobiles. Flexibility of combustion engines is well known and widely established. They are used in both particular and industrial applications, from low power requirements, such as light motorbikes or gardening tools, to very high power structures, like container ships, large aircraft engines, uninterruptible power supply units for hospitals or airports, etc. The list of applications is endless. The popularity of these engines is granted by the versatility of the conversion from chemical energy to mechanical power, and if needed, to electric energy. Moreover, automotive fuels present energy densities only beaten by nuclear fuels, which, to date, has given vehicles that use this technology an unmatched autonomy.

A significant step ahead was introduced by adding forced-induction systems to the engines. This consists in filling the cylinders with air at a higher pressure and density than ambient conditions, which is achieved by adding some kind of compression stage in the intake line. Among the different types of compressors that exist, the most popular configuration for light automotive vehicles is the centrifugal compressor. It is usually connected through a shaft with a radial turbine from where the energy is taken, enhancing the global thermal efficiency of the engine, forming a device known as turbocharger.

The turbocharger was invented by Alfred Büchi, a Swiss engineer in charge of the engine diesel research at Gebrüder Sulzer, an engine manufacturer company. However, it took Büchi and his team near twenty years to successfully develop this technology and pairing it to a diesel engine. Parallel but independent progress was also made by Auguste Rateau and Sanford Alexander

Moss, who managed to fit a turbocharger to aircraft engines, compensating the decrease of air density at high altitude and setting a turning point in air navigation. In the 1920s, production aircrafts, ships and locomotives equipped with turbocharged engines start appearing. However, it was only a few decades ago, around the 1980s when passenger cars began incorporating the turbochargers to their engines, being their complete popularization even more recent; first among Compression Ignited (CI) engines, around twenty years ago, and then among Spark Ignited (SI) engines, about a decade ago. Turbocharged engines were a key factor for improving the specific power and efficiency of the vehicles, especially when combined with a reduction of the cylinder displacement. The synergy produced by this combination is known as "downsizing", a trend that has been popularized during the last years.

However, coupling two different mechanical devices, as are a reciprocating engine with a continuous flow turbocharger, does not come exempt of drawbacks, especially in applications where there may be a wide range of operating conditions, such as in automobiles. The main inconvenient that affects the performance and controllability of the system is the so called turbo-lag [9]. This is the delay between the driver demand of an increase of power and the response of the turbocharger to meet the conditions to actually provide the requested power. Since there are no mechanical constraints between both devices, the exhaust gases need to accelerate the turbocharger wheel against its inertia, friction and compression load, primary contributors of the turbo-lag.

Although turbochargers have been used for about a century, with the recent downsizing trend they have become an essential component of the current generation of engines, appearing even configurations with multiple stages of compressors and turbines. The low-end torque request has tightened the operating range of the compressor towards low mass flow rates and high boosting pressure, i.e. closer to the surge line [10]. This is a stability limit where the adverse pressure gradient in the impeller of the compressor is so high that the flow detaches and backflows appear, suddenly decreasing the compression ratio and the mass flow and producing an oscillating phenomenon. During this oscillation, the wheel suffers damaging axial loads and the efficiency drops. In the past years, special effort has been made in pushing the surge limit, either with active control [11] or passively by modifying the geometry of the system [12].

Due to the relaxed emission regulations and the reduced awareness on this topic of both consumers and manufacturers in the near past, pollution levels

have been increased causing a harmful impact on the health of all living creatures in general and lowering the quality of life of humans in particular, also accelerating the climatic change [13]. Fortunately, in the recent years, measures against the emission of pollutant gases have been tightened and vehicle manufacturers have invested in and investigated about improving different techniques to reduce these noxious gases that are released to the ambient. On the one side, carbon dioxide (CO_2) is a greenhouse gas, product of a proper combustion of hydrocarbon fuels, thus its reduction is bonded to an increase of the global efficiency of the vehicle power-train. For this, the most popular trend followed by engine manufacturers in the past years is the aforementioned downsizing. By reducing the cylinder displacement, and even in some cases the number of cylinders, the engine becomes lighter and the mechanical losses decrease [14]. Additionally, operating points at low engine speeds, where traditionally increased emissions were produced, are moved towards better efficiency regions. Other techniques used for improving the efficiency of the vehicle consist on introducing the usage of an electric-hybrid powertrain, stopping the engine during short stops, lightening up the weight of the car, etc.

On the other side, each engine family (CI and SI) generates additional subproducts during the combustion, depending on the thermodynamic conditions of the process. Carbon monoxide (CO), unburnt hydrocarbons (HC) and nitrogen oxides (NO_x) are produced by SI engines and dramatically decreased by catalytic converters [15]. In CI engines, critical pollutant emissions are soot and NO_x. The former is usually captured in particulate filters (DPFs) and then burnt when the accumulation reaches a certain threshold [16]. NO_x emissions, which are responsible of acid rain and may potentially damage lung tissue, can be addressed by avoiding their generation during combustion (active measures) or by removing them with after-treatment techniques (passive measures). In a Selective Catalytic Reduction (SCR) system, ammonia is injected into the exhaust stream, which reacts with the NO_x and produces N_2, CO_2 and water. However, this aforementioned device increases the engine production cost and has other disadvantages [17]. An approach for directly avoiding the formation of NO_x is to mix exhaust gases with fresh air upstream of the cylinders, which reduces the maximum temperature without adding additional oxygen. This technique is called Exhaust Gas Recirculation (EGR) and in spite that it has been used for more than 40 years [18], it has not ceased evolving since its appearance. The main scope of application of EGR systems are CI engines, even though using EGR in turbocharged SI engines is also beneficial [19, 20].

It has been widely employed with different routing [21], depending on where the gases are taken from. Studies about the advantages and drawbacks of each alternative have been made by authors such Ladommatos et al. [22] and Cornolti et al. [23]. At CMT-Motores Térmicos analogous researches were made by Desantes et al. [21] and Luján et al. [24].

The most common configuration consists in connecting both outlet and inlet manifolds, resulting in the so-called high-pressure or Short Route EGR (SR-EGR). Using this connection, a cooler and a valve to control the mass flow rate are usually employed. This system has been very popular during the last decades due to its simplicity. However, as it will be explained below, it introduces some drawbacks which are partially avoided by using the Long Route EGR (LR-EGR), which consists in extracting part of the low-pressure gases downstream the turbine and DPF and reintroducing them before the compressor.

The main practical difference between these two EGR configurations resides in the mass flow going through the turbine and the compressor. As the SR-EGR valve opens, the flow passing through the turbocharger is reduced, shifting the working point towards generally lower efficiency values and reducing the compressor surge margin, hence requiring a selection of turbomachinery that withstands good performance over a wide range of operating conditions. In addition, lowering the turbine mass flow implies reducing its power, worsening its transient response as stated by Desantes et al. [21]. Conversely, with LR-EGR the turbine mass flow rate is not directly affected by the valve opening. From the point of view of air charge, the SR-EGR loop leads to an increase in the intake manifold temperature, which has a negative effect on Brake Specific Fuel Consumption (BSFC) (see Ladommatos et al. [22] and Desantes et al. [21]). Finally, a relevant aspect of the engine performance is the cylinder-to-cylinder EGR distribution. SR-EGR system may not be able to uniformly distribute EGR gas between the cylinders because the EGR outlet duct discharges over the inlet manifold [25], and the flow may not have enough time to be mixed with fresh air, thus entailing an increase in NO_x and particulate matter emissions [26]. This phenomenon is responsible for possible dis-uniformities of charge among cylinders [24]. On the opposite hand, LR-EGR mixes both flows far upstream the cylinders, letting a perfect distribution of the EGR gas between them.

Hence, the LR-EGR may look like a better solution although it is not without drawbacks [21, 23, 27]. Firstly, it presents a higher design complexity

since inlet and outlet connections are relatively far from each other, meaning longer ducts within the underhood. In addition, the volume of the whole ducting implies a transient buffer of exhaust gas mass flow, which may decrease EGR demand responsiveness. The addition of the EGR discharge upstream the compressor produces a geometry modification that may impact on the compressor performance, as studied previously by Serrano et al. [28].

Moreover, the humidity of the exhaust gases is prone to condense in different points of the system when their temperature falls below dew conditions. Main regions where condensation is produced are: at the interior walls of the LR-EGR cooler (especially during a cold start of the engine) and at the T-joint where the exhaust gases are reintroduced to the intake line, right upstream of the compressor. The latter condensation mechanism, opposed to the cooler wall condensation, imply inflow condensation, a phenomenon that has not been as explored as the former one. Nevertheless in both cases the problem appears when the water droplets reach the compressor and impact against the impeller, which is usually rotating at high speeds, causing erosion on it and posing at risk the durability and integrity of the whole turbocharger.

In spite of recent progress in emission reduction technologies, there is a lack of a complete effectiveness due to the slow retirement of the vehicles with obsolete emission control. In Table 1.1, the European emission control standards concerning CO, HC, and NO_x for CI engines is showed. The pronounced tightening of the NO_x is clear, following a progressive reduction to less than one fifth of the initial value. In Fig. 1.1 it is shown which portion of the vehicles in operation of Spain [29] was manufactured under each European emission regulation. It is noticeable that more than half of the vehicles were made under the Euro III regulation or before, and only a fourth comply with Euro V or VI.

The problem faced in this thesis comprises the inlet of the compressor where, as aforementioned, different phenomena take place. On the one side, the aerodynamic pattern given by the inlet geometry affects the performance of the compressor, especially at low mass flow rates where tightening demands are required. On the other side, the LR-EGR discharge, which inherently modifies the inlet geometry, may trigger the generation of condensates, which as aforementioned, may become an issue in terms of impeller durability.

Emissions standard	**Year**	**CO**	**HC+NO_x**	**NO_x**
		(g/km)	(g/km)	(g/km)
Pre-Euro I		-	-	-
Euro I	1994	2.72	0.97	-
Euro II	1997	1	0.7	-
Euro III	2001	0.66	0.56	0.5
Euro IV	2006	0.5	0.3	0.25
Euro V	2010	0.5	0.23	0.18
Euro VI	2015	0.5	0.17	0.08

Table 1.1: European emission standards for CI engines.

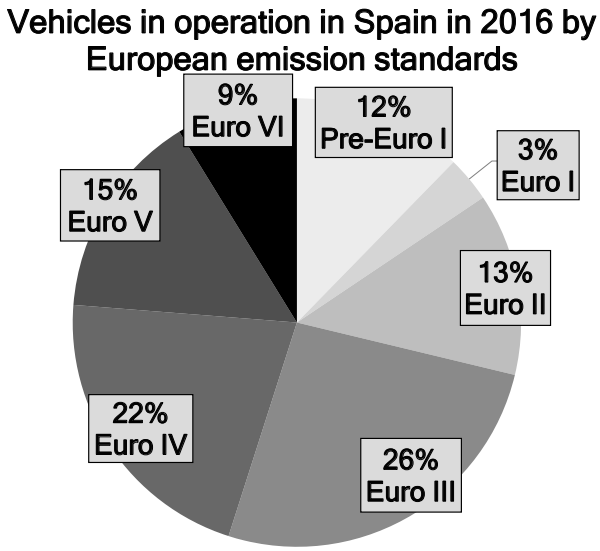

Figure 1.1: VIO of Spain [29].

1.2 Background

Several fields of study are explored for considering a complete view of the phenomena involved in the current work. A summary of the highlighted investigations checked prior to the development of the proposed approach is described next.

Concerning condensation, many authors have focused on this phenomenon being produced on the walls due to the widespread situations where a cold

surface is responsible of it. Kim et al. [30] and Panday et al. [31] performed studies about condensation in tubes for intercooling applications and Liu et al. [32], Vyskocil et al. [33] and Shang et al. [34] researched about free stream wall condensation. Important progress was made by Moses et al. [35] and later by Grubel et al. [36] on inflow condensation, however in those cases condensation was being caused by a drop in temperature when the gas was accelerated in a de Laval nozzle, implying velocities significantly higher than common velocities inside a LR-EGR mixing T-joint. Condensation in EGR systems has been studied by several authors. Abarham et al. [37] and Warey et al. [38] focused on the deposits left after condensing, studying how the efficiency of the cooler was affected and how to remove them using water vapor exempt of HC. Bourgoin et al. [39] and Moroz et al. [40] focused on the corrosion generated by the acidic components of the exhaust gases using both diesel and biodiesel fuels, obtaining similar results of condensation rate and acidity. At CMT-Motores Térmicos, Serrano et al. [41] proposed a 0D psychrometric model to quantify the worst case scenario in terms of condensation given a certain ambient and engine operating conditions, considering potential condensates in both the cooler and the later mixing with fresh air. Moreover, Serrano et al. [41] conducted experimental tests to analyze the impact of condensation in the LR-EGR line on the erosion of the compressor wheel, additionally providing the experimental setup methodology used in this current thesis (see section 2.5). Other authors, such as Castorrini et al. [42] and Koka et al. [43] also studied the damage caused by water droplets on rotating blades using numerical simulations, the latter analyzed the protectiveness capacity of a ceramic coating, comparing experimental erosion tests with a predictive numerical model. However, the droplet distribution on the inducer was imposed, not depending on the configuration upstream of the compressor. Surendran et al. [44] studied the impact of compressing humid air, as would be the case when using LR-EGR.

Regarding the compressor operation, researches have been widely studied for decades, being the surge limit one of the most addressed topics. Surge consists in a pulsating oscillation of the flow produced when the pressure gradient in the compressor exceeds the centrifugal forces of the impeller [45]. Huppert [46], Fink et al. [47] and Willems and De Jager [48] studied different surge mechanism that appear depending on several factors. It is possible to shift the surge limit against lower mass flow rates by modifying certain elements of the compressor or by adding *ad hoc* components for this purpose. Epstein et al. [49] and Gravdahl et al. [50] proposed to generate acoustic waves

to counteract surge oscillations, delaying its onset. Sundtröm et al. [51] studied the influence of the compressor housing treatment, paying special attention on the emitted noise. Zamiri et al. [52] and Shahin et al. [53] analyzed a compressor with diffuser vanes, however this technique is mostly used for large compressors.

Different authors have confirmed the noticeable influence of the intake compressor geometry on its performance [54]. Even the actual piping configuration used under the hood of a manufactured vehicle may differ from the data obtained in a continuous flow test bench, as seen by Capon and Morris [55] and by Baris and Mendonça [56]. At CMT-Motores Térmicos, experimental tests and CFD simulations have been carried out about different inlet configurations. Serrano et al. [28] modeled and tested a set of 90° elbows upstream the compressor inlet, obtaining in most of the cases a negative impact on compression ratio but a beneficial surge shift. Galindo et al. [57] proposed adding a pre-whirl device embedded in a 90° perpendicular elbow, seeking to counteract the drawbacks of having a regular elbow. Lang [58] and Galindo et al. [59] studied the influence of an elbow, a volume (with both a step and a tapered duct at the end) and a resonator on the surge line and the compressor map, first with computational models and then through experimental tests, obtaining noticeable benefits mainly on the surge line. Finally, the in-house background regarding the geometry of the compressor inlet ends with the study made by Desantes et al. [60] about the incorporation of a convergent-divergent nozzle right upstream the compressor inducer. The compressor map was heavily modified towards lower mass flow rates, increasing the surge margin up to a 30%, and a higher compression ratio and an increase in compressor efficiency were found at low and mid mass flow rates. Conversely, for high mass flow rates, the pressure drop introduced by the area restriction produced a considerable worsening of the compression ratio and compressor efficiency.

Several experimental facilities and measuring apparatus were required during the development of this thesis. Luckily, at CMT-Motores Térmicos top notch instrumentation and detailed documentation were available to fulfill all of the different needs regarding the experimental section. A turbocharger can be characterized mounted on an engine test bench [59, 61] or isolated in a continuous flow rig [62, 63]. Each approach is suitable for different purposes. For example, a steady flow rig allows a better control of the turbocharger parameters such speed, mass flow and compression ratio, becoming optimal for measuring compressor maps. However, the actual behavior slightly differs

when mounted in a real engine [59], so that in some occasions it is more interesting to use an engine test bench to characterize the compressor. In the latter case, compressed air may be injected in the intake manifold, adding a degree of freedom that allows measuring the compressor map with ease [61]. It is also possible to reproduce pulsating flow on a steady flow test bench using rotating valves, as studied by Galindo et al. [64]. For measuring the noise generated in the compressor, it is possible to either use a directional microphone at the intake orifice or by decomposing the acoustic waves with an in-duct three-sensor array, as described by Broatch et al. [65] and Torregrosa et al. [66]. Finally, a turbocharger steady flow test bench can be modified to simulate EGR conditions and allow the possibility of condensing water in the EGR cooler or in the EGR T-joint. For this, Serrano et al. [41] proposed deriving part of the hot and compressed air used to feed the turbine and inject a certain amount of water, depending of the desired specific humidity for the EGR gas. Finally, the humid gas is cooled down and reintroduced upstream of the compressor, in a T-joint.

Both main topics covered in this thesis are approached both experimentally and through CFD simulations. For a development of a proper CFD methodology, many background works and studies were addressed. It is worth mentioning the work performed by Mihaescu, Sakowitz, Semlitsch and others from the fluid mechanics group of KTH regarding compressor 3D-CFD modeling. Sakowitz et al. [67, 68] simulated and studied the mixing of two streams in T-junctions using Large Eddy Simulations (LES) and unsteady Reynolds averaged Navier-Stokes (URANS), focusing on the secondary structures generated due to the curvature in the region of the junction. Pulsating conditions and different mass flow ratios were imposed to simulate engine-like conditions. It was found a relation between the velocity ratio of the two streams and the mixing quality. Sakowitz et al. [69] performed a flow decomposition method to study the EGR mixing and distribution in a Diesel intake manifold using LES simulations. Pulsating oscillations were responsible of a large scale non-uniform cylinder-to-cylinder EGR distribution. Semlitsch et al. [70] studied the flow field in a compressor inlet generated by using a ported shroud configuration using a LES and finding good agreement with experimental data. The noise emission was assessed as well due to the strong impact of these kind of inlet configurations on the noise.

Focusing on compressor modeling, Baris et al. [56] studied the impact of a real inlet geometry on the compressor performance. Modeling the noise

generated in the compressor has been lately a main topic due to the generalization of the turbocharger usage [71, 72]. Authors such Evans et al. [10] and Teng et al. [73] studied a specific broad-band noise emitted when the compressor operates near stall conditions, this noise is more inconvenient because its frequency, around 1000-3000 Hz, lays in the range of human hearing peak sensitivity. At CMT-Motores Térmicos some research has also been made regarding the latter topic. Broatch et al. [74] analyzed the noise emission of a compressor at operating conditions close to surge and compared the experimental results with CFD predictions, using URANS and DES approaches. Broatch et al. [75] focused on the whoosh noise produced by a compressor and analyzed the flow behavior along the compressor channels and the diffuser. Torregrosa et al. [76] performed in-duct noise measurements and numerical validation of the results and also measured the radiated noise of a turbocharger using a technique based on acoustic particle velocity. The methodology for compressor simulation proposed by Navarro [77] is followed in this thesis in the corresponding sections (Sections 3.2 and 5.3). This methodology has proven to be capable of predicting flow field conditions at near-stall conditions and the generated noise.

1.3 Objectives

1.3.1 Main objectives

The coupling of the LR-EGR T-joint with the compressor involves several thermo-fluid dynamic processes that may be addressed individually for a proper understanding of the whole problem. Thus, the main objectives set to face the described phenomena are summarized as follows:

- Analyze the mechanics of in-flow water condensation due to the mixing of wet streams at different temperature and humidity, considering the LR-EGR as reference application for setting the operating conditions.
- Establish a consistent methodology that is able to predict the impact of the T-junction design on damage on the leading edges of the compressor wheel caused by the aforementioned mist flow.
- Study the role of the compressor on the mixing process itself and the

consequent condensation production, analyzing under which conditions this issue may be significant.

- Deepen in the influence of different basic geometries on the compressor performance (surge line, efficiency, etc). The highlighted selected configurations are: straight duct (baseline case), tapered duct, convergent-divergent nozzle and convergent nozzle.

1.3.2 Selected approaches

The objectives described in Section 1.3.1 involve both experimental tests and numerical simulations. The experimental methodologies are selected from previous researches that, in spite of not being widely popular, prove to be meaningful and consistent. Complete descriptions of the setups are shown in their corresponding chapters (see Sections 2.5.1 and 4.2). Concerning the numerical approach, LR-EGR T-joint and centrifugal compressor simulations are performed using the 3-dimensional commercial CFD code STAR-CCM+® of CD-Adapco. This code is based on a finite-volume approach, with 2^{nd} order discretizations in time and space. During the development of this thesis, versions 9.04.011 [78] and 11.06.010 [79] have been used, both with double precision to increase the acoustic prediction [80].

1.3.3 Methodological objectives

To accomplish the previous objectives, a set of milestones become essential, either because a non-existent tool is required to assess the main objectives and needs to be created, or for assuring the consistency of the conclusions that are to be made. Next, these methodological objectives are described:

- Development of a condensation tool for 3D-CFD applications that allows predicting the liquid water formed in an internal in-flow stream. It is required the model to be robust and consistent, agreeing with the physics as much as possible. The assumptions and simplifications considered ought to be properly exposed. The development of the model, as the bibliography establishes, must follow three leading steps:
  - Implementation of the model and verification. After the 3D-CFD software environment is clear, the model is theoretically shaped and

then implemented. The process of assuring the model behaves as it is intended to is collected in the verification step.

  - Validation of the model with experimental data. Once the verification is made, it is needed to check and adjust the model so it can simulate accurately the actual physics of the problem.

  - Finally, to ascertain the consistency and robustness of the model, a sensitivity study is required, both against geometrical variations and different numerical configurations of the CFD software.

- Minimization of the computational effort required exploring the possibility of decoupling the compressor from the simulation. The solution of a case with both the T-joint and the compressor is compared with the solution of the T-joint alone, assessing the error made through this assumption. The reduction in computational time is also presented as well as the uncertainties taken during this simplification.

- The experimental methodology, used either for validation of the models or for the fluid-dynamic analysis, needs to be well defined and established, relying on the bibliographic knowledge and on the wide in-house know-how for this purpose.

1.4 Thesis outline

Considering this introduction as Chapter 1, subsequent chapters are organized as follows.

The complete development of the condensation model is described in Chapter 2. First, the physical problem is exposed, taking into account the environmental conditions that surround the application that has been considered. Then, the condensation model approach is presented, as well as the commercial CFD code in which the model will be embedded. After it is implemented, the verification step is performed followed by the validation. Finally, the sensitivity analysis will be exposed.

The interaction between the radial compressor and the mixing and condensation mechanics is described in Chapter 3. There, the influence of the compressor under different conditions on the mixing process and thus, on the

condensation, is assessed. The computational effort required is faced as well, studying the possibility of its minimization.

Dealing with the other main topic of the thesis, the influence of the inlet geometry of the compressor is analyzed through an experimental study in Chapter 4. The selected geometries are introduced first, and the methodology is explained next, considering both steady and transient tests. The results obtained concerning compression ratio, efficiency and noise emission are discussed.

After, in Chapter 5 the most promising geometries of the previous experimental study are presented and analyzed through CFD simulations with analogous operating conditions, deepening in the flow structures. Several parameters involved in the flow state upstream the inducer are studied to find out if there is a correlation between them and surge closeness.

The concluding remarks of the thesis are summarized in Chapter 6. This includes the contributions made from different topics, the conclusions obtained during the discussions of the results of each part and recommendations for further studies on these matters.

Chapter 1 Bibliography

[9] F. Millo, F. Mallamo, E. Pautasso, and G. Ganio Mego. "The Potential of Electric Exhaust Gas Turbocharging for HD Diesel Engines." In: *SAE 2006 World Congress & Exhibition*. SAE International, 2006. DOI: 10.4271/2006-01-0437 (cit. on p. 3).

[10] D. Evans and A. Ward. "Minimizing Turbocharger Whoosh Noise for Diesel Powertrains." *SAE Technical Paper* 2005-01-2485 (2005). DOI: 10.4271/2005-01-2485 (cit. on pp. 3, 11, 96).

[11] Q. Yang, L. Li, Y. Zhao, J. Xiao, Y. Shu, and Q. Zhang. "Experimental investigation of an active control casing treatment of centrifugal compressors." *Experimental Thermal and Fluid Science* 83 (2017), pp. 107 – 117. ISSN: 0894-1777. DOI: 10.1016/j.expthermflusci.2016.12.013 (cit. on p. 3).

[12] M. Gancedo, E. Guillou, and E. Gutmark. "Effect of bleed slots on turbocharger centrifugal compressor stability." *International Journal*

of Heat and Fluid Flow 70 (2018), pp. 206 –215. ISSN: 0142-727X. DOI: 10.1016/j.ijheatfluidflow.2017.12.007 (cit. on p. 3).

[13] J. S. Gaffney and N. A. Marley. "The impacts of combustion emissions on air quality and climate - From coal to biofuels and beyond." *Atmospheric Environment* 43(1) (2009). Atmospheric Environment - Fifty Years of Endeavour, pp. 23 –36. ISSN: 1352-2310. DOI: 10.1016/j.atmosenv.2008.09.016 (cit. on p. 4).

[14] J. E. Kirwan, M. Shost, G. Roth, and J. Zizelman. "3-Cylinder Turbocharged Gasoline Direct Injection: A High Value Solution for Low CO2 and NOx Emissions." *SAE International Journal of Engines* 3(1) (2010), pp. 355–371. DOI: 10.4271/2010-01-0590 (cit. on p. 4).

[15] P. Michel, A. Charlet, G. Colin, Y. Chamaillard, G. Bloch, and C. Nouillant. "Optimizing fuel consumption and pollutant emissions of gasoline-HEV with catalytic converter." *Control Engineering Practice* 61 (2017), pp. 198 –205. ISSN: 0967-0661. DOI: 10.1016/j.conengprac.2015.12.010 (cit. on p. 4).

[16] J. R. Serrano, H. Climent, P. Piqueras, and E. Angiolini. "Filtration modelling in wall-flow particulate filters of low soot penetration thickness." *Energy* 112 (2016), pp. 883 –898. ISSN: 0360-5442. DOI: 10.1016/j.energy.2016.06.121 (cit. on p. 4).

[17] B. Guan, R. Zhan, H. Lin, and Z. Huang. "Review of state of the art technologies of selective catalytic reduction of NOx from diesel engine exhaust." *Applied Thermal Engineering* 66(1) (2014), pp. 395 –414. ISSN: 1359-4311. DOI: 10.1016/j.applthermaleng.2014.02.021 (cit. on p. 4).

[18] Petersen Publishing Company and E. Rosen. *The Petersen Automotive Troubleshooting & Repair Manual*. Grosset & Dunlap, 1975. ISBN: 9780448119465 (cit. on p. 4).

[19] A. Cairns, N. Fraser, and H. Blaxill. "Pre versus post compressor supply of cooled EGR for full load fuel economy in turbocharged gasoline engines." In: *SAE Technical Paper*. 2008. DOI: 10.4271/2008-01-0425 (cit. on pp. 4, 27).

[20] J. M. Luján, H. Climent, R. Novella, and M. E. Rivas-Perea. "Influence of a low pressure EGR loop on a gasoline turbocharged direct injection engine." *Applied Thermal Engineering* 89 (2015), pp. 432–443. DOI: 10.1016/j.applthermaleng.2015.06.039 (cit. on pp. 4, 27).

[21] J. M. Desantes, J. M. Luján, B. Pla, and J. A. Soler. "On the combination of high-pressure and low-pressure exhaust gas recirculation loops for improved fuel economy and reduced emissions in high-speed direct-injection engines." *International Journal of Engine Research* 14(1) (2013), pp. 3–11. DOI: 10.1177/1468087412437623 (cit. on p. 5).

[22] N. Ladommatos, S. Abdelhalim, and H. Zhao. "The effects of exhaust gas recirculation on diesel combustion and emissions." *International Journal of Engine Research* 1(1) (2000), pp. 107–126. DOI: 10.1243/1468087001545290 (cit. on p. 5).

[23] L. Cornolti, A. Onorati, T. Cerri, G. Montenegro, and F. Piscaglia. "1D simulation of a turbocharged Diesel engine with comparison of short and long EGR route solutions." *Applied Energy* 111 (2013), pp. 1–15. DOI: 10.1016/j.apenergy.2013.04.016 (cit. on p. 5).

[24] J. Luján, B Pla, S Moroz, and G Bourgoin. "Effect of low pressure EGR on gas exchange processes and turbocharging of a HSDI engine." In: *Proceedings of the conference on thermo-and fluid-dynamic processes in diesel engines (THIESEL 2008), Valencia, Spain, paper E.* Vol. 2. 2008 (cit. on p. 5).

[25] J. M. Luján, J. Galindo, J. R. Serrano, and B. Pla. "A methodology to identify the intake charge cylinder-to-cylinder distribution in turbocharged direct injection Diesel engines." *Measurement Science and Technology* 19(6) (2008), p. 065401. DOI: 10.1088/0957-0233/19/6/065401 (cit. on p. 5).

[26] A. Maiboom, X. Tauzia, and J.-F. Hétet. "Influence of EGR unequal distribution from cylinder to cylinder on NOx–PM trade-off of a HSDI automotive Diesel engine." *Applied Thermal Engineering* 29(10) (2009), pp. 2043 –2050. ISSN: 1359-4311. DOI: 10.1016/j.applthermaleng.2008.10.017 (cit. on p. 5).

[27] J. Benajes, J. R. Serrano, S. Molina, and R. Novella. "Potential of Atkinson cycle combined with EGR for pollutant control in a HD diesel engine." *Energy Conversion and Management* 50(1) (2009), pp. 174 – 183. ISSN: 0196-8904. DOI: 10.1016/j.enconman.2008.08.034 (cit. on p. 5).

[28] J. R. Serrano, X. Margot, A. Tiseira, and L. M. García-Cuevas. "Optimization of the inlet air line of an automotive turbocharger." *International Journal of Engine Research* 14(1) (2013), pp. 92–104. DOI: 10.1177/1468087412449085 (cit. on pp. 6, 9, 28, 96).

[29] Dirección General de Tráfico. Gobierno de España. *Vehicles in operation in Spain*. 2016. URL: https://sedeapl.dgt.gob.es (cit. on pp. 6, 7).

[30] S. J. Kim and H. C. No. "Turbulent film condensation of high pressure steam in a vertical tube." *International Journal of Heat and Mass Transfer* 43(21) (2000), pp. 4031–4042. DOI: 10.1016/S0017-9310(00)00015-6 (cit. on pp. 8, 28).

[31] P. Panday. "Two-dimensional turbulent film condensation of vapours flowing inside a vertical tube and between parallel plates: a numerical approach." *International journal of refrigeration* 26(4) (2003), pp. 492–503. DOI: 10.1016/S0140-7007(02)00162-7 (cit. on pp. 8, 28).

[32] J. Liu, H. Aizawa, and H. Yoshino. "CFD prediction of surface condensation on walls and its experimental validation." *Building and Environment* 39(8) (2004), pp. 905–911. DOI: 10.1016/j.buildenv.2004.01.015 (cit. on pp. 8, 28).

[33] L. Vyskocil, J. Schmid, and J. Macek. "CFD simulation of air–steam flow with condensation." *Nuclear Engineering and Design* 279 (2014), pp. 147–157. DOI: 10.1016/j.nucengdes.2014.02.014 (cit. on pp. 8, 28, 31, 70).

[34] D.-Y. Shang and L.-C. Zhong. "Extensive study on laminar free film condensation from vapor–gas mixture." *International Journal of Heat and Mass Transfer* 51(17) (2008), pp. 4300–4314. DOI: 10.1016/j.ijheatmasstransfer.2008.03.004 (cit. on pp. 8, 28).

[35] C. Moses and G. Stein. "On the growth of steam droplets formed in a Laval nozzle using both static pressure and light scattering measurements." *Journal of Fluids Engineering* 100(3) (1978), pp. 311–322. DOI: 10.1115/1.3448672 (cit. on pp. 8, 28, 70).

[36] M. Grubel, J. Starzmann, M. Schatz, T. Eberle, and D. Vogt. "Two-phase flow modeling and measurements in low-pressure turbines-Part 1: Numerical validation of wet steam models and turbine modeling." In: 2014. DOI: 10.1115/GT2014-25244 (cit. on pp. 8, 28).

[37] M. Abarham, T. Chafekar, J. Hoard, D. Styles, and D. Assanis. "A visualization test setup for investigation of water-deposit interaction in a surrogate rectangular cooler exposed to diesel exhaust flow." *SAE Technical Paper* 2012-01-0364 (2012). DOI: 10.4271/2012-01-0364 (cit. on pp. 8, 28).

[38] A. Warey, A. S. Bika, D. Long, S. Balestrino, and P. Szymkowicz. "Influence of water vapor condensation on exhaust gas recirculation cooler fouling." *International Journal of Heat and Mass Transfer* 65 (2013), pp. 807–816. DOI: 10.1016/j.ijheatmasstransfer.2013.06.063 (cit. on pp. 8, 28).

[39] G. Bourgoin, E. Tomas, J. Luján, and B. Pla. "Acidic Condensation in HP EGR Systems Cooled at Low Temperature Using Diesel and Biodiesel Fuels." *SAE Technical Paper* 2010-01-1530 (2010). DOI: 10.4271/2010-01-1530 (cit. on pp. 8, 28).

[40] S. Moroz, G. Bourgoin, J. M. Luján, and B. Pla. "Acidic condensation in low pressure EGR systems using diesel and biodiesel fuels." *SAE Int. J. Fuels Lubr* 2009-01-2805 (2009). DOI: 10.4271/2009-01-2805 (cit. on pp. 8, 28).

[41] J. R. Serrano, P. Piqueras, E. Angiolini, C. Meano, and J. De La Morena. "On Cooler and Mixing Condensation Phenomena in the Long-Route Exhaust Gas Recirculation Line." In: *SAE Technical Paper*. 2015. DOI: 10.4271/2015-24-2521 (cit. on pp. 8, 10, 28, 32, 41, 54, 150).

[42] A. Castorrini, A. Corsini, F. Rispoli, P. Venturini, K. Takizawa, and T. E. Tezduyar. "Computational analysis of wind-turbine blade rain erosion." *Computers & Fluids* 141(Supplement C) (2016), pp. 175 –183. ISSN: 0045-7930. DOI: 10.1016/j.compfluid.2016.08.013 (cit. on pp. 8, 28).

[43] P. Z. John, T. Koka, and S. Dayalan. "Water droplet erosion simulation of a turbocharger compressor wheel." In: *ASME Turbo Expo 2014: Turbine Technical Conference and Exposition*. GT2014-26974. American Society of Mechanical Engineers. 2014 (cit. on pp. 8, 28).

[44] A. Surendran and H. D. Kim. "Effects of Wet Compression on the Flow Behavior of a Centrifugal Compressor: A CFD Analysis." In: *ASME Turbo Expo 2014: Turbine Technical Conference and Exposition*. GT2014-25035. American Society of Mechanical Engineers. 2014, V02DT42A002. DOI: 10.1115/GT2014-25035 (cit. on pp. 8, 28).

[45] E. M. Greitzer. "Surge and rotating stall in axial flow compressors–Part I: Theoretical compression system model." *Journal of Engineering for Gas Turbines and Power* 98(2) (1976), pp. 190–198. DOI: 10.1115/1.3446138 (cit. on pp. 8, 95).

[46] M. C. Huppert. *Compressor surge*. Tech. rep. 1965 (cit. on pp. 8, 96).

[47] D. Fink, N. Cumpsty, and E. Greitzer. "Surge dynamics in a free-spool centrifugal compressor system." *Journal of Turbomachinery* 114(2) (1992), pp. 321–332. DOI: 10.1115/91-GT-031 (cit. on pp. 8, 96).

[48] F. Willems and B. De Jager. "Modeling and control of compressor flow instabilities." *Control Systems, IEEE* 19(5) (1999), pp. 8–18. DOI: 10.1109/37.793434 (cit. on pp. 8, 96).

[49] A. Epstein, J. Ffowcs Williams, and E. Greitzer. "Active suppression of aerodynamic instabilities in turbomachines." *Journal of Propulsion and Power* 5(2) (1989), pp. 204–211. DOI: 10.2514/3.23137 (cit. on pp. 8, 96).

[50] J. T. Gravdahl, O. Egeland, and S. O. Vatland. "Drive torque actuation in active surge control of centrifugal compressors." *Automatica* 38(11) (2002), pp. 1881–1893. DOI: 10.1016/S0005-1098(02)00113-9 (cit. on pp. 8, 96).

[51] E. Sundström, B. Semlitsch, and M. Mihăescu. "Generation Mechanisms of Rotating Stall and Surge in Centrifugal Compressors." *Flow, Turbulence and Combustion* 100(3) (2018), pp. 705–719. ISSN: 1573-1987. DOI: 10.1007/s10494-017-9877-z (cit. on pp. 9, 126, 136).

[52] A. Zamiri, B. J. Lee, and J. T. Chung. "Numerical evaluation of transient flow characteristics in a transonic centrifugal compressor with vaned diffuser." *Aerospace Science and Technology* 70 (2017), pp. 244 –256. ISSN: 1270-9638. DOI: 10.1016/j.ast.2017.08.003 (cit. on p. 9).

[53] I. Shahin, M. Alqaradawi, M. Gadala, and O. Badr. "Large eddy simulation of surge inception and active surge control in a high speed centrifugal compressor with a vaned diffuser." *Applied Mathematical Modelling* 40(23) (2016), pp. 10404 –10418. ISSN: 0307-904X. DOI: 10.1016/j.apm.2016.07.030 (cit. on p. 9).

[54] I. Ariga, N. Kasai, S. Masuda, Y. Watanabe, and I. Watanabe. "The effect of inlet distortion on the performance characteristics of a centrifugal compressor." *Journal of Engineering for Gas Turbines and Power* 105(2) (1983), pp. 223–230. DOI: 10.1115/82-GT-92 (cit. on pp. 9, 96).

[55] G. Capon and T. Morris. "The effect of air inlet system features on automotive turbocharger compressor performance." In: 9^{th} *International Conference on Turbochargers and Turbocharging*. 2010 (cit. on pp. 9, 96).

[56] O. Baris and F. Mendonça. "Automotive Turbocharger Compressor CFD and Extension Towards Incorporating Installation Effects." In: *Proceedings of ASME Turbo Expo 2011: Power for Land, Sea and Air*. ASME, 2011, pp. 2197–2206. DOI: 10.1115/GT2011-46796 (cit. on pp. 9, 10, 96).

[57] J. Galindo, J. R. Serrano, X. Margot, A. Tiseira, N. Schorn, and H. Kindl. "Potential of flow pre-whirl at the compressor inlet of automotive engine turbochargers to enlarge surge margin and overcome packaging limitations." *International journal of heat and fluid flow* 28(3) (2007), pp. 374–387. DOI: 10.1016/j.ijheatfluidflow.2006.06.002 (cit. on pp. 9, 96, 128).

[58] R. Lang. "Contribución a la Mejora del Margen de Bombeo en Compresores Centrífugos de Sobrealimentación." PhD thesis. Universitat Politècnica de València, 2011 (cit. on pp. 9, 96, 104, 120, 147).

[59] J. Galindo, F. Arnau, A. Tiseira, R. Lang, H. Lahjaily, and T. Gimenes. "Measurement and Modeling of Compressor Surge on Engine Test Bench for Different Intake Line Configurations." *SAE Technical Paper* 2011-01-0370 (2011). DOI: 10.4271/2011-01-0370 (cit. on pp. 9, 10, 99, 125).

[60] J. Desantes, J. M. Luján, B Pla, and J. Soler. "Potential of using a nozzle at the compressor inlet of a high-speed direct-injection diesel engine." *Proceedings of the Institution of Mechanical Engineers, Part D: Journal of Automobile Engineering* 225(2) (2011), pp. 178–189. DOI: 10.1243/09544070JAUTO1429 (cit. on pp. 9, 104, 121, 125, 135, 148).

[61] J. Galindo, A. Tiseira, F. J. Arnau, and R. Lang. "On-Engine Measurement of Turbocharger Surge Limit." *Experimental Techniques* 37(1) (2013), pp. 47–54. ISSN: 1747-1567. DOI: 10.1111/j.1747-1567.2010.00697.x (cit. on pp. 9, 10, 99, 150).

[62] J. Luján, V. Bermúdez, J. R. Serrano, and C. Cervelló. "Test bench for turbocharger groups characterization." *SAE Technical Paper* 2002-01-0163 (2002). DOI: 10.4271/2002-01-0163 (cit. on pp. 9, 44, 96).

[63] M. Tancrez, J. Galindo, C. Guardiola, P. Fajardo, and O. Varnier. "Turbine adapted maps for turbocharger engine matching." *Experimental Thermal and Fluid Science* 35(1) (2011), pp. 146–153. DOI: 10.1016/j.expthermflusci.2010.07.018 (cit. on pp. 9, 44).

[64] J. Galindo, H. Climent, C. Guardiola, and A. Tiseira. "On the effect of pulsating flow on surge margin of small centrifugal compressors for automotive engines." *Experimental Thermal and Fluid Science* 33(8) (2009), pp. 1163–1171. DOI: 10.1016/j.expthermflusci.2009.07.006 (cit. on pp. 10, 96, 99).

[65] A. Broatch, J. Galindo, R. Navarro, and J. García-Tíscar. "Methodology for experimental validation of a CFD model for predicting noise generation in centrifugal compressors." *International Journal of Heat and Fluid Flow* 50 (2014), pp. 134–144. DOI: 10.1016/j.ijheatfluidflow.2014.06.006 (cit. on pp. 10, 96, 120, 124).

[66] A. J. Torregrosa, A. Broatch, X. Margot, and J. García-Tíscar. "Experimental methodology for turbocompressor in-duct noise evaluation based on beamforming wave decomposition." *Journal of Sound and Vibration* 376 (2016), pp. 60–71. DOI: 10.1016/j.jsv.2016.04.035 (cit. on p. 10).

[67] A. Sakowitz, M. Mihaescu, and L. Fuchs. "Turbulent flow mechanisms in mixing T-junctions by Large Eddy Simulations." *International Journal of Heat and Fluid Flow* 45 (2014), pp. 135–146. DOI: 10.1016/j.ijheatfluidflow.2013.06.014 (cit. on pp. 10, 29, 47).

[68] A. Sakowitz, M. Mihaescu, and L. Fuchs. "Effects of velocity ratio and inflow pulsations on the flow in a T-junction by Large Eddy Simulation." *Computers & Fluids* 88 (2013), pp. 374–385. ISSN: 0045-7930. DOI: 10.1016/j.compfluid.2013.10.001 (cit. on p. 10).

[69] A. Sakowitz, M. Mihaescu, and L. Fuchs. "Flow decomposition methods applied to the flow in an IC engine manifold." *Applied Thermal Engineering* 65(1–2) (2014), pp. 57–65. ISSN: 1359-4311. DOI: 10.1016/j.applthermaleng.2013.12.082 (cit. on p. 10).

[70] B. Semlitsch, V JyothishKumar, M. Mihaescu, L. Fuchs, E. Gutmark, and M. Gancedo. "Numerical Flow Analysis of a Centrifugal Compressor with Ported and without Ported Shroud." *SAE Technical Paper* 2014-01-1655 (2014). DOI: 10.4271/2014-01-1655 (cit. on p. 10).

[71] A. Karim, K. Miazgowicz, B. Lizotte, and A. Zouani. "Computational Aero-Acoustics Simulation of Compressor Whoosh Noise in Automotive Turbochargers." *SAE Technical Paper* 2013-01-1880 (2013). DOI: 10.4271/2013-01-1880 (cit. on pp. 11, 96).

[72] T. Raitor and W. Neise. "Sound generation in centrifugal compressors." *Journal of Sound and Vibration* 314 (2008), pp. 738–756. ISSN: 0022-460X. DOI: 10.1016/j.jsv.2008.01.034 (cit. on pp. 11, 97).

[73] C. Teng and S. Homco. "Investigation of Compressor Whoosh Noise in Automotive Turbochargers." *SAE Int. J. of Passeng. Cars-Mech. Syst.* 2(1) (2009), pp. 1345–1351. DOI: 10.4271/2009-01-2053 (cit. on pp. 11, 96).

[74] A. Broatch, J. Galindo, R. Navarro, and J. García-Tíscar. "Numerical and experimental analysis of automotive turbocharger compressor aeroacoustics at different operating conditions." *International Journal of Heat and Fluid Flow* 61 (2016), pp. 245 –255. ISSN: 0142-727X. DOI: 10.1016/j.ijheatfluidflow.2016.04.003 (cit. on pp. 11, 28, 70, 86, 122, 136).

[75] A. Broatch, J. Galindo, R. Navarro, J. García-Tíscar, A. Daglish, and R. K. Sharma. "Simulations and measurements of automotive turbocharger compressor whoosh noise." *Engineering Applications of Computational Fluid Mechanics* 9(1) (2015). DOI: 10.1080/19942060.2015.1004788 (cit. on pp. 11, 96, 122).

[76] A. J. Torregrosa, A. Broatch, R. Navarro, and J. García-Tíscar. "Acoustic characterization of automotive turbocompressors." *International Journal of Engine Research* 16(1) (2015), pp. 31–37. DOI: 10.1177/1468087414562866 (cit. on pp. 11, 98, 137).

[77] R. Navarro. *Predicting Flow-Induced Acoustics at Near-Stall Conditions in an Automotive Turbocharger Compressor: A Numerical Approach*. Springer, 2018. ISBN: 978-3-319-72248-1. DOI: 10.1007/978-3-319-72248-1 (cit. on pp. 11, 71, 73, 122, 123).

[78] *STAR-CCM+*. Release version 9.04.011. CD-adapco. 2014. URL: http://www.cd-adapco.com (cit. on pp. 12, 29, 30, 35, 36, 47, 60).

[79] *STAR-CCM+*. Release version 11.06.010. CD-adapco. 2016. URL: http://www.cd-adapco.com (cit. on pp. 12, 70, 72, 120, 122).

[80] M. Perić. "Acoustics and Turbulence: Aerodynamics Applications of STAR-CCM+." In: *South East Asian Conference*. 2012 (cit. on p. 12).

Chapter 2

Condensation model for Long-Route EGR CFD simulation

Contents

2.1 Introduction

Due to the constant increase of emission regulations restrictions and the competitiveness in automotive engines, techniques that seek better efficiency combined with low emissions are being developed constantly. This non trivial combination of goals also requires improving or keeping the mechanical power.

Emissions reduction technologies used nowadays are either in-cylinder control or aftertreatment (A/T) control [81, 82]. In-cylinder control systems reduce the generation of emissions within the source, during the combustion process. For instance, controlling the injection scheme [83], the maximum in-cylinder pressure, with thermal management [84] or using recirculating exhaust gases (EGR). On the other side, A/T systems reduce pollutant emissions along the exhaust line [85], such as diesel particulate filters (DPFs), selective catalytic reduction (SCR) or diesel oxidation catalysts (DOC) [86]. This work is focused on one of these systems, specifically on the exhaust gas recirculation (EGR). This consists in reintroducing part of the exhaust gases resulting from the combustion process back again in the cylinders mixed with fresh air, which causes a decrease in the maximum temperature achieved during the combustion process so that the nitrogen oxides (NO_x) formation is reduced while the mean pressure in the cylinders is kept almost the same. EGR most common application is CI engines, nevertheless it is beneficial in turbocharged SI engines too [19, 20].

As turbochargers are indispensable in diesel engines, two possible paths of recirculation are available. First, the usage of the Short Route-EGR was spread, this configuration connects the exhaust manifold to the intake manifold, cooling the exhaust gases in an intercooler. Afterwards, the Long Route-EGR gained popularity. The LR-EGR takes the exhaust gases downstream of the after-treatment, benefiting from the use of clean gases, and reintroduces them upstream of the compressor. There are significant advantages of using the latter configuration (see Section 1.1) but also an important drawback appears.

Due to the high water content of the EGR flow, condensation may arise provided that the necessary conditions are met. This may be a problem for the LR-EGR, since water droplets may damage the compressor wheel. For the SR-EGR, since the exhaust gases are reintroduced downstream the compressor, condensation is less critical. In fact, it may even be a feasible technique for

on-board regeneration of the cooler efficiency [37, 38]. Condensation when using LR-EGR may be produced in the EGR cooler as well. Despite the lower acidity due to suspended contaminants than in SR-EGR [39, 40], condensation may still cause damage to the compressor wheel. LR-EGR condensation may also be produced within the flow when EGR stream is mixed with cold ambient fresh air. A combination of both ambient and engine/EGR operating point conditions may lead the mixing process to reach saturated conditions and the water to condensate. For example, ambient temperatures below +10 °C are susceptible to condensate EGR within the bulk of the mixing region for moderate EGR rates.

If condensation occurs, water droplets are driven towards the compressor wheel which is normally rotating at very high speed, implying elevated relative momentum and impact damage [42]. Dramatic consequences are observed at the leading edges of the compressor wheel if droplets impact the blades for long enough, as noticed by Serrano et al. [41]. Surface coating is normally applied to the wheel, partially protecting against this erosion, nevertheless it is not infallible, as observed by Koka et al. [43]. Once the water penetrates the compressor inducer, due to its inertia, it may not follow the air streamlines but get attached to the wheel walls, forming rivers and leaving depositions [41]. The load of the compressor wheel may also change, according to Surendran et al. [44].

The complexity of the condensation within the flow has to be remarked. Wall condensation in the interior of tubes has been deeply studied by many authors [30, 31], and wall condensation in free streams by others [32, 34, 33]. However, bulk flow condensation has not been researched extensively because there are less applications in which this process is important and in addition, a combination of both 3D fluid dynamic and psychrometric models are needed, since the complex turbulent flow structures upstream the compressor [28] and the mixing process control condensation rate [74]. Condensation will be produced at constant pressure and as a consequence of the mixing of two different flows at different psychrometric conditions.

It is worth noting that a different cause that also produces condensation in the bulk flow has been studied by Moses et al. [35] and later Grübel et al. [36], where the water droplets appear due to the decrease of temperature caused by the acceleration of the flow in a de Laval nozzle. Due to the high velocities found in these sort of nozzles, small errors predicting the appearance of condensation imply greater errors in its location, therefore complex models

that accurately predict the nucleation and growth of water droplets within the fluid are required. Since the characteristic velocities found in a LR-EGR system are relatively low, this type of condensation will not be considered in the present work.

Due to the importance of local effects on the mixing process of the intake and EGR flows and on the resulting condensation, it is interesting to address the problem using 3D-CFD simulations. For instance, Patel et al. [87] assessed the impact of several turbulence models on the condensation formation in low-pressure turbines and modified a k-ω SST model to improve the prediction accuracy. Sakowitz et al. [67] studied the mixing process in two T-junctions using LES and comparing the results with both experimental data and URANS simulations, detecting secondary structures that control the mixing and concluding that the velocity ratio between both inlet streams impacts the mixing quality.

The model that is presented below is conceived to be embedded in the CFD commercial code STAR-CCM+® [78], which allows the creation of user field functions, enabling the implementation of a custom condensation model. According to Versteeg and Malalsekera [88], to quantify the level of confidence of the results obtained with a new developed model, it is needed to follow a set of steps that would assess the unavoidable errors and uncertainties committed. The concepts of verification and validation, introduced by AIAA [89] and Oberkampf and Trucano [90], are now widely accepted and are defined as follows:

- **Verification:** this process consist in assessing if the equations proposed are being solved as intended by the developer, i.e., a quantification of the error [91, 92]. Numerical divergence introduced by the code and programming mistakes are commonly main topics of this step.
- **Validation:** this process consist in evaluating the accuracy of the model in predicting the actual physics of the addressed problem, quantifying the uncertainty. Experimental data is usually used for comparing the results, adjusting tunable parameters and coefficients if necessary. A critical analysis should be made by the developer, clearly defining the validity range of the model.

This chapter is organized as follows. First, a summary of the background,

introducing the available models and the psychrometric physics that govern the problem is presented in Section 2.2. Section 2.3, covers a description of the proposed approach for the condensation model. After, in Section 2.4 it is proceeded with the verification of the model, using a simple geometry and a validated 0D perfect mixing condensation model for that purpose. Then, in Section 2.5, the validation and the sensitivity analysis are performed. Finally, some concluding remarks will be provided in section 2.6.

2.2 Background and model validation strategy

With respect to 3D-CFD calculation model, a first exploration of diverse possibilities available in the STAR-CCM+® [78] code leads this study to the so-called *Defogging model*, which claims to simulate defogging (evaporation) inside a cabin windshield or surface [93]. In spite of condensation not being the main scope application of this model, there is an important aspect of the *Defogging model* that could be used. A property which may be enabled consists in a super saturation limitation that controls the specific humidity not to exceed saturation conditions by condensing vapor into water. However, numerical experiments show that condensation is produced isothermally in *Defogging model* as shown in Fig. 2.1. This is not suitable as condensation should be an isenthalpic process [94, 95]. The isothermal process is the result of removing the vapor content of the gas without releasing the latent heat of the condensation, what implies a greater amount of condensates at the end of the process. Hence, this model cannot be used for this work since the super saturation limitation is intended only to bound the problem but not to be used as an independent application itself.

Having discarded the *Defogging model*, other approaches the software offers are considered, from a complete phase Eulerian-Eulerian solver to a Lagrangian approach. However, due to the complexity of the problem and the diverse interactions between phases and components (phase change, liquid-gas interaction, liquid-surface interaction, coalescence, etc), the implementation and computational effort required exponentially grow, surpassing the scope this work. Moreover, a first quick exploration of these possibilities shows some incapacities for specifically modeling inflow condensation. Therefore, another solution is proposed. Considering that condensation acts as a sink of vapor mass and a source of energy on the flow conditions, the phase change mod-

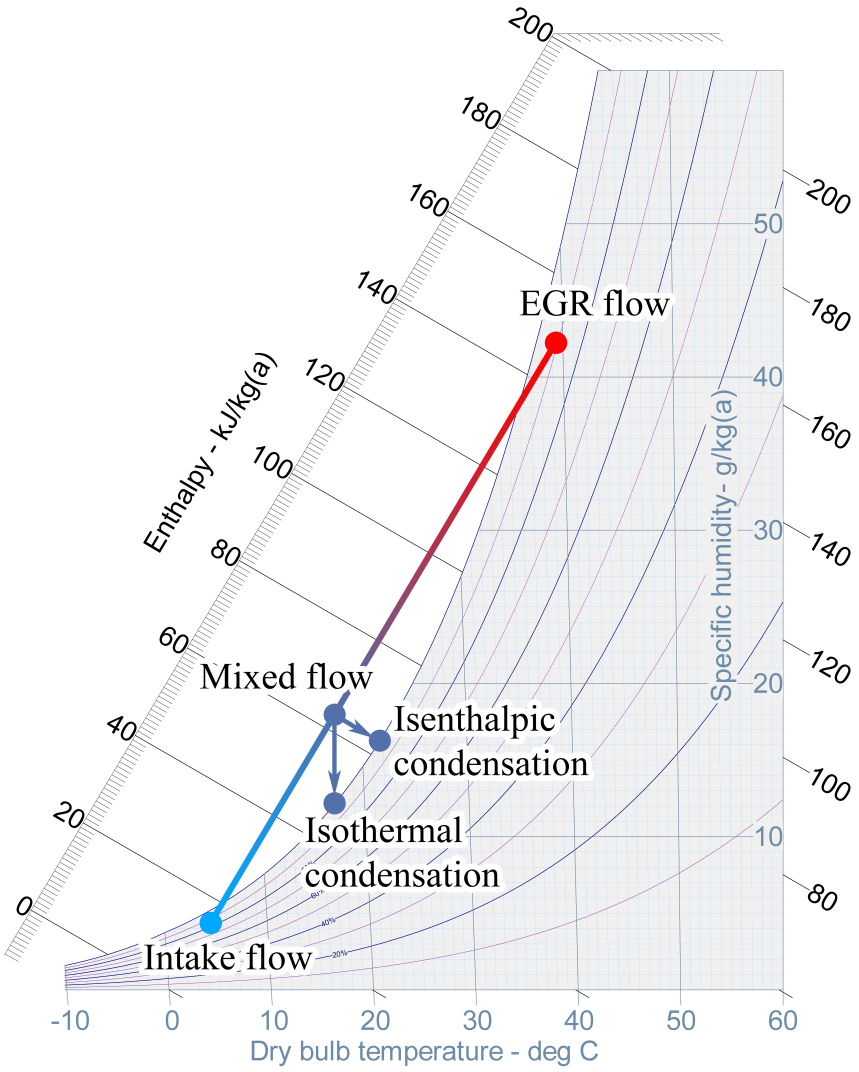

Figure 2.1: Psychrometric diagram with Isothermal and isenthalpic condensation processes produced when the hot wet flow of the EGR is mixed with the cold dry gas of the intake.

eled using user field functions and the transport equations are modified using available custom source terms, as will be explained in section 2.3. Vyskocil et al. [33] used a similar approach for calculating volume condensation.

There are different approaches to verify CFD simulation results. The physical problem which is faced here consists in the condensation due to the mixing of two gases at different temperatures and specific humidities but at a constant pressure. Mixing process is isenthalpic if both components are considered [94, 95]. If the conditions of the mixed gas results to be supersaturated, water may condensate isenthalpically until it reaches 100% of relative humidity. An example of how this process is produced is shown in the diagram of Fig. 2.1. A weighting of mass flow rates is used to calculate the enthalpy (Eq. 2.1) and the specific humidity (Eq. 2.2) of the mixed flow. Then, using Eq. (2.4), the temperature of the mixed flow is obtained.

The analytical solutions used to compare and verify the proposed model in this work correspond to an energy and mass balance system of equations developed by Serrano et al. [41]. As can be found in the referred work, the conservation equations are solved analytically with an iterative resolution method, to get the final state of a perfect mixing of two gases at different conditions, assuming an isenthalpic evolution. As any 0D balance, the computational effort to get the analytical solution is low but local effects are not considered. Therefore, for the CFD verification exposed in Section 2.4, a simple geometry is designed so the condensation model is the only responsible of the process, excluding local effects caused by the mixing process. For this purpose, a premixed option is chosen, thus with a simple straight duct the restrictions are solved.

The inlet conditions of this single inlet duct are calculated in 3D-CFD codes coupling both flows. Mass flow and mass fractions (the specific humidity) are directly obtained. Nevertheless, for the temperature, a similar process used for calculating the initial mixing point in the diagram method shown in Fig. 2.1 is used. The enthalpy of the initial mixing is calculated with the mass flow and the enthalpy of each inlet (Eq.2.1). The temperature is obtained knowing the enthalpy and the specific humidity of the mix [96] (Eq. 2.4).

$$h_{mix} = \frac{h_{in}\dfrac{\dot{m}_{in}}{\frac{w_{in}}{1000}+1} + h_{EGR}\dfrac{\dot{m}_{EGR}}{\frac{w_{EGR}}{1000}+1}}{\dfrac{\dot{m}_{in}}{\frac{w_{in}}{1000}+1} + \dfrac{\dot{m}_{EGR}}{\frac{w_{EGR}}{1000}+1}} \tag{2.1}$$

$$w_{mix} = \frac{w_{in}\frac{\dot{m}_{in}}{\frac{w_{in}}{1000}+1} + w_{EGR}\frac{\dot{m}_{EGR}}{\frac{w_{EGR}}{1000}+1}}{\frac{\dot{m}_{in}}{\frac{w_{in}}{1000}+1} + \frac{\dot{m}_{EGR}}{\frac{w_{EGR}}{1000}+1}} \tag{2.2}$$

$$h = (T - 273.15)\ c_{p_{air}} + h_{vap,sat}\ \frac{w}{1000} \tag{2.3}$$

$$h = (T - 273.15)\ c_{p_{air}} + (1.76\ (T - 273.15) + 2502.9)\ \frac{w}{1000} \tag{2.4}$$

Finally, the outcomes of the different methods (0D & 3D) are the temperature and the condensation rate of water in function of the dry air mass flow rate, verifying the flow is at saturated conditions.

2.3 Description of proposed condensation model in STAR-CCM+®

Once the objectives and limitations of the model are known, the hypothesis and simplifications that have been established for this work can be introduced.

- Instantaneous condensation: Relatively low velocities (M<0.2) control the mixing phenomena in a LR-EGR T-joint, causing the condensation to be practically instantaneous in time and space. The limit will be imposed by the time step and the size of the cell respectively.
- Liquid water phase is not modeled: The modeling of the water phase exceeds the objectives of this work, which is intended to create a condensation model that predicts the quantity of water generated due to the mixing of two flows at different conditions. In order to obtain this amount, the impact of the condensation calculation in the numerical model should be as low as possible, while the incorporation of an extra phase component in the simulation (with the relative Lagrangian approach) would lead the calculation effort to increase substantially. Nevertheless, as will be explained below, a passive scalar is used to track the

condensed water since it does not have much impact in the computational effort required. This simplification implies some small unbalances in the conservation equations, detailed as follows:

  - Continuity: Condensed water is taken into account by the passive scalar. However, the mass conservation in the calculated species is not met. The influence of this simplification should be low since condensed water represents less than 0.5% of the mass flow and hence, it can be neglected.
  - Momentum: Following a similar argumentation, the momentum of the liquid water that disappears represents again less than 0.5% of the total momentum, which has insignificant impact in the solution of the simulation.
  - Energy: This term is related to the enthalpy of the vapor that is disappearing, which in this case is below 1% due to the specific heat capacity of the vapor being twice the specific heat of the dry air. Nevertheless, the energy source term introduced in Eq. 2.11 takes into account this issue, producing at the end an isenthalpic process.

- Evaporation is not modeled: Potentially, some of the condensed water might be eventually evaporated if water droplets are in contact with subsaturated flow. However, once the condensation has occurred the flow remains very close to saturation conditions, which means that the evaporation rate would be minimal, if not zero [97, 98]. Modeling evaporation is challenging since it is not an instantaneous process, its characteristic time depending on the droplet size and other parameters that are not considered to avoid a Lagrangian approach and its subsequent increase of computational effort. In any case, this simplification produces a worst-case scenario concerning the condensation rate, keeping the prediction on the safety side.

- Isenthalpic condensation (Fig. 2.1): During a condensation process, since it is an adiabatic evolution, the enthalpy of the gas is kept constant [94, 95].

- Adiabatic walls: The objective is to predict bulk flow condensation, not condensation on the walls. Enabling heat transfer through the walls would cause water condensation on the walls, requiring a thin film condensation model. Moreover, the verification of the model would not be

possible with an energy balance since, in that case, the energy would not be conserved.

The actual condensation phenomenon is not going to be calculated due to the high complexity and computational cost. Instead, its effect on the mass and energy transport equations is going to be modeled taking into account the hypothesis and simplifications exposed above. Transport equations in discrete form for segregated flow simulations can be obtained considering the appropriate terms of Table 2.1 in the Eq. 2.5. STAR-CCM+® [78] allows arbitrary editing the source terms of the transport equations and this is going to be used to model the effect of the condensation. The relationship between the source terms of each equation will define the type of thermodynamic process that the condensation will follow.

$$\frac{\partial(\rho\ \varphi)}{\partial t} + \nabla(\rho\ \varphi\ u_i) = \nabla(\rho\ \Gamma_\varphi\ \nabla(\varphi)) + S_\varphi \tag{2.5}$$

Equation	$\boldsymbol{\varphi}$	$\boldsymbol{\Gamma_\varphi}$	$\boldsymbol{S_\varphi}$
Mass	1	–	S_{vap}
Species	Y	D	S_{vap}
Momentum	u_i	ν	$-\partial p/\partial x_i + f_m + f_v + S_{mom.}$
Energy	h	α	$-Dp/Dt + f_t + f_v + S_{ener.}$

Table 2.1: Transport equations.

The first parameter of the condensation that is considered is the relative humidity (RH), which is introduced in order to identify in which cells the condensation should appear, and is defined as the ratio between the partial pressure of the vapor and the saturation pressure of the dry air (Eq. 2.6). The partial pressure of the vapor is calculated by using the Dalton's law (Eq. 2.7) and the saturation pressure is obtained adjusting the Antoine equation coefficients with the data tables from Stull [99] valid for a temperature range between 255.9 and 373 K (Eq. 2.8) and thus suitable for the application of the current work. The enthalpy of the humid flow is defined in Eq. (2.4).

$$\mathrm{RH} = 100\ \frac{p_{\mathrm{vap}}}{p_{\mathrm{sat}}} \tag{2.6}$$

$$p_{\text{vap}} = \frac{p}{1 + 1000 \frac{\text{MW}_{H_2O}}{w \cdot \text{MW}_{\text{air}}}} \tag{2.7}$$

$$p_{\text{sat}} = 10^{4.6543 - \frac{1435.26}{T - 64.848}} \tag{2.8}$$

Relative humidities greater than 100% will trigger condensation occurrence. In Fig. 2.2 it is depicted a psychrometric diagram in function of the specific humidity, the dry bulb temperature, the relative humidity and the enthalpy. The starting point of the process (1) is placed in the saturated zone, with a relative humidity higher than 100%. If the process of condensation is produced isothermally as in *Defogging model* of STAR-CCM+® [78], the final point will be at the intersection of a vertical line from the starting point and the 100% of relative humidity curve (3). On the other side, if the process is produced isenthalpicly, the final desired point will be at the intersection of an isoenthalpic line with the 100% relative humidity curve. The value of temperature and specific humidity of this latter point are unknown. Equation 2.6 indicates that for saturated conditions, vapor and saturation pressure are equivalent (Eq. 2.6). With Eqs. 2.7 and 2.8 and in addition with the enthalpy Eq. 2.4, it is formed a system with two equations and two variables.

As the equation system is implicit, the solution cannot be calculated directly. Therefore, a numerical approach has to be established taking into account the limitations of the CFD software and the computational cost. There are two main aspects that must be carefully taken into account. In first place, the enthalpy ought to remain constant. For achieving this, heat may be released as the vapor condensates into water. If this restriction is locally accomplished, the enthalpy will be kept constant globally. In second place, the condensation is imposed to occur instantaneously, which in terms of CFD implies a complete condensation from the initial oversaturated state of a cell to saturated conditions in a single iteration. The size of the cell is then responsible for the local dimensions where the condensation takes place. That means a smaller condensation region for finer meshes. For the sake of accuracy, the size of the cells should be much smaller in comparison with the geometry, so that the influence of this parameter in the global condensation region is negligible.

The numerical model is set up to be iterative, being the number of iterations discussed later on. Figure 2.2 will be used to describe the calculation

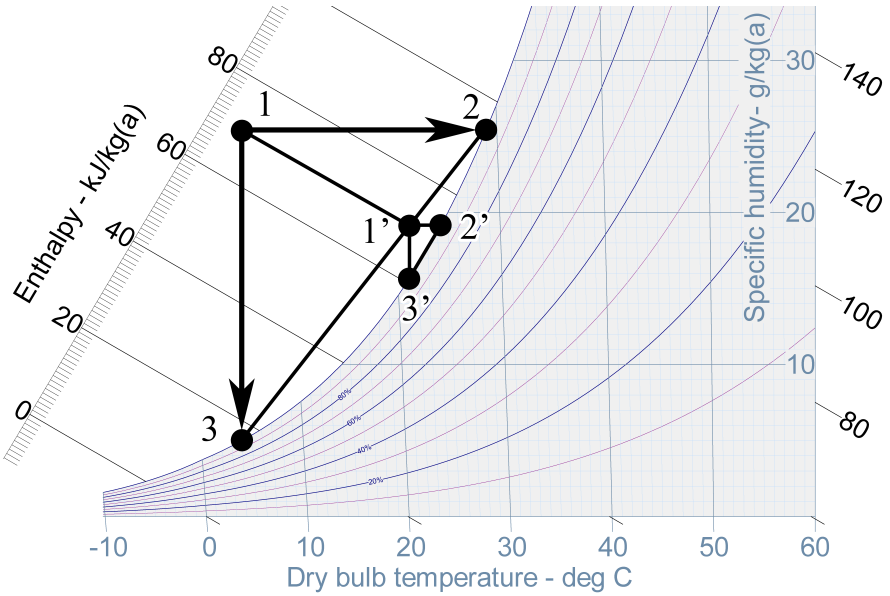

Figure 2.2: Iterative process of the numerical condensation model in a psychrometric diagram.

process. From the oversaturated starting point (1) the temperature and the specific humidity are known and thus its enthalpy can be calculated. Points (2) and (3) are obtained moving point (1) at iso-specific humidity and isothermally respectively. The temperature of point (2) and the specific humidity of point (3) can be obtained imposing saturated conditions at Eqs. 2.7 and 2.8. Next, enthalpies of points (2) and (3) are calculated and the specific humidity of point (1') is obtained by interpolating the enthalpies, according to Eq. 2.9.

$$w_{1'} = \frac{w_2 - w_3}{h_2 - h_3}(h_1 - h_3) + w_3 \tag{2.9}$$

Finally, the temperature of point (1') is calculated with the enthalpy Eq. (2.4). Taking point (1') as the new starting point, the process can be repeated as many times as desired to increase accuracy. When the last iteration is performed, the specific humidity of the last interpolated point (w_f) is used to

calculate the vapor mass source term shown in Eq. 2.10.

$$S_{\text{vap}} = \frac{\rho Y_{\text{air}} \left(w_f - w_1\right)}{\Delta \text{t}} \tag{2.10}$$

The dimensions of the mass source term required by the 3D-CFD code are $ML^{-3}T^{-1}$. Theoretically, the correct form of calculating this term would be the product of specific humidity times the mass flow rate through the cell and divided by the volume of the cell. This is not possible to be done because calculating the mass flow rate of the cell is not straight forward. One possibility could be taking into account each face of a given cell and calculating the net incoming flow. The sum of the flows of all faces of that given cell would be the mass flow, however, it is not possible with the current version of STAR-CCM+®. Instead, density and a characteristic velocity of a cell are used, obtaining a valid approximation of the source term. The denominator term of Eq. 2.10 is associated to the characteristic time in which the vapor mass source is being added to the flow or, in other words, the residence time of a particle in a given cell. This parameter can be calculated dividing the equivalent diameter of the cell (supposing it is a sphere) by the velocity of the flow in that cell. The energy source term is calculated simply considering the product of the species term and the latent heat of condensation of water (Eq. 2.11) and subtracting the sensible heat of the condensed vapor.

$$S_{\text{ener.}} = -S_{\text{vap}} \ \ \left(L - c_{p_{vap}} T\right) \tag{2.11}$$

Finally, for the momentum conservation, the corresponding value for the condensed vapor has been removed. In Eq. 2.12 this term is written. The momentum is the product of the mass times the velocity vector. The mass term is the source term of mass calculated in Eq. 2.10.

$$S_{\text{mom.}} = S_{\text{vap}} \ \ \vec{u} \tag{2.12}$$

Strictly, the mass conservation of the fluid volume is not being maintained since vapor mass is disappearing and a water liquid phase is not being taken into account. The justification of this simplification resides in the ratio between the condensed mass and the total inlet mass, which is below 0.5% (see

Table 2.4) and thus introduces little error to the conservation equations. Nevertheless, in order to trace the condensates, a passive scalar transport equation is introduced which considers the condensed water. The functioning simply consists in a scalar value that is transported by the flow and increases as the condensation takes place, with diffusion and convection driven by a Schmidt number of 0.9 [100]. The Schmidt number defines the ratio between the viscous and molecular diffusivity, as defined in Eq. 2.13

$$\mathrm{Sc} = \frac{\nu}{D} = \frac{\mu}{\rho\, D} = \frac{\text{viscous diffusion rate}}{\text{molecular (mass) diffusion rate}} \tag{2.13}$$

The condensation rate of the simulation is calculated computing the flow rate of passive scalar across the outlet surface.

To conclude this section, a study of the influence of the number of iterations of the numerical model (Fig. 2.2) is performed to quantify the impact of this parameter in accuracy of the results and the computational cost. Simulations of the 15% of EGR rate case from Table 2.3 were performed with one, two and three iteration cycles. Results of condensation rates showed negligible differences (<1%) among all the simulations. The explanation resides in the exaggeration of the starting over-saturated point in the psychrometric diagram shown in Fig. 2.2. In fact, due to the resolution of the mesh and the solvers, the iteration is produced naturally in consecutive cells as the flow passes through. However, the impact on the computational cost is indeed very high. Respect to a reference case without condensation with a normalized iteration time of 100%, for 1, 2 and 3 iterations of the numerical model, the computational time increased to 120, 135 and 250% respectively, as can be seen in Table 2.2. For the verification of the model, a single sub-iteration is set and will be justified in Section 2.4.2.

Sub-iterations (-)	0	1	2	3
Computational time (%)	100	120	135	250

Table 2.2: Normalized computational time for different sub-iterations.

2.4 Verification of the model

As aforementioned in section 2.1, when a new model is developed and implemented, a verification process must be done in order to check that the equations are behaving as intended [88, 91, 92]. This process is addressed to detect implementation errors and to quantify the errors due to discretization, round-off and iterative convergence.

2.4.1 Numerical setup

In this section, the configuration of the simulation case is discussed, from choosing the solver to defining the boundary conditions.

Concerning the solver, a segregated model with multi component ideal gas is used and the widely-used RANS k-ϵ turbulence model [101] is imposed to close the flow equations. A time step of $1{\cdot}10^{-4}$ s is used to capture oscillations with characteristic lengths below the duct diameter. Gravitational effects are neglected since the Froude number, calculated from gravity and characteristics velocity and length, is around 25, much greater than 1, implying greater influence of inertial forces compared with gravitational ones. Conventional boundary conditions are used i.e., mass flow and temperature are imposed for the inlet and a constant static pressure is set for the outlet.

Regarding the CFD configuration of the mesh, polyhedral cells have been used, with an average cell length of 1.8 mm, resulting in about 400k cells. In addition, eight prism layers are imposed at the walls to increase boundary layer resolution. An independence mesh study has been performed with two additional meshes, presenting respectively one fourth and four times the number of cells compared with the reference one. Discrepancies below 1% in global variables including condensation rate were found in the finer mesh, whereas for the coarser one discrepancies were above 5%. Therefore the reference mesh with 400k cells was selected.

Operating parameters of the simulations are not arbitrary but are within the range of a LR-EGR engine working in very cold climates since such low ambient temperatures suppose a worst case scenario in terms of condensation.

Table 2.3 summarizes the parameters that were used to define the boundary conditions of the different simulations. Five working points are defined,

covering a wide range of EGR rate thus allowing a comprehensive verification of the model.

Ambient temperature (°C)	-15
Ambient RH (%)	100
Ambient specific humidity (g/kg dry air)	1.62
LR-EGR rate (%)	5,10,15,20,25
LR-EGR cooler outlet temperature (°C)	55
LR-EGR specific humidity (g/kg dry air)	50

Table 2.3: Operating conditions.

2.4.2 Results and discussion

Table 2.4 shows the results of outlet temperature and condensation rate provided by the 3D-CFD simulations with the developed condensation model at the operating conditions defined by Table 2.3. Table 2.4 includes the 3D-CFD prediction in terms of absolute values and relative differences when compared to the 0D balance.

Comparisons are performed using the perfect mixing 0D balance equations developed by Serrano et al. [41] as the reference. Regarding 3D simulation, errors below 1% are found for water condensation and temperature for all the range of EGR rate. High accuracy is reasonable, since the same equations are used for both 3D-CFD and 0D balance. Minor discrepancies are due to numerical error and local effects. Since condensation is triggered by over-saturated conditions, the 3D simulations will always end the process by the side of non-saturated conditions. Normally, final relative humidities are around 99.75%, what would imply slightly more condensation and increased temperature if the process is being perfectly isenthalpic.

In Fig. 2.3 it is depicted the condensation rate evolution along the axis cross-sections for the 15% EGR rate case of Table 2.3. Due to the premixed state of the inlet flow the condensation process takes place within the very first part of the duct. Afterwards, equilibrium conditions are reached and kept constant until the outlet of the duct. Comparing this evolution with the solution of the 0D perfect mixing balance, for the same inlet conditions, it can be seen the perfect agreement of the 3D simulation.

Model	T_{out} (K)	$\frac{\dot{m}_{H_2O}}{\dot{m}_{air}}$ (-)	ΔT (K)	ϵ $\frac{\dot{m}_{H_2O}}{\dot{m}_{air}}(\%)$
5% EGR rate				
0D balance	265.20	$1.46{\cdot}10^{-3}$		
3D-CFD	265.27	$1.46{\cdot}10^{-3}$	0.07	-0.46
10% EGR rate				
0D balance	271.38	$2.58{\cdot}10^{-3}$		
3D-CFD	271.46	$2.56{\cdot}10^{-3}$	0.08	-0.45
15% EGR rate				
0D balance	276.72	$3.35{\cdot}10^{-3}$		
3D-CFD	276.78	$3.34{\cdot}10^{-3}$	0.05	-0.20
20% EGR rate				
0D balance	281.34	$3.82{\cdot}10^{-3}$		
3D-CFD	281.36	$3.83{\cdot}10^{-3}$	0.02	0.19
25% EGR rate				
0D balance	285.34	$4.05{\cdot}10^{-3}$		
3D-CFD	285.34	$4.07{\cdot}10^{-3}$	-0.01	0.69

Table 2.4: Result summary and comparison.

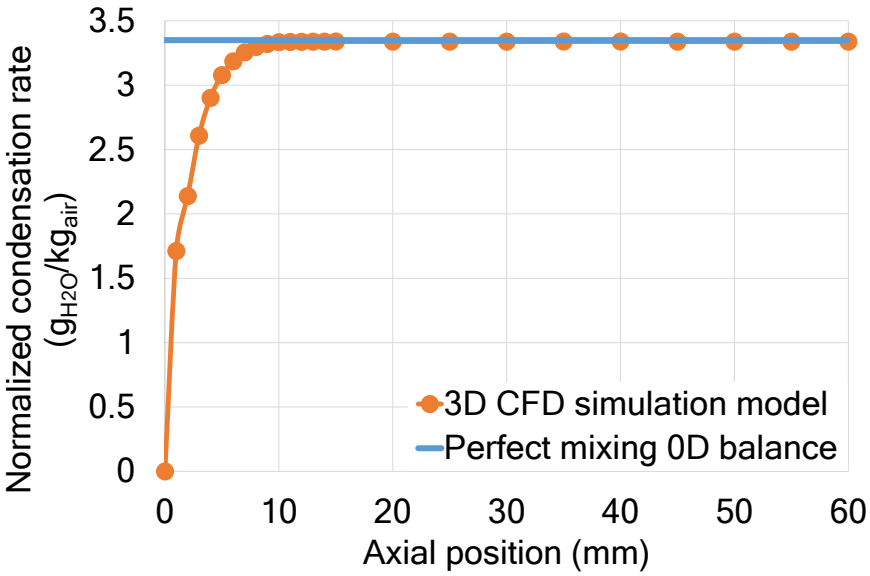

Figure 2.3: Condensation rate evolution during the duct inlet.

Fig. 2.4 corresponds to a detailed section of the specific humidity scalar field in the inlet duct. The mesh has been superimposed allowing to notice the specific number of cells the condensation process needs to reach saturated conditions.

Taking into account the base size of the cells and a mean number of 4 cells that are required to reach the saturation, the length required for a total condensation is about 7 mm. Mainly due to the single sub-iteration and the approximation of the mass source term, condensation is not being instantaneous (not produced in a single cell). In order to reduce the length of the condensation interface there are two possible approaches. On one hand, the number of sub-iterations of the condensation model could be increased, implying a rise in the computational effort as aforementioned. On the other hand, the mesh density could be increased so that not only the condensation length decreases but also the discretization error is reduced in the rest of the transport equations. Even though the latter approach also implies a rise in the computational effort, it is preferable against the first option.

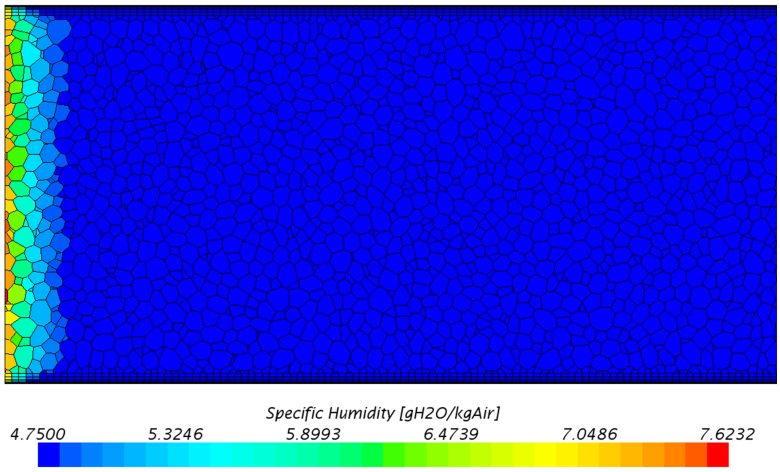

Figure 2.4: Scalar of specific humidity.

It is to be noticed that the premixed conditions of the inlet flow set a worst case scenario where all the condensation process is done almost instantaneously, i.e. in a short length. In realistic applications, the condensation is instead distributed over a wider region, so that the approximations have less impact on the condensation zone thickness, as it is decreased (see Fig. 2.10)

In the next section, the model will be validated thanks to experimental data obtained from a continuous flow turbocharger test bench.

2.5 Validation of the model

The validation process, introduced in section 2.1, determines if the model is faithfully representing the reality [88], and thus its application is useful to solve particular problems. For this purpose, a turbocharger test rig is set up and instrumented, allowing the measurements of different variables within the interest region of the LR-EGR system upstream the compressor, to provide the information required for validating the condensation model. The geometry and the operating conditions of the experiment are replicated with the 3D-CFD software.

2.5.1 Experimental setup

2.5.1.1 Facility

The facility used in this work is based on the turbocharger test bench described by Luján et al. [62] and Tancrez et al. [63]. For this work, the gas stand has been upgraded and is capable to reproduce hot, humid air as EGR. In Fig. 2.5 it is depicted a diagram of the enhanced rig configuration. In first place, air is compressed in a screw compressor and heated up to around 500 °C. Part of this flow is expanded in the turbine, driving power to the compressor. The rest of the hot compressed air is splitted in a three way valve and conditioned to simulate the LR-EGR flow. For doing so, a certain mass flow rate of water is injected within this flow. The water evaporates due to the high temperature of the air and before being re-introduced upstream the compressor, its temperature is reduced in the LR-EGR cooler to a desired value. Separately, air is cooled and dried in a climatic chamber and connected to the compressor intake line. This air simulates cold ambient conditions. As aforementioned, the LR-EGR flow is blown upstream the compressor through a T-joint valve which consists in a simple perpendicular intersection of circular ducts, with flaps to control the mass flow rates. The intake flap was fixed at a high angle.

The instrumentation used allows a continuous measurements of the vari-

ables needed to control the test rig and characterize the region of interest upstream the compressor. The intake air mass flow rate is measured with an engine flow meter mounted in the air box filter. The mass flow rate downstream the compressor is measured using a Vortex flow meter, since the high humidity of the gas made it impossible to use a conventional hot wire/plate flow meter. With those parameters it is possible to calculate the LR-EGR mass flow rate by difference. An inductive PICOTURN compressor speed sensor is mounted in the compressor wheel to measure its spinning rate. A transparent duct is placed at the LR-EGR cooler outlet to assure the absence of water droplets coming from it. Piezoresistive pressure sensors are mounted along the different ducts of the rig. Their specifications are noted in the Table 2.5. For the temperature sensors, K-type thermocouples are used, the specifications of these sensors are listed in the Table 2.6.

Type	Piezoresistive KISTLER RAG25A52BV1H
Range	0 to 5 bar & 0 to 2 bar (comp. inlet)
Output signal	0... 10 V

Table 2.5: Pressure sensors specifications.

Type	Watlow thermocouple K-type
Range	-200 to 1270 °C
Output signal	41 μV/°C

Table 2.6: Thermocouples specifications.

2.5.1.2 Description of durability test

Including the aforementioned T-joint configuration, which will be used as a baseline, seven durability tests of 50 hours are performed with different geometries and flaps in order to assess a potential compressor wheel damage and thus, provide data for validation. For this, an actual engine operating point is replicated in terms of compressor mass flow, EGR rate and specific humidity of the exhaust gases that would be generated during the combustion. Fresh dry air is taken from a climatic chamber at temperatures below 0 °C. The EGR rate is fixed to be 15%, a common value for the selected operating point.

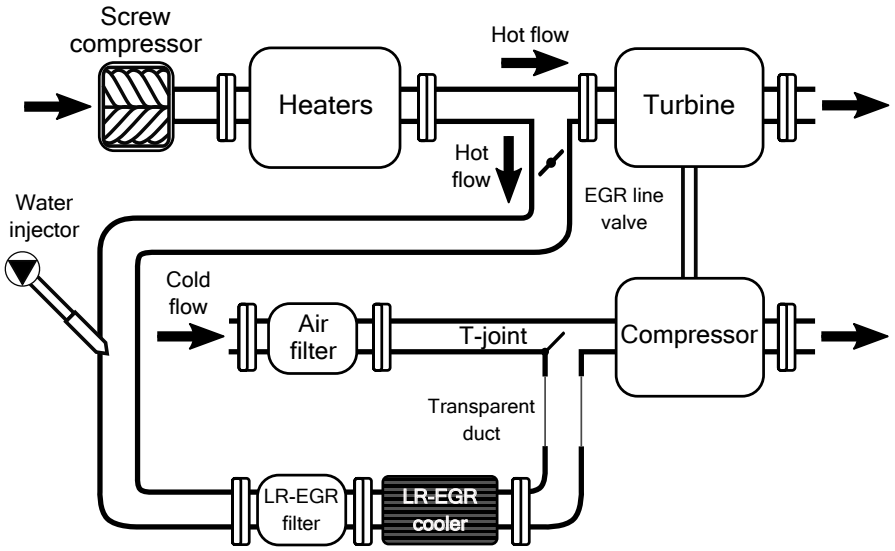

Figure 2.5: Diagram of the continuous flow turbocharer test rig with water injection for humid EGR gas replication.

For the characterization of the problem that is addressed in this work, the duct between the LR-EGR discharge and the compressor inlet is instrumented with a thermocouple that can be moved to measure different points contained in a cross-section plane in the mixing region, 55 mm downstream of the LR-EGR discharge duct axis. These measurement points are distributed following a cross pattern including one in the center, resulting in a total of 5 points. The temperature measurement at each point is performed during 10 hours.

The pressure drop introduced by the T-joint system is also measured placing a piezoresistive pressure sensor in the air box filter and another in the compressor inlet. The pressure drop will be compared with the pressure drop generated by the same T-joint when the intake flap is removed.

Finally, at the end of the 50 testing hours, the T-joint is removed from the compressor inlet and a picture of the state of the compressor wheel is taken, evaluating if there is erosion or damage on the inducer.

2.5.2 Numerical configuration

In this part, the influence of different parameters of the 3D-CFD simulation setup on the performance of the condensation model implemented within the software is assessed. In the end, the robustness of the condensation model to changes of these parameters is tested. In addition, an optimized setup is selected for the rest of the validation process.

2.5.2.1 Geometry and baseline setup

The modeled geometry represents the actual T-joint valve used in the experimental part of this work. This kind of T-joint has been widely used previously to study the mixing process of two streams in order to assess the accuracy of different turbulent approaches [67].

A preliminary study was conducted to determine the length of the ducts required to define the numerical domain. It was found that three intake diameters upstream the intake flap and two EGR duct diameters upstream the EGR flap are required so that the boundary conditions do not affect the domain of interest, allowing a proper development of the flow before reaching the respective flap. In addition, the results presented a low sensitivity to the value of turbulence intensity imposed at the boundary conditions, and hence a standard value of 4% is used. Finally, five intake diameters are extruded downstream the intake flap in order to be able to observe a fair length of the mixing process between both flows. A detailed view of the geometry is showed in Fig. 2.6.

An initial numerical setup is required to be used as a baseline for the sensitivity analyses. The segregated solver of STAR-CCM+® [78] is considered through this work. The coupled solver was not considered since Mach number in this application does not exceed values of 0.3. The domain is composed by a mesh of 0.5M polyhedral cells. Viscous sublayer resolution is sought, so that y^+ values of unity are intended in the wall cells. For this purpose, a prism layer configuration is set. A Reynolds Averaged Navier-Stokes approach for the turbulence solver is chosen, closing the equation system with the Standard $k-\epsilon$ submodel [102, 103]. Costa et al. [104] used this model to simulate mixing processes as well. Both inlets are configured with a mass flow inlet boundary condition, whereas static pressure is set at the outlet of the

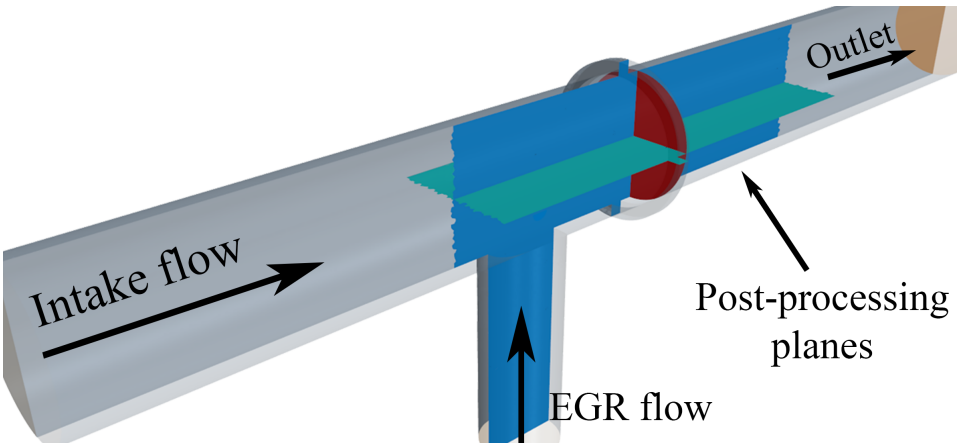

Figure 2.6: Numerical domain and post-processing planes of the selected LR-EGR geometry.

T-joint. These boundary values are obtained averaging their correspondent magnitude of the experimental test. Steady-state calculations are considered, thus sparing the time discretization. Heat transfer with the surroundings is neglected, so that the walls are regarded as adiabatic. The centrifugal compressor existing downstream the T-joint is omitted in the simulations for the sake of computational cost, so it is assumed that it does not affect the mixing process nor the condensation rate.

2.5.2.2 Mesh independence

The sensitivity study starts with the assessment of the mesh independence. For this, the aforementioned reference case is considered and two additional meshes are proposed. Since the reference one has 0.5 M cells, a coarse mesh of 0.1 M cells and a fine mesh of 2 M are generated. The base size of the cells is modified in order to find a mesh with the desired number of cells. This implies that other cell-related parameters are scaled with the base size such as the prism layer thickness or the surface size. Starting from the coarse mesh, the grid refinement for obtaining a fine mesh is therefore *substantial* and performed in a *systematic* way, as suggested by Ferziger and Perić [105].

After iterating the solutions until achieving convergence, imbalances of the transport equation are used for the comparison. Air and water mass imbal-

ances are calculated using Eqs. 2.14 and 2.15 and for the energy imbalance, Equation 2.16 is used.

$$\epsilon_{\text{air}}(‰) = \frac{\dot{m}^{\text{in}}_{\text{air}} + \dot{m}^{\text{EGR}}_{\text{air}} - \dot{m}^{\text{out}}_{\text{air}}}{\dot{m}^{\text{in}}_{\text{air}} + \dot{m}^{\text{EGR}}_{\text{air}}} \cdot 1000 \tag{2.14}$$

$$\epsilon_{\text{water}}(‰) = \frac{\dot{m}^{\text{in}}_{\text{vap}} + \dot{m}^{\text{EGR}}_{\text{vap}} - \left(\dot{m}^{\text{out}}_{\text{vap}} + \dot{m}^{\text{out}}_{\text{water}}\right)}{\dot{m}^{\text{in}}_{\text{vap}} + \dot{m}^{\text{EGR}}_{\text{vap}}} \cdot 1000 \tag{2.15}$$

$$\epsilon_{\text{ener.}}(‰) = \frac{h^{\text{in}}\dot{m}^{\text{in}} + h^{\text{EGR}}\dot{m}^{\text{EGR}} - h^{\text{out}}\dot{m}^{\text{out}} + \int_V S_{\text{ener.}}\,\mathrm{d}V}{h^{\text{in}}\dot{m}^{\text{in}} + h^{\text{EGR}}\dot{m}^{\text{EGR}}} \cdot 1000 \tag{2.16}$$

The condensation rate is normalized with the dry air mass flow rate, showed in Eq. 2.17.

$$\hat{\dot{m}}_{\text{water}} = \frac{\dot{m}^{\text{out}}_{\text{water}}}{\dot{m}^{\text{in}}_{\text{air}} + \dot{m}^{\text{EGR}}_{\text{air}}} \cdot 1000 \tag{2.17}$$

A summary of the results obtained in this study is shown in Table 2.7.

Millions of cells (-)	**0.1**	**0.5 (ref)**	**2**
$\boldsymbol{\epsilon_{\text{air}}(‰)}$	0.74	0.01	0.05
$\boldsymbol{\epsilon_{\text{water}}(‰)}$	0.87	0.18	0.20
$\boldsymbol{\epsilon_{\text{ener.}}(‰)}$	2.20	0.99	1.06
$\boldsymbol{\hat{\dot{m}}_{\text{water}}\left(\frac{g_{\text{water}}}{kg_{\text{air}}}\right)}$	1.79	1.80	1.80
$\boldsymbol{\epsilon_{\text{water}}(‰)}$	19.2	3.1	-

Table 2.7: Imbalances and condensation rate results of mesh independence study.

Considering the imbalances, the discretization error of the coarse mesh is significantly larger than that obtained by the other meshes, even though all of them are below a tight threshold. Table 2.7 also shows the ultimate result of the simulation, namely the condensation rate. In this way, relative error of the condensation rate predicted by the reference mesh against the finest one is only 3‰, whereas the coarsest mesh increases this error by a order of magnitude.

As Table 2.7 only provides quantitative global results of the simulations, in Figure 2.7 it is depicted the temperature distribution in the cross-section planes of the main duct (see Fig. 2.6), downstream of the intake flap. It can be observed the similarities between the fine mesh and the reference one, whereas the coarse mesh presents clear differences in the temperature distribution, implying a poorly accurate solution. It is obvious that the fine grid should present a lower discretization error, but it is not worth using it due to the greater computational effort it requires. Hence, the base size of the reference 0.5 million cell mesh is kept since it presents the best trade-off.

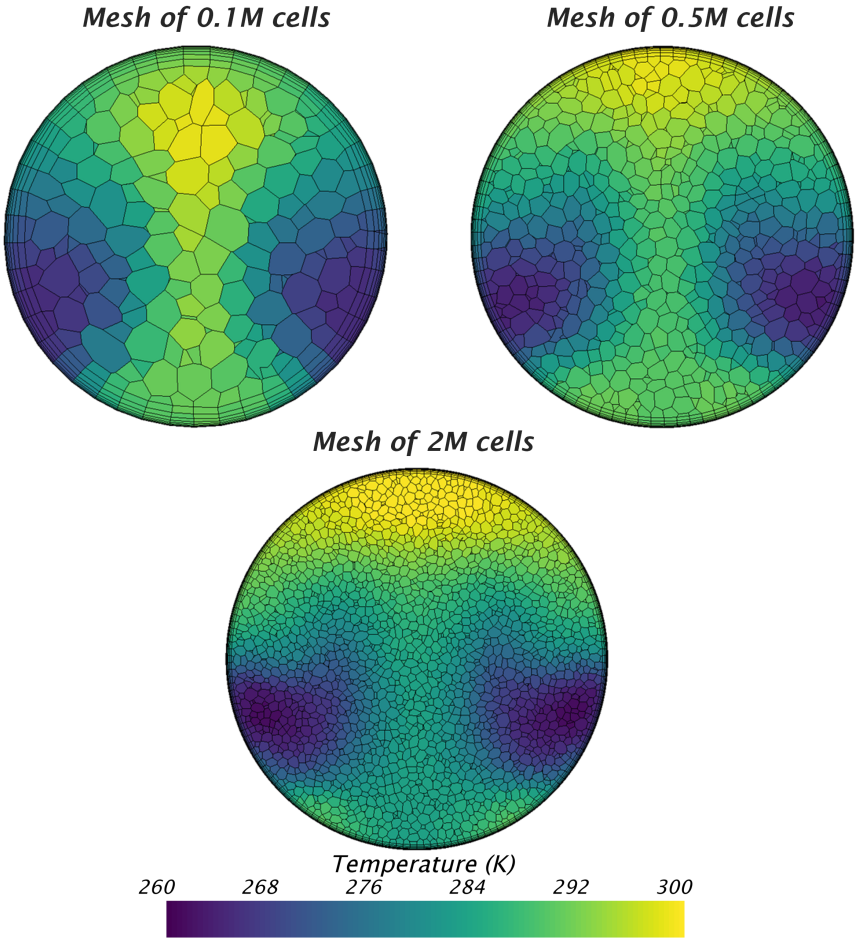

Figure 2.7: Temperature field in the cross-section 55 mm downstream the EGR axis.

2.5.2.3 Time discretization

The next step consists in studying the influence of the time discretization on the simulation results. The reference case is set as steady, thus a transient discretization is going to be analyzed by imposing different time steps. To have an order of magnitude of the shedding frequency of the vortices generated downstream the intake flap, the Strouhal dimensionless number is considered (Eq. 2.18), which links this frequency with the flow rate parameters.

$$St = \frac{fr\, l}{U} \tag{2.18}$$

To calculate the frequency, the characteristic Strouhal number of the problem ought to be estimated in first place. With the study performed by Chen and Fang [106] about the Strouhal numbers of flat inclined flaps in free streams, it is obtained a Strouhal of 0.2 for the current case. Using the definition of the Strouhal number (Eq. 2.18), the minor axis of the projection of the flap on a cross section as a characteristic length and the velocity of the flow at a common operating condition, a frequency can be calculated. The shedding frequency of vortices is around 120 Hz, hence imposing a resolution of forty time steps for each oscillation, the time step should be around $2{\cdot}10^{-4}$ s. From this value, two additional cases are proposed with a quarter and a tenth of that time step ($5{\cdot}10^{-5}$ s, $2{\cdot}10^{-5}$ s).

Following the same process that in the previous step, in Table 2.8 are summarized the imbalance results and the condensation rate at the outlet of each case, considering time-averaged results.

Time step (ms)	**Steady (ref)**	**0.2**	**0.05**	**0.02**
$\epsilon_{\mathbf{air}}$(‰)	0.01	0.09	0.21	0.37
$\epsilon_{\mathbf{water}}$(‰)	0.18	2.55	0.86	1.28
$\epsilon_{\mathbf{ener.}}$(‰)	0.99	1.43	1.58	1.53
$\hat{\dot{m}}_{\mathbf{water}}(\frac{g_{\mathbf{water}}}{kg_{\mathbf{air}}})$	1.80	1.80	1.80	1.79
$\epsilon_{\mathbf{water}}$(‰)	10.1	8.6	2.2	-

Table 2.8: Imbalances and condensation rate results of time step sensitivity study.

Reduced imbalances are found for all these cases. Compared with the

steady reference case, the transient cases behave slightly worse in terms of imbalances. The error in condensation rate of the steady solution compared with the smallest time step transient calculation ($\Delta t = 2 \cdot 10^{-5}\ s$) is around 1% (see Table 2.8). For the case studied, the increase of computational effort to conduct transient simulations is not worth it. The steady-state solver presents little error since the flow solution is quite stable. For other configurations, consisting in different geometries or operating conditions, unsteady phenomena such as flow detachment may appear. In such cases, the residuals would present significant oscillations when attempted to be simulated with a steady solver. A transient solver should be rather used, conducting a time step sensitivity analysis such as the one presented in Table 2.8.

2.5.2.4 Turbulence approach

Regarding the turbulence modeling, no scale-resolving methods are assessed in this work due to the substantial increase of computational effort that they would require. As aforementioned, the RANS Standard $k-\epsilon$ closure model is used for the reference case, since it is widely used in flow mixing problems. In addition to this model, another RANS closure model is tested, the $k-\omega$ SST model [107]. The shear stress transport (SST) equations combine the use of the $k-\omega$ model in the inner parts of the boundary layer and the $k-\epsilon$ model in the free-stream. This model claims to provide a better solution to adverse pressure gradient conditions [107], such as those found downstream of the flaps.

In the same manner as in the previous comparisons, in Table 2.9 are summarized the results of the imbalances and condensation rates of the different turbulence approaches used.

Turbulence model	**k-e(ref)**	**k-w SST**
$\epsilon_{\mathbf{air}}(‰)$	0.01	0.04
$\epsilon_{\mathbf{water}}(‰)$	0.18	0.04
$\epsilon_{\mathbf{ener.}}(‰)$	0.99	1.55
$\hat{\dot{m}}_{\mathbf{water}}(\frac{g_{\mathbf{water}}}{kg_{\mathbf{air}}})$	1.80	1.88

Table 2.9: Imbalances and condensation rate of different turbulence approaches.

Low errors in the imbalances are found for both turbulent approaches. The

slightly higher condensation rate can be due to local flow resolving differences inherent to the turbulence model. Nevertheless, the difference in condensation rate is below 4%, so the impact of the turbulence approach is not excessively significant. The election of the RANS turbulent model depends thus on external parameters that are not related with the condensation model but with the flow problem. In this case it is chosen to solve future simulations with the $k-\omega$ model since it presents a wider usage during the latest years in automotive gas exchange 3D-CFD simulations.

2.5.2.5 Flap angle

During the experimental tests it was observed an important sensitivity of the flap angle in the temperature distribution downstream the mixing region. This change in the temperature profile is caused by a modification of the flow structure within the mixing region, since each stream has a different temperature. Changes in the flow structure imply different mixing behaviors and hence, different condensation rates. So it is important to estimate the impact of this sensitivity with the simulations.

A swept in flap angle is defined varying around the tested angle (74°) from 65° to 83° by steps of 3°, resulting in a total of 7 cases. For the rest of the setup, the baseline configuration is used with $k-\omega$ SST as turbulence submodel. So in this case, the results that are compared are concerning the flow structure (temperature distribution and condensation rate) and pressure drop.

The pressure drop is calculated subtracting the pressure difference of the intake inlet and a cross section plane downstream the mixing region of a flapless configuration case to the pressure difference of a case with a certain flap angle. The results are showed in Table 2.10.

Flap angle	**65°**	**68°**	**71°**	**74°**	**77°**	**80°**	**83°**
Δp(mbar)	39.2	41.7	45.1	47.7	50.8	54.4	57.6

Table 2.10: Pressure drop generated by the flap at different angles.

Within this range, the pressure drop behaves linearly with the flap angle. In addition, the impact of a small modification of the flap angle on the pressure

drop is significant, implying a strong modification of the flow structures and the mixing process.

Concerning the flow structures, a good indicator is the temperature distribution in a cross section plane within the mixing region. For the next comparison, contour planes are made coinciding with the position of the thermocouple in the tests, as will be used in the validation afterwards. In Fig. 2.8 it is depicted the temperature contours at that said section position for three angle positions, namely 65°, 74° (reference case) and 83°.

From the different temperature distributions it can be concluded, as stated previously, that the flow structures are very permeable to the flap angle. In this case, the EGR flow reaches the top part of the T-joint duct with higher flap angles. The closest position of the flap prevents the intake flow of transferring momentum to the EGR flow (hotter), implying a smaller deflection. The absence of deflection also generates a recirculating region right upstream the EGR flow discharge.

Finally, to conclude the sensitivity study, the impact of the flap angle in the condensate production is conducted. In Fig. 2.9 the normalized condensation rate of the same flap angles previously proposed is shown. In addition, the normalized condensation rate with perfect mixing conditions [41] is showed, highlighting that if given enough distance, both streams mix completely and the solution tends to the solution of the perfect 0D mixing model.

In spite of the differences in the flow structures found in the previous studies, their repercussion on the normalized condensation rate may not be such clear. In this case, the mixing processes generated by flap angles between 65° and 74° lead to similar normalized condensation rates. However for higher flap angles a slight reduction of normalized condensation rate is observed. It can be inferred that a particular normalized condensation rate is associated to each flow structure, and no linear behavior may be found between geometrical parameters and the normalized condensation rate produced. Moreover, the flow structures are sensitive to the geometry, so special attention may be paid when trying to reproduce actual geometries.

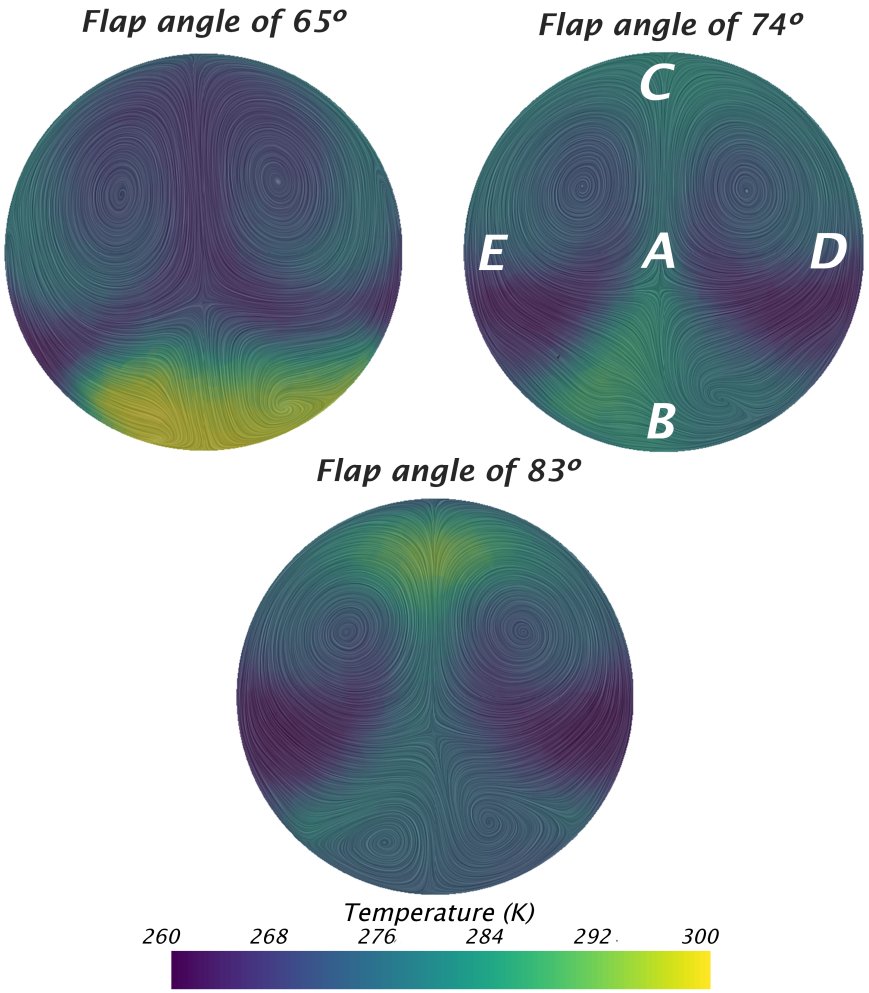

Figure 2.8: Temperature field on a cross section 55 mm downstream the intake flap.

2.5.3 Validation results

From the sensitivity study it is obtained the base configuration which is used for the validation. As aforementioned, it is selected the reference mesh in steady state conditions with a $k-\omega$ SST turbulence approach. The boundary conditions imposed are obtained averaging their value during the experimental test. The validation of the model using experimental data is addressed com-

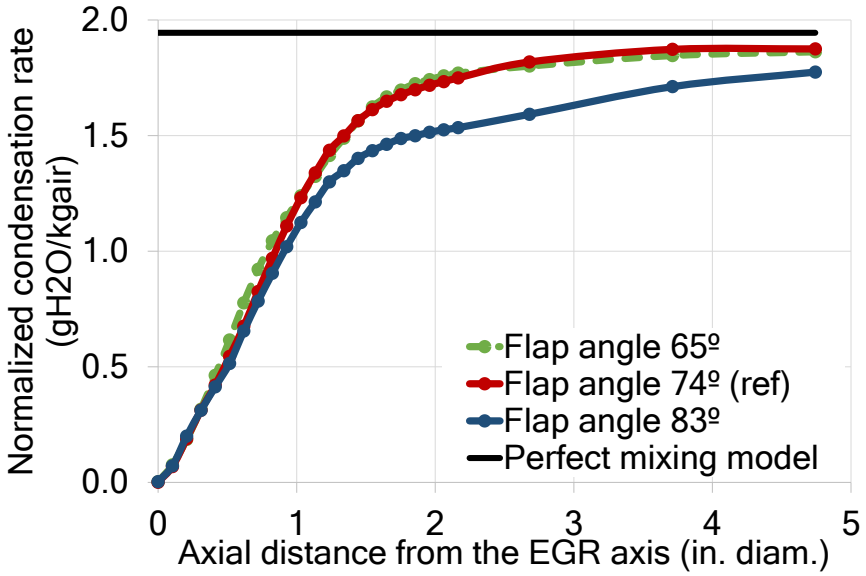

Figure 2.9: Normalized condensation rate results of flap angle study compared with perfect mixing solution.

paring the pressure drop of the T-joint and the temperature distribution in the section plane introduced previously. In addition, a qualitative comparison between the erosion observed in the compressor wheel of seven different T-joint configurations, after 50-hour durability tests, and their modeled condensation rate in the inducer plane is performed, completing the validation assessment.

First, the error in pressure drop generated by the flap relative to the averaged pressure drop of the test is shown in Table 2.11. As aforementioned, these values are obtained subtracting the pressure drop of a flap-less configuration to each case, for both modeled and tested configurations.

Flap angle	**65°**	**68°**	**71°**	**74°**	**77°**	**80°**	**83°**
Δp error(%)	-23	-19	-12	-7	-1	6	12

Table 2.11: Relative error of pressure drop generated with different flap angles.

The results show that the pressure drop of the test is closer to the simulation case of the flap angle of 77°. Despite of the small error in angle, the uncertainty of the pressure drop is noticeable. This error may be produced by

the simplifications of the 3D model, the flap angle uncertainty, the uncertainty of the pressure sensors and the numerical solver itself, so this result is accepted as valid.

Next, the temperature measurements at the compressor inlet are compared with the results of the simulation. Each temperature value has been obtained averaging during 10 hours of testing. In Fig. 2.8 it is highlighted the zones at the cross-section where the thermocouple was actually placed. In Table 2.12 the comparison between the measurements and simulations of the different flap angles is shown. With this results the uncertainty of the flap angle during the testing is clarified, verifying if the test coincide with the measured angle.

	Test	**CFD simulation error (K)**				
Point	**Temp (K)**	**65°**	**68°**	**71°**	**74°**	**77°**
A	296	-9	**0**	-1	5	5
B	296	8	3	4	**1**	**-1**
C	272	**0**	6	6	9	12
D	268	5	**0**	**0**	**0**	-1
E	271	1	**0**	**0**	-2	-2

Table 2.12: Relative comparison between the temperature measurements and the CFD simulation.

As previously stated, due to the high sensitivity of the flow structure to the flap angle, the uncertainty of this position during the testing and the uncertainty of the thermocouples, the temperature distribution changes importantly with the flap position. For the study of the flap angle, it turns out that the solution of test measurement coincide with the simulation cases with flap angles between 68° and 74°, close to the imposed flap angle. Since the condensation model affects the temperature values through the source term of the energy transport equation, it can be concluded that this results are in good agreement with the experimental data.

Finally, durability tests are performed with seven different T-joint configurations. The presence of erosion on the leading edges is compared with the condensation rate predicted by the model using each actual geometry. Table 2.13 summarizes these results. The condensation rates are normalized with the threshold case that produced a slight erosion on the impeller.

Norm. condensation rate	**Observed erosion**
(−)	(−)
1.48	Yes
1.41	Yes
1.11	Yes
1	Slight
0.98	No
0.78	No
0.58	No

Table 2.13: Comparison between the erosion observed on the leading edges after 50 hours of durability test and the modeled condensation rate of seven different T-joint valve configurations.

Three of the configuration tested produced a noticeable erosion on the leading edges of the compressor wheels. These cases also produced the highest condensation rates when modeled with the developed model. In the same way, the three configurations that showed no erosion after the durability tests obtained the lowest condensation values according to the prediction of the model. A configuration in between of the previous ones in terms of predicted condensation rate showed slight erosion marks in some of the leading edges, implying closeness to an erosion threshold for the operating point used.

Taking into account the uncertainties of the numerical model and the experiment, with the quantitative and qualitative comparisons made above, the validity of the model to represent the condensation phenomena with confidence is proven.

To further understand the mixing process and the sensitivity of the geometrical parameters to the condensation rate, other significant results of the simulation are exposed next. In Fig. 2.10 are highlighted the cells where condensation is taking place. These cells define an interface between both intake and EGR flows in the first part of the mixing region, then as the flow advances through the duct and mixes, condensation keeps occurring until equilibrium conditions are reached when the whole flow is saturated. The color field denotes the vapor source term that is vanishing in a given cell.

Once the vapor has condensed, the passive scalar increases to keep track-

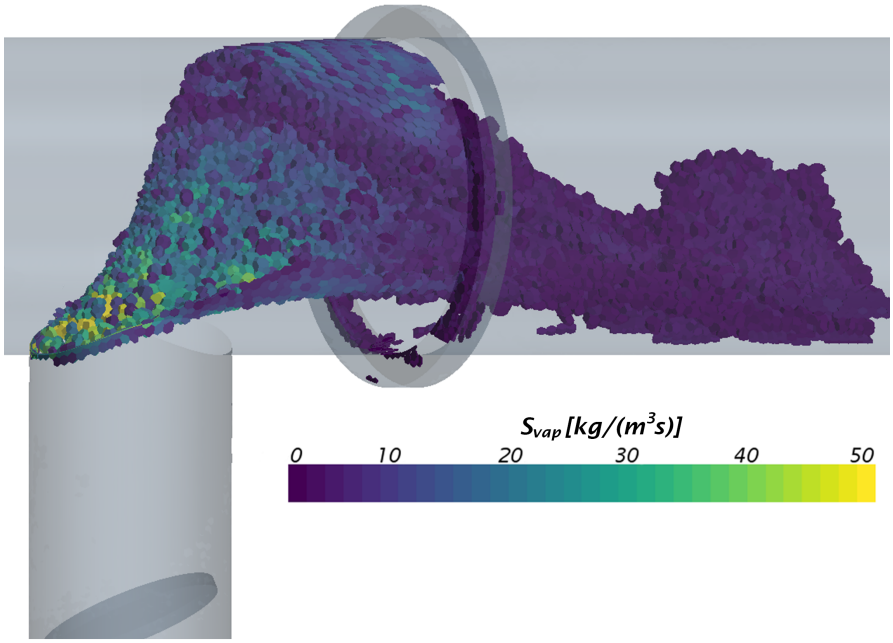

Figure 2.10: Local condensation region with color field of vapor source value.

ing of the water as it travels within the flow. Thanks to the passive scalar options available, realistic diffusive and convective properties may be enabled, presenting a homogenization process through the duct. In Fig. 2.11 it is shown this water homogenization process in top and side sections of the valve (see Fig. 2.6).

In order to analyze which flow structures are responsible of the mixing process, in Fig. 2.12 are represented the streamlines of the EGR flow. A recirculating region is generated downstream the EGR flow discharge due to the low momentum passing through this area. So, the EGR flow is moved to the top zone of the duct. In addition, the intake flap generates two symmetric vortices which contribute suctioning the EGR flow and the mixing process. These flow structures are quite stable, so that the mixing keeps occurring continuously as the flow travels downstream.

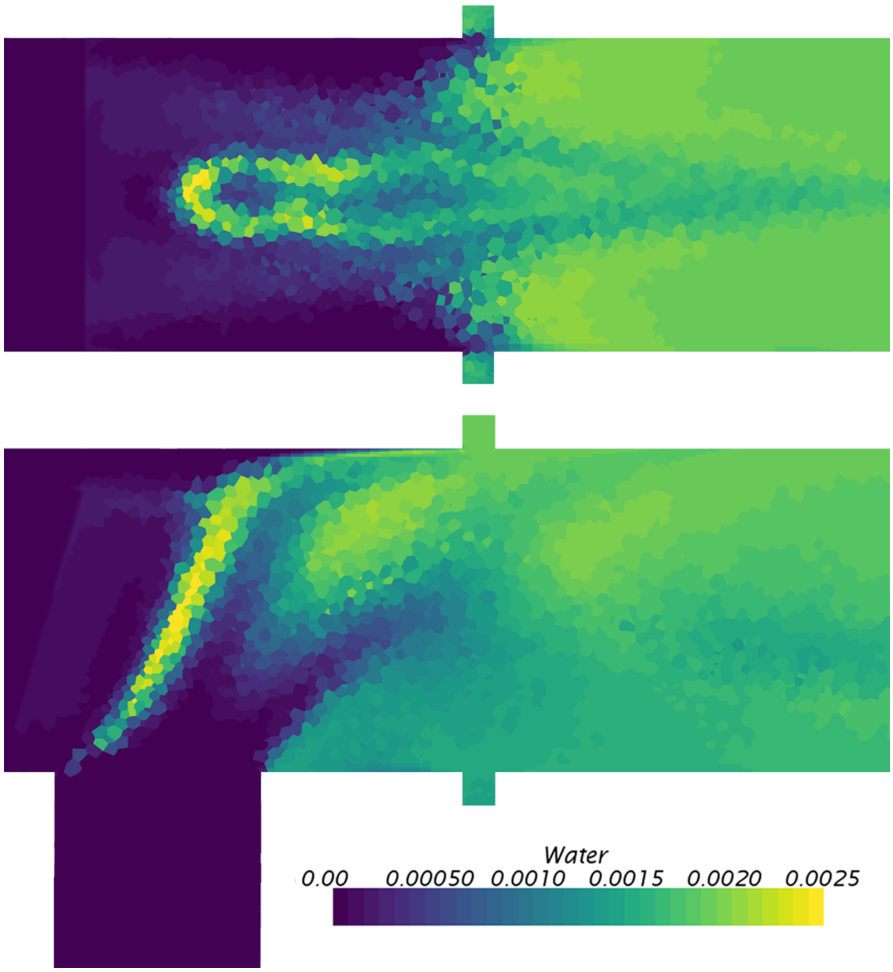

Figure 2.11: Top and side section planes of water passive scalar fraction field.

2.6 Conclusions

A collection of suitable source terms to model water condensation in humid air stream have been developed and implemented within the code of the commercial 3D-CFD software STAR-CCM+® [78]. The capabilities and limitations of the model have been exposed, and fulfill the requirements and objectives regarding computational cost and accuracy in the condensation prediction in LR-EGR systems. A previously validated 0D perfect mixing system of balance

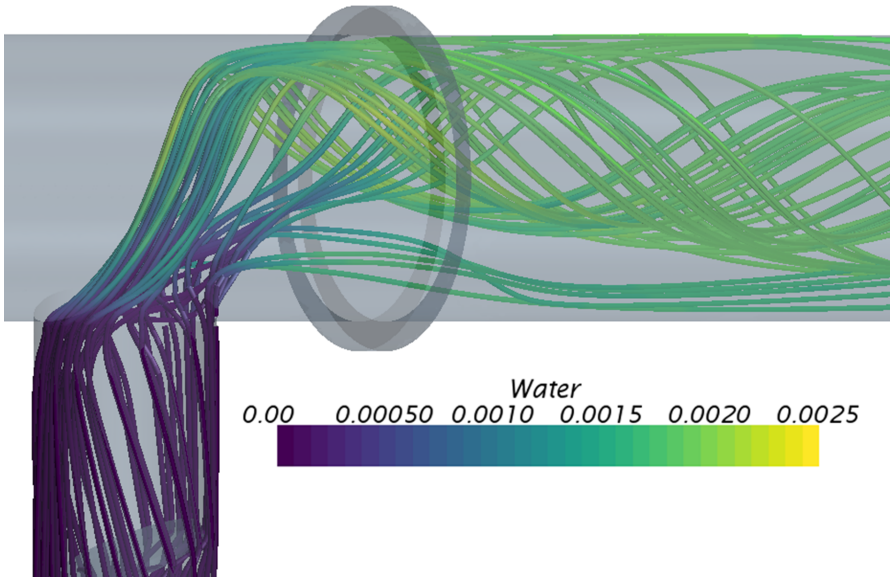

Figure 2.12: Streamlines of the EGR flow with color field of water passive scalar fraction.

equations has been used in order to compare the global results of the simulation with analytical solutions for a wide range of boundary conditions in terms of specific humidity and temperatures, obtaining good agreement. Therefore, the implementation of the condensation submodel in STAR-CCM+ is verified.

A sensitivity study and a validation process have been performed of the verified condensation model. A turbocharger test rig has been set up and instrumented. A testing procedure has been designed to allow a quantitative and qualitative validation of the condensation phenomena, using pressure drop, temperature pattern in a section plane in the mixing region and evaluating the compressor wheel erosion of seven T-joint configurations. A baseline T-joint geometry has been simulated in order to assess the behavior of the model. The agreement found between the simulated and tested results proved the validity of the model. The sensitivity study added meaningful value to the robustness of the model against different setup variations.

The results showed a significant sensitivity of the mixing flow structures to the intake flap angle. Special attention must be paid of this parameter, since the mixing process controls the condensation rate and hence, the damage of

the compressor wheel. The influence of this geometrical constraint can be extended to the whole geometry, thus a proper 3D modeling of each particular configuration is recommended, reproducing its actual geometry as much as possible. A correlation has been proved between the condensation rate predicted by the model and the detection of erosion after performing a durability test with the same geometrical configuration and operating conditions.

The applications of this model can be extended beyond the seen LR-EGR condensation prediction to any kind of problem where due to psychrometric reasons, vapor may condense into liquid water. Further studies may include an evaporation model that complements the condensation model or a wall condensation model. For considering water droplets modeling, a different solver would be needed, such as a Lagrangian approach.

Next, in Chapter 3, the influence of the compressor wheel on the mixing process and condensation generation will be assessed. The compressor will be modeled as well, facing thus a more complex numerical problem and assessing the correct behavior of the condensation model in that said situation.

Chapter 2 Bibliography

[19] A. Cairns, N. Fraser, and H. Blaxill. "Pre versus post compressor supply of cooled EGR for full load fuel economy in turbocharged gasoline engines." In: *SAE Technical Paper*. 2008. DOI: 10.4271/2008-01-0425 (cit. on pp. 4, 27).

[20] J. M. Luján, H. Climent, R. Novella, and M. E. Rivas-Perea. "Influence of a low pressure EGR loop on a gasoline turbocharged direct injection engine." *Applied Thermal Engineering* 89 (2015), pp. 432–443. DOI: 10.1016/j.applthermaleng.2015.06.039 (cit. on pp. 4, 27).

[28] J. R. Serrano, X. Margot, A. Tiseira, and L. M. García-Cuevas. "Optimization of the inlet air line of an automotive turbocharger." *International Journal of Engine Research* 14(1) (2013), pp. 92–104. DOI: 10.1177/1468087412449085 (cit. on pp. 6, 9, 28, 96).

[30] S. J. Kim and H. C. No. "Turbulent film condensation of high pressure steam in a vertical tube." *International Journal of Heat and Mass Transfer* 43(21) (2000), pp. 4031–4042. DOI: 10.1016/S0017-9310(00)00015-6 (cit. on pp. 8, 28).

[31] P. Panday. "Two-dimensional turbulent film condensation of vapours flowing inside a vertical tube and between parallel plates: a numerical approach." *International journal of refrigeration* 26(4) (2003), pp. 492–503. DOI: 10.1016/S0140-7007(02)00162-7 (cit. on pp. 8, 28).

[32] J. Liu, H. Aizawa, and H. Yoshino. "CFD prediction of surface condensation on walls and its experimental validation." *Building and Environment* 39(8) (2004), pp. 905–911. DOI: 10.1016/j.buildenv.2004.01.015 (cit. on pp. 8, 28).

[33] L. Vyskocil, J. Schmid, and J. Macek. "CFD simulation of air–steam flow with condensation." *Nuclear Engineering and Design* 279 (2014), pp. 147–157. DOI: 10.1016/j.nucengdes.2014.02.014 (cit. on pp. 8, 28, 31, 70).

[34] D.-Y. Shang and L.-C. Zhong. "Extensive study on laminar free film condensation from vapor–gas mixture." *International Journal of Heat and Mass Transfer* 51(17) (2008), pp. 4300–4314. DOI: 10.1016/j.ijheatmasstransfer.2008.03.004 (cit. on pp. 8, 28).

[35] C. Moses and G. Stein. "On the growth of steam droplets formed in a Laval nozzle using both static pressure and light scattering measurements." *Journal of Fluids Engineering* 100(3) (1978), pp. 311–322. DOI: 10.1115/1.3448672 (cit. on pp. 8, 28, 70).

[36] M. Grubel, J. Starzmann, M. Schatz, T. Eberle, and D. Vogt. "Two-phase flow modeling and measurements in low-pressure turbines-Part 1: Numerical validation of wet steam models and turbine modeling." In: 2014. DOI: 10.1115/GT2014-25244 (cit. on pp. 8, 28).

[37] M. Abarham, T. Chafekar, J. Hoard, D. Styles, and D. Assanis. "A visualization test setup for investigation of water-deposit interaction in a surrogate rectangular cooler exposed to diesel exhaust flow." *SAE Technical Paper* 2012-01-0364 (2012). DOI: 10.4271/2012-01-0364 (cit. on pp. 8, 28).

[38] A. Warey, A. S. Bika, D. Long, S. Balestrino, and P. Szymkowicz. "Influence of water vapor condensation on exhaust gas recirculation cooler fouling." *International Journal of Heat and Mass Transfer* 65 (2013), pp. 807–816. DOI: 10.1016/j.ijheatmasstransfer.2013.06.063 (cit. on pp. 8, 28).

[39] G. Bourgoin, E. Tomas, J. Luján, and B. Pla. "Acidic Condensation in HP EGR Systems Cooled at Low Temperature Using Diesel and Biodiesel Fuels." *SAE Technical Paper* 2010-01-1530 (2010). DOI: 10.4271/2010-01-1530 (cit. on pp. 8, 28).

[40] S. Moroz, G. Bourgoin, J. M. Luján, and B. Pla. "Acidic condensation in low pressure EGR systems using diesel and biodiesel fuels." *SAE Int. J. Fuels Lubr* 2009-01-2805 (2009). DOI: 10.4271/2009-01-2805 (cit. on pp. 8, 28).

[41] J. R. Serrano, P. Piqueras, E. Angiolini, C. Meano, and J. De La Morena. "On Cooler and Mixing Condensation Phenomena in the Long-Route Exhaust Gas Recirculation Line." In: *SAE Technical Paper*. 2015. DOI: 10.4271/2015-24-2521 (cit. on pp. 8, 10, 28, 32, 41, 54, 150).

[42] A. Castorrini, A. Corsini, F. Rispoli, P. Venturini, K. Takizawa, and T. E. Tezduyar. "Computational analysis of wind-turbine blade rain erosion." *Computers & Fluids* 141(Supplement C) (2016), pp. 175 –183. ISSN: 0045-7930. DOI: 10.1016/j.compfluid.2016.08.013 (cit. on pp. 8, 28).

[43] P. Z. John, T. Koka, and S. Dayalan. "Water droplet erosion simulation of a turbocharger compressor wheel." In: *ASME Turbo Expo 2014: Turbine Technical Conference and Exposition*. GT2014-26974. American Society of Mechanical Engineers. 2014 (cit. on pp. 8, 28).

[44] A. Surendran and H. D. Kim. "Effects of Wet Compression on the Flow Behavior of a Centrifugal Compressor: A CFD Analysis." In: *ASME Turbo Expo 2014: Turbine Technical Conference and Exposition*. GT2014-25035. American Society of Mechanical Engineers. 2014, V02DT42A002. DOI: 10.1115/GT2014-25035 (cit. on pp. 8, 28).

[62] J. Luján, V. Bermúdez, J. R. Serrano, and C. Cervelló. "Test bench for turbocharger groups characterization." *SAE Technical Paper* 2002-01-0163 (2002). DOI: 10.4271/2002-01-0163 (cit. on pp. 9, 44, 96).

[63] M. Tancrez, J. Galindo, C. Guardiola, P. Fajardo, and O. Varnier. "Turbine adapted maps for turbocharger engine matching." *Experimental Thermal and Fluid Science* 35(1) (2011), pp. 146–153. DOI: 10.1016/j.expthermflusci.2010.07.018 (cit. on pp. 9, 44).

[67] A. Sakowitz, M. Mihaescu, and L. Fuchs. "Turbulent flow mechanisms in mixing T-junctions by Large Eddy Simulations." *International Journal of Heat and Fluid Flow* 45 (2014), pp. 135–146. DOI: 10.1016/j.ijheatfluidflow.2013.06.014 (cit. on pp. 10, 29, 47).

[74] A. Broatch, J. Galindo, R. Navarro, and J. García-Tíscar. "Numerical and experimental analysis of automotive turbocharger compressor aeroacoustics at different operating conditions." *International Journal of Heat and Fluid Flow* 61 (2016), pp. 245 –255. ISSN: 0142-727X. DOI: 10.1016/j.ijheatfluidflow.2016.04.003 (cit. on pp. 11, 28, 70, 86, 122, 136).

[78] *STAR-CCM+*. Release version 9.04.011. CD-adapco. 2014. URL: http://www.cd-adapco.com (cit. on pp. 12, 29, 30, 35, 36, 47, 60).

[81] F. Posada, A. Bandivadekar, and J. German. "Estimated cost of emission control technologies for light-duty vehicles Part 1-Gasoline." In: *SAE Technical Paper*. 2013. DOI: 10.4271/2013-01-0534 (cit. on p. 27).

[82] F. Posada, A. Bandivadekar, and J. German. "Estimated cost of emission control technologies for light-duty vehicles Part 2-Diesel." In: *SAE Technical Paper*. 2013. DOI: 10.4271/2013-01-0539 (cit. on p. 27).

[83] R. Mobasheri and Z. Peng. "CFD investigation into diesel fuel injection schemes with aid of Homogeneity Factor." *Computers & Fluids* 77(Supplement C) (2013), pp. 12 –23. ISSN: 0045-7930. DOI: 10.1016/j.compfluid.2013.02.013 (cit. on p. 27).

[84] J. M. Luján, H. Climent, V. Dolz, A. Moratal, J. Borges-Alejo, and Z. Soukeur. "Potential of exhaust heat recovery for intake charge heating in a diesel engine transient operation at cold conditions." *Applied Thermal Engineering* 105 (2016), pp. 501–508. DOI: 10.1016/j.applthermaleng.2016.03.028 (cit. on p. 27).

[85] T. V. Johnson. "Review of Vehicular Emissions Trends." *SAE Int. J. Engines* 8 (Apr. 2015), pp. 1152–1167. DOI: 10.4271/2015-01-0993 (cit. on p. 27).

[86] C. Guardiola, B. Pla, P. Piqueras, J. Mora, and D. Lefebvre. "Model-based passive and active diagnostics strategies for diesel oxidation catalysts." *Applied Thermal Engineering* 110 (2017), pp. 962–971. DOI: 10.1016/j.applthermaleng.2016.08.207 (cit. on p. 27).

[87] Y. Patel, T. Turunen-Saaresti, G. Patel, and A. Grönman. "Numerical investigation of turbulence modelling on condensing steam flows in turbine cascade." In: *ASME Turbo Expo 2014: Turbine Technical Conference and Exposition*. American Society of Mechanical Engineers. 2014, V01BT27A035–V01BT27A035 (cit. on pp. 29, 72).

[88] H. K. Versteeg and W. Malalasekera. *An introduction to computational fluid dynamics: the finite volume method*. 2nd ed. Harlow: Pearson Education Limited, 2007 (cit. on pp. 29, 40, 44).

[89] AIAA. *Guide for the Verification and Validation of Computational Fluid Dynamics Simulations*. Vol. G-077-1998. AIAA, 1998. DOI: 10.2514/4.472855.001 (cit. on p. 29).

[90] W. L. Oberkampf and T. G. Trucano. "Verification and validation in computational fluid dynamics." *Progress in Aerospace Sciences* 38(3) (2002), pp. 209–272. ISSN: 0376-0421. DOI: 10.1016/S0376-0421(02)00005-2 (cit. on p. 29).

[91] P. J. Roache. *Verification and validation in computational science and engineering*. Vol. 895. Hermosa Albuquerque, NM, 1998 (cit. on pp. 29, 40).

[92] S. P. Veluri, C. J. Roy, and E. A. Luke. "Comprehensive code verification techniques for finite volume CFD codes." *Computers & Fluids* 70(Supplement C) (2012), pp. 59 –72. ISSN: 0045-7930. DOI: 10.1016/j.compfluid.2012.04.028 (cit. on pp. 29, 40).

[93] S. Sen, M. Selokar, D. Nisad, and K. Kishore. "Design and Development of Demisting Device of a Commercial Vehicle and its Numerical as Well as Experimental Validation." In: *SAE Technical Paper*. 2016. DOI: 10.4271/2016-01-0217 (cit. on p. 30).

[94] *Psychrometric Chart - Structure and Application*. Siemens Building Technologies Group, 2014. URL: www.siemens.com (cit. on pp. 30, 32, 34).

[95] D. C. Shallcross. "Psychrometric charts for water vapour in natural gas." *Journal of Petroleum Science and Engineering* 61(1) (2008), pp. 1–8. DOI: 10.1016/j.petrol.2007.10.002 (cit. on pp. 30, 32, 34).

[96] M. J. Moran, H. N. Shapiro, D. D. Boettner, and M. B. Bailey. *Fundamentals of engineering thermodynamics*. John Wiley & Sons, 2010 (cit. on pp. 32, 86).

[97] G. Ferron and S. Soderholm. "Estimation of the evaporation or stabilization times of water droplets." *Journal of Aerosol Science* 18(6) (1987), pp. 639 –642. ISSN: 0021-8502. DOI: 10.1016/0021-8502(87)90086-3 (cit. on p. 34).

[98] H. Barrow and C. Pope. "Droplet evaporation with reference to the effectiveness of water-mist cooling." *Applied Energy* 84(4) (2007), pp. 404 –412. ISSN: 0306-2619. DOI: 10.1016/j.apenergy.2006.09.007 (cit. on p. 34).

[99] D. R. Stull. "Vapor pressure of pure substances. Organic and inorganic compounds." *Industrial & Engineering Chemistry* 39(4) (1947), pp. 517–540. DOI: 10.1021/ie50448a022 (cit. on p. 35).

[100] Y. Tominaga and T. Stathopoulos. "Turbulent Schmidt numbers for CFD analysis with various types of flowfield." *Atmospheric Environment* 41(37) (2007), pp. 8091 –8099. ISSN: 1352-2310. DOI: 10.1016/j.atmosenv.2007.06.054 (cit. on p. 39).

[101] D. C. Wilcox. "Reassessment of the scale-determining equation for advanced turbulence models." *AIAA journal* 26(11) (1988), pp. 1299–1310. DOI: 10.2514/3.10041 (cit. on p. 40).

[102] D. C. Wilcox. *Turbulence Modeling for CFD (Hardcover)*. 3rd ed. La Cañada, California: Dcw Industries Inc., 2006 (cit. on p. 47).

[103] W. Jones and B. Launder. "The prediction of laminarization with a two-equation model of turbulence." *International Journal of Heat and Mass Transfer* 15(2) (1972), pp. 301–314. DOI: 10.1016/0017-9310(72)90076-2 (cit. on p. 47).

[104] J. Costa, L. Oliveira, and D Blay. "Test of several versions for the k–ε type turbulence modelling of internal mixed convection flows." *International Journal of Heat and Mass Transfer* 42(23) (1999), pp. 4391–4409. DOI: 10.1016/S0017-9310(99)00075-7 (cit. on p. 47).

[105] Ferziger, J.H. and Perić, M. *Computational Methods for Fluid Dynamics*. 3rd rev. Berlin: Springer, 2002 (cit. on p. 48).

[106] J. M. Chen and Y.-C. Fang. "Strouhal numbers of inclined flat plates." *Journal of wind engineering and industrial aerodynamics* 61(2) (1996), pp. 99–112. DOI: 10.1016/0167-6105(96)00044-X (cit. on p. 51).

[107] F. R. Menter. "Two-equation eddy-viscosity turbulence models for engineering applications." *AIAA journal* 32(8) (1994), pp. 1598–1605. DOI: 10.2514/3.12149 (cit. on p. 52).

Chapter 3

Influence of compressor on condensation generation

Contents

3.1 Introduction

As introduced in Chapter 2, the compressor inlet plays an important role in the condensation phenomenon. Condensation depends on the flow distribution and turbulence, i.e., how the streams mix. So, a thorough analysis should be addressed using a 3D-CFD approach. Previously, different authors have dealt with similar stream mixing problems [108, 109, 110], condensation modeling [111, 35] or both phenomena [33]. Modeling condensation in the bulk flow due to the mixing of streams at different psychrometric conditions has been scarcely studied due to the lack of applications where this phenomenon is present. In the particular case of condensation produced in a LR-EGR T-joint, the compressor presence as an active element on the process may be of importance. It is known that there are operating conditions where the influence of the compressor affects a substantial region upstream of it, caused either by pressure oscillations [74] or even by recirculated flow [112, 113], as will be explored in Chapter 5. However, modeling the whole compressor along with the LR-EGR T-joint with accuracy implies a computational effort remarkably larger than simulating only the T-joint, as will be shown in Section 3.4.4.

This chapter is meant to study the influence of the compressor on the condensation process and the possibility of decoupling the compressor from the T-joint for the condensation simulation, thus reducing the computational time required. For this, a complete geometry that includes the T-joint and the compressor will be simulated and compared with a simulation of T-joint alone. The commercial CFD code STAR-CCM+ [79] will be used throughout all the study. The condensation model developed and validated in Chapter 2 will be used for the condensation prediction. Parameters such condensation, flow patterns and pressure profiles will be used for the comparison and domain assessment. Finally, the computational effort of both approaches will be compared.

In Section 3.2 the mesh and simulation setups will be detailed and the condensation model summarized. Then, the methodology, including the operating points and specific geometrical configurations, will be explained in Section 3.3. The results and the discussion are written in Section 3.4 and finally, the conclusions are highlighted in Section 3.5.

3.2 Numerical configuration

3.2.1 Geometries and mesh

As aforementioned, there are two main regions of interest in the current study; the LR-EGR junction and the compressor, which together form the complete geometry, as shown in Fig. 3.1. The particular LR-EGR junction selected for this work is a T-joint, as can be seen in Fig. 3.2. It has two perpendicular inlets, one for the intake of fresh cold air (left branch) and one for the warm and humid EGR (bottom branch), with a counter-pressure flap on each one for controlling the ratio of mass flow rates (known as EGR rate). The length of the intake pipes, from each flap to their inlet boundary is three corresponding diameters, as determined in Chapter 2. The T-joint discharges into the compressor wheel (right branch of Fig. 3.2). Figure 3.3 shows that the complete geometry of the compressor is considered, i.e., 360°-resolved wheel, diffuser, volute and outlet duct, which is 5 diameters long [77]. There will be two sets of simulations: Complete domain (T-joint with compressor; Fig. 3.1) and reduced domain (T-joint alone; Fig. 3.2). For the latter, the section at the end of the cone is extruded one and a half diameters, thus reducing the impact of the boundary condition on the solution. The angle of the EGR flap is fixed and the set of angles used for the intake flap will be discussed in Section 3.3.

For the sake of consistency, the meshing approach is kept the same for both regions. The meshes are composed of polyhedral cells, with a base size between 0.8 mm for the critical regions such the compressor wheel and 3 mm for the inlet and outlet ducts. Prism layers are generated on the walls, which improve the solution of the boundary layer. The y^+ value on the walls is about 1, assuring a proper solving of the near-wall flow [114]. Meshing characteristics are in agreement with those corresponding to mesh independence studies of Section 2.5.2.2 and compressor [77]. With these options, the meshes of the complete cases have 12M cells and the reduced cases (T-joint only) have 0.75M cells.

3.2.2 Setup and boundary conditions

Regarding the numerical configuration, the flow is set as multicomponent ideal gas, considering dry air and water vapor as components. The segregated solver

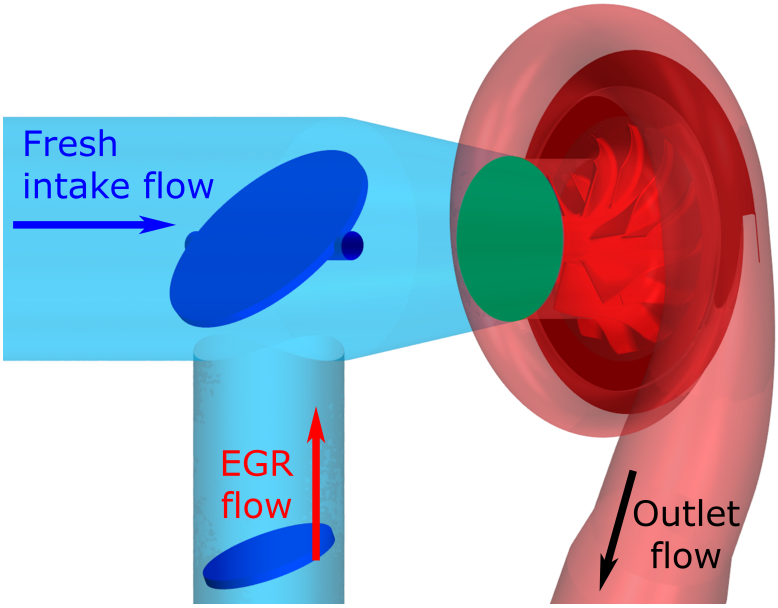

Figure 3.1: Complete region geometry.

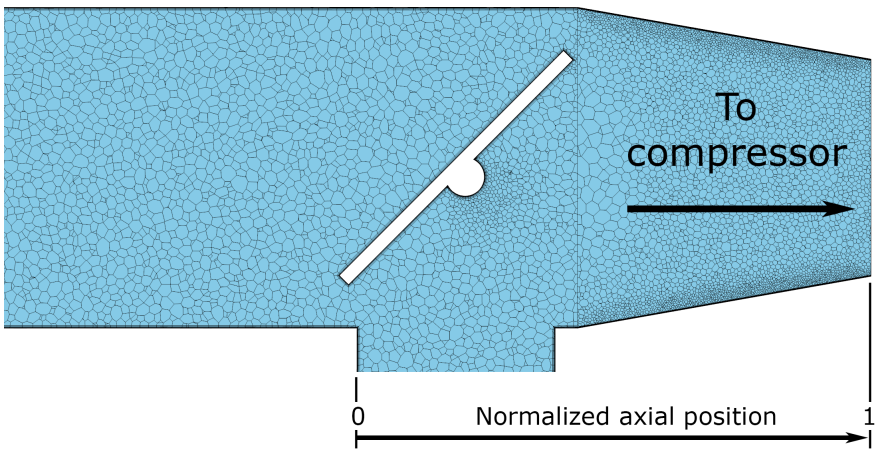

Figure 3.2: LR-EGR T-joint with cross-section of mesh and normalized axis for post-processing.

of STAR-CCM+ [79] is chosen. For the turbulence approach, the Detached Eddy Simulation (DES) model with the $k-\omega$ SST submodel is used [87]. Second-order time discretization is considered, imposing a fixed step of 4 de-

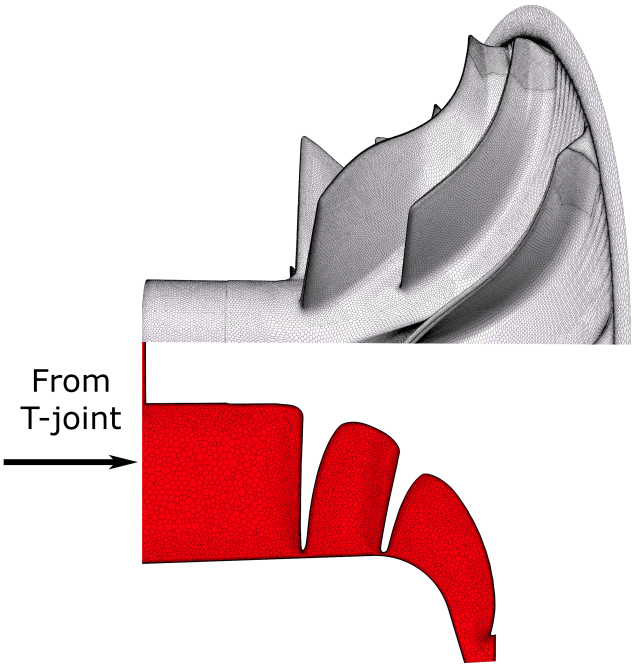

Figure 3.3: Compressor domain and impeller mesh.

grees angle of the compressor wheel, resulting in a time-step size is $4.2{\cdot}10^{-6}$ s. Navarro [77] proved this time step was enough for an accurate prediction of the global variables.

Mass flow inlet boundaries are selected in both fresh air and EGR inlets, specifying additionally the total temperature and the mass fraction of each component. For the cases with the compressor, the values of compressor speed and outlet pressure are required. A radial equilibrium profile is employed at the outlet boundary [115]. For the reduced cases, only the static pressure at the end of the extruded outlet duct is needed. The ratio between the inlet mass flow rates fixes the EGR rate, and the mass fraction of the gas components sets their specific humidity. The values of the boundary conditions are obtained from experimental tests performed in Section 2.5.1.

For the reduced-domain simulations, the outlet pressure values were not actually measured. Instead, the full solutions are simulated first and the pressure at a plane at the end of the inlet cone is averaged and used as a constant and homogeneous value for the reduced cases. This pressure depends on the

operating point and it is not known beforehand, but the sensitivity of the solution to the T-joint outlet pressure is assessed in section 3.4.3.

3.3 Methodology

3.3.1 Numerical campaign

A combination of different operating conditions and geometries are analyzed. Two operating points are combined with three flap angle positions. The first operating point has high intake mass flow rate, low EGR rate and high compressor speed, the second has a low intake mass flow rate, high EGR rate and low compressor speed. The numeration of the cases and the flap angles are shown in the Table 3.1. To assess the influence of the compressor on the condensation process, all six previous configurations will be run for the domains introduced in section 3.2.1, i.e., complete geometry (with compressor) and reduced geometry (without compressor). In these 12 simulations several performance indicators are employed to conduct quantitative comparisons. They are described in Section 3.3.2.

Table 3.1: Simulation campaign.

Op. point	$\dot{\mathbf{m}}_\mathbf{a}$	**% EGR**	**N**
A	↑	↓	↑
B	↓	↑	↓

Case	**Intake flap angle (°)**	**Op. point (-)**
45A	45	A
15A	15	A
0A	0	A
45B	45	B
15B	15	B
0B	0	B

3.3.2 Parameters analyzed

The consideration of the passive scalar for tracking the generated condensates allows the calculation of the liquid water mass flow rate that passes through a given section with little additional effort. Thus, performing this operation along different sections between the EGR discharge duct and the compressor inducer, it is possible to analyze and quantify the influence of the compressor on the mixing process and determine the impact of neglecting the compressor from the simulation. Additionally, an overview of the influence of using different operating conditions and flap angles will be possible through this analysis. Differences in condensation rate between the complete and the reduced cases will be displayed in absolute and relative values, which are calculated following Equations 3.1 and 3.2 respectively.

$$\epsilon_{abs} = cond_{comp} - cond_{red} \quad \left(\frac{g}{h}\right) \tag{3.1}$$

$$\epsilon_{rel} = \frac{cond_{comp} - cond_{red}}{cond_{comp}} * 100 \quad (\%) \tag{3.2}$$

Condensation depends on how the streams are mixed, which in turn is determined by the flow structures. The mechanisms that set the main flow structures will be then studied and discussed in Section 3.4.

Analogously, each flow pattern sets a different pressure distribution. Analyzing this parameter on the section at the end of the cone (boundary in the right side of Fig. 3.2) will provide useful information regarding the predominant mechanism that controls the flow structure at the inducer. The maximum and minimum pressures on that said sections will be analyzed as well.

3.4 Results

3.4.1 Axial evolution of condensation rate

The condensation rate from the EGR discharge duct to the end of the inlet cone for all the cases are shown in Figures 3.4 (op. point A) and 3.5 (op. point B). The vertical axis shows the condensation rate normalized with dry air mass

flow rate and the horizontal axis displays the axial position normalized with the distance between the EGR discharge duct and the end of the inlet cone (see Fig. 3.2). This is the critical region where the condensation is produced before reaching the compressor wheel. After entering the inducer, droplets may impact other components, deposit over the surfaces and even re-evaporate as the gas is compressed and heated up. However all this latter phenomena are not considered since the most harmful mechanism is the impact of the droplets against the leading edges of the compressor.

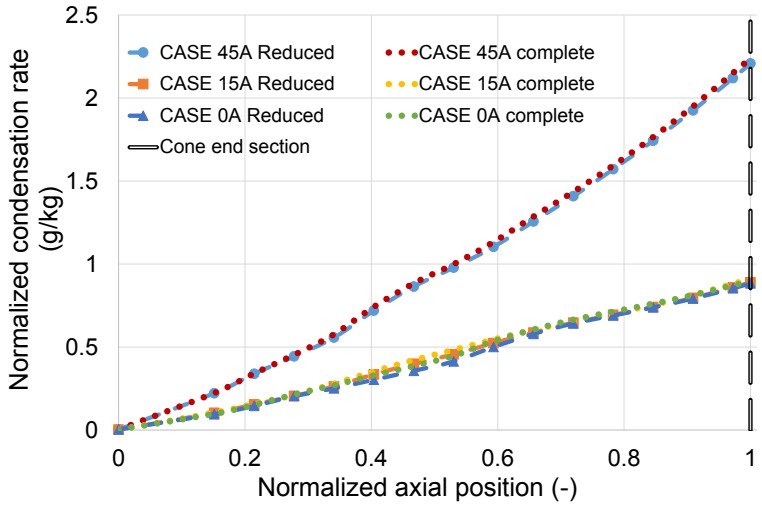

Figure 3.4: Condensation rate of operating point A cases.

3.4.2 Analysis of complete cases

In first place, the results of the complete case are analyzed. Dotted lines of Fig. 3.4 show the results of the cases with of operating point A. It is noticeable that in this case, where the EGR rate is low, small intake flap angles produce the same results of condensation, being the differences between 0° and 15° almost non-existent. Conversely, a high flap angle enhances condensation generation. Figure 3.5 shows the results of operating point B. In this case, the high EGR rate that characterizes these cases clearly controls the mixing and the condensation, producing similar results for all three cases. Nevertheless, the highest flap angle of 45° still produces at the end of the inlet cone the highest condensation rate.

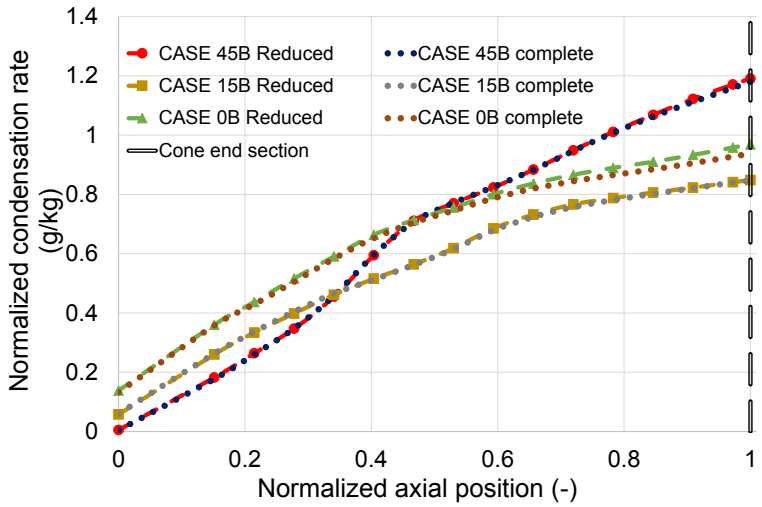

Figure 3.5: Condensation rate of operating point B cases.

The influence of the EGR rate and flap angle on the mixing process is illustrated in Figs. 3.6 and 3.7, where a Line Integral Convolution (LIC) [116] representation of the time-averaged temperature scalar over a longitudinal section, together with velocity vectors, are displayed. Figure 3.6 is devoted to the cases 15A and 45A, with lower EGR rate than their counterparts 15B and 45B, depicted in Fig. 3.7. In these figures it can be observed the EGR stream entering the T-joint from the bottom branch with higher temperature. As both streams mix, the temperature gradient at a given cross-section is reduced, which, considering the condensation rate results in Figs. 3.4 and 3.5, prove that the mixing of the streams and the condensation produced is correlated.

For the low EGR rate cases on Fig. 3.6, the high angle of the flap (bottom of the picture) induces high vorticity and turbulent structures which enhance condensation generation. Moreover, the low momentum region created by the valve reduces pressure, so that the EGR flow is directed upwards, further contributing to mixing of streams and condensation. Also, strong counter-rotating swirling structures are created by the flap and convected downstream, which extend the mixing region. On the contrary, when the flap angle is reduced (upper side of Fig. 3.6), the intake flow impinges and smoothly deflects the EGR stream towards the compressor, avoiding excessive mixing. For operating point A, Figure 3.4 suggests that there should be a threshold of low-end

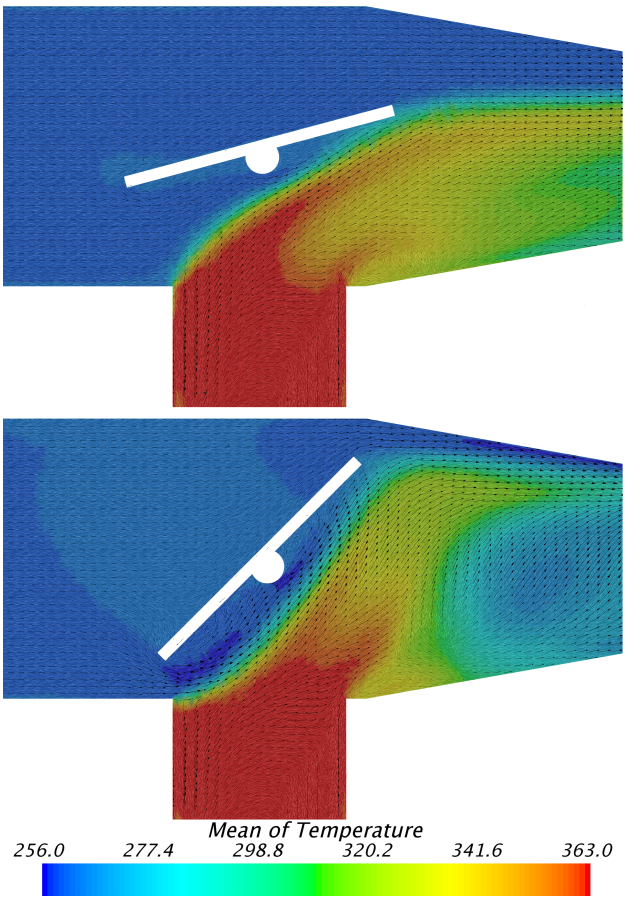

Figure 3.6: Line integral convolution of temperature and velocity vectors at longitudinal section for cases 15A (top) and 45A (bottom).

flap angle that does not affect the flow structure enough to have repercussions on the mixing.

High EGR rate cases corresponding to working point B, depicted in Fig. 3.7, show a lower influence of flap angle because the penetration of the EGR stream is higher, similarly impacting against the flap regardless of its angle. Part of the EGR stream may even surround the flap and overcome to the upper side towards the inlet face, advancing the condensation production, as can be seen in case 15B (top of Fig. 3.7). The condensation rate evolution of case 0B, depicted in the Fig. 3.5, shows an offset of condensation rate at the origin

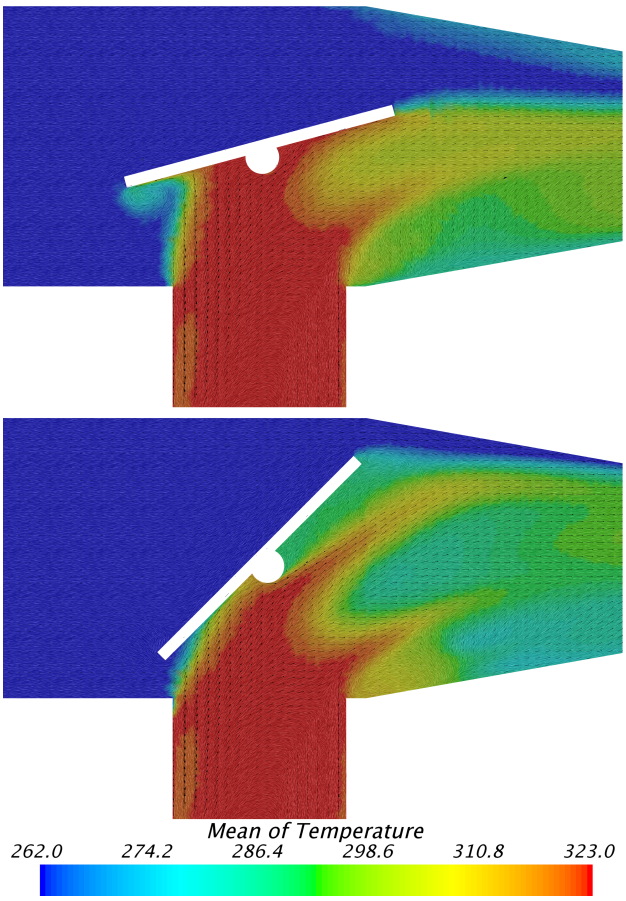

Figure 3.7: Line integral convolution of temperature and velocity vectors at longitudinal section for cases 15B (top) and 45B (bottom).

of the axial position, implying that condensates are being produced upstream the EGR duct, due to the aforementioned issue. This issue exists for operating conditions combining lower flap angles and high EGR rates.

3.4.3 Comparison of reduced and complete cases

The impact of the compressor on the mixing process and condensation generation can be assessed by comparing the results of condensation rate of the complete cases with their analogous with reduced geometries. Figures 3.4

and 3.5 show such results, in which dashed lines represent the reduced counterparts of the complete cases. Generally, the axial profiles of condensation rate predicted without compressor follow the ones corresponding to the complete cases with great agreement. Only a slight discrepancy is found in case 0B, but the reduced case prediction is still quite close to the solution of the complete geometry. The relative and absolute errors of condensation rate, calculated using Equations 3.1 and 3.2, are evaluated at the end of the inlet cone (normalized axial position = 1 in Figs. 3.4 and 3.5) and showed in Table 3.2.

Table 3.2: Condensation rate error in the cross-section at the end of the inlet cone.

Case	$\epsilon_{\mathbf{abs}}$ **(g/h)**	$\epsilon_{\mathbf{rel}}$ **(%)**
45A	-8.58	-1.37
15A	-5.37	-2.11
0A	-3.44	-1.37
45B	1.31	0.86
15B	0.15	0.14
0B	4.05	3.34

The relative errors found are all below 4%. Thus, the compressor does not significantly affect the generation of condensates. In spite of not playing an important role on the condensation production, it is worth analyzing why the influence is such small.

As can be seen in Figure 3.8, when comparing the water distribution at the end of the mixing region, it is noticed that strong patterns are unlikely to be perturbed by the compressor influence. In operating point A, where the intake mass flow is relatively high, strong and stable vortices are formed downstream of the flap, fixing this pattern from that point and explaining why both flow structures and condensation rate are almost identical.

On the contrary, Figure 3.9 shows the comparison of flow structure between the complete and reduced 45B cases. Operating point B has a lower intake mass flow rate that is combined with a higher EGR flow, what causes a weak and unsteady pattern that is likely permeable to external interactions such as the influence of the compressor. Note that velocity vectors in Fig.3.9 are much smaller than those displayed in Fig 3.8, and so are secondary flows (velocity vectors in Fig 3.8 and 3.9 use the same scaling factor). That is why the condensation patterns in Fig 3.9 are not the same for the complete

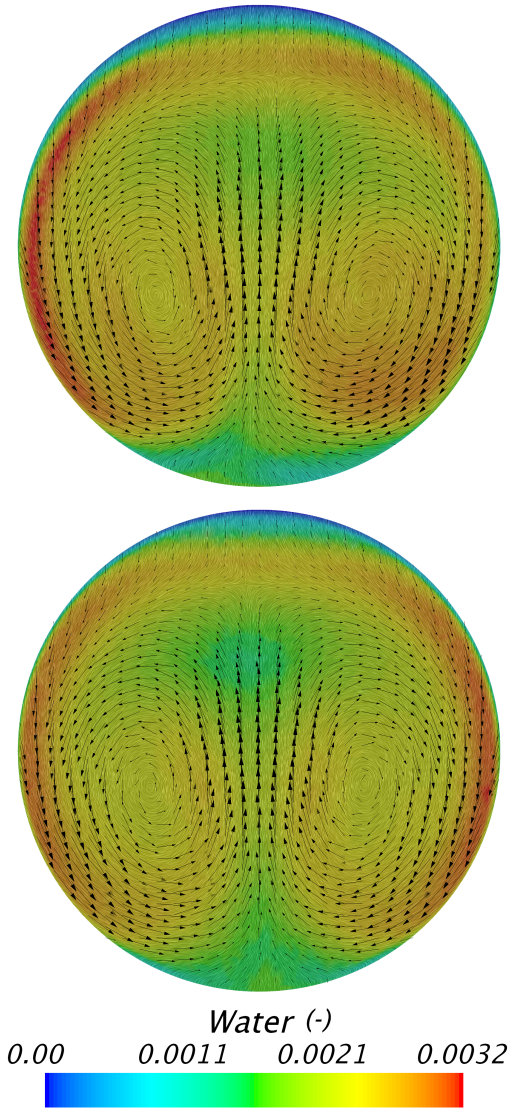

Figure 3.8: Cross-section time-averaged water fraction contours and in-plane velocity vectors comparison at the end of the inlet cone of case 45A. Complete case on top and reduced geometry on bottom.

and reduced case. However, due to the actual operating conditions of the compressor (low speed and compression ratio), its perturbation upstream the

wheel is also weak and the impact on secondary flows (and thus condensation) is only slight. There could be operating conditions where the impact could be greater, however these conditions are not in the common working range of the coupling between the turbocharger and the EGR demand [117].

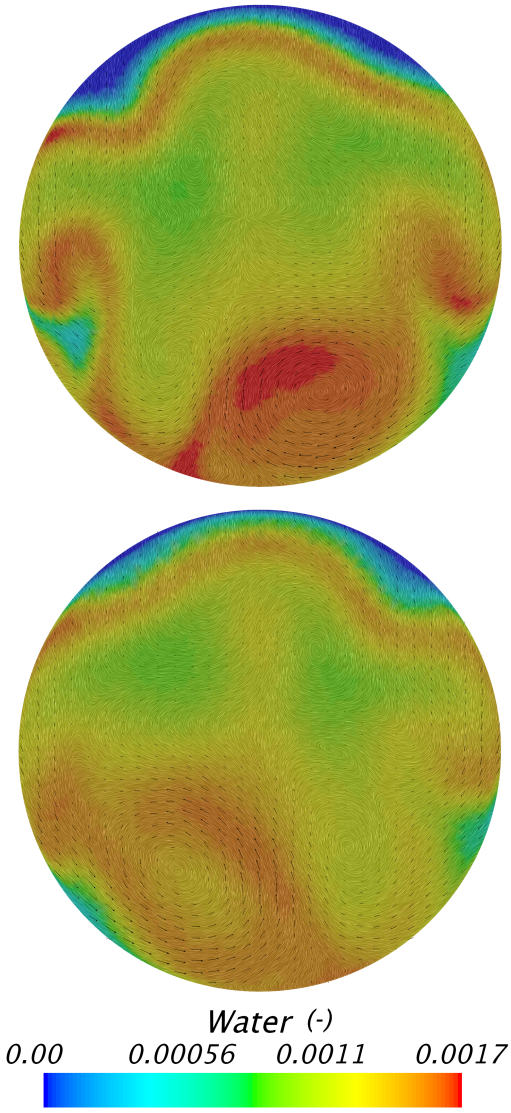

Figure 3.9: Cross-section scalar of water fraction comparison at the end of the inlet cone of case 45B. Complete case on top and reduced geometry on bottom.

An additional approach to detect predominant flow patterns resides in observing the pressure contours. Cases with strong flow structures generated during the mixing process usually have defined vortices with elevated pressure gradients. The pressure range of a given section plane is therefore defined as: $p_{range} = p_{max} - p_{min}$, where all pressures are time-averaged. In Table 3.3 the pressure range at the section at the end of the inlet cone are provided, for both complete and reduced cases.

Table 3.3: p_{range} at the end of the inlet cone section.

Case	Complete Case (Pa)	Simplified Case (Pa)
45A	5360	5710
15A	1812	1239
0A	2031	1221
45B	618	444
15B	351	279
0B	486	262

There are two phenomena mainly responsible for creating in-plane pressure gradients that would drive secondary flows. First, regarding the valve, higher flap angles and higher mass flow rates (and velocities) imply a higher pressure gradient. This occurs in case 45A, where the high mass flow and the high flap angle produce two strong counter-rotating vortices with low pressure in their centers, masking the rest of the pressure perturbations, as can be seen in the comparison of Figure 3.10. Second, concerning the impeller, the closeness of the nut of the wheel to this section drives the gas stream away from the center of the duct, lowering the velocity and increasing the pressure near the central part. This phenomenon increases with the mass flow rate and causes a higher pressure gradient compared with a simulation without the compressor and the nut.

In the rest of the cases, where the flow structures at the mixing region are not as dominating as in case 45A, the influence of the compressor is clearer. A lower pressure gradient can be observed in Figure 3.11, where the flap angle is set at 0°. The presence of the nut in the central part of the complete simulation causes the pressure to be noticeable higher, while in the reduced case the pressure distribution is homogeneous. This is a good example of the compressor influence, the pressure gradient generated by it is so relatively small that the secondary flows are weak and do not impact the condensation

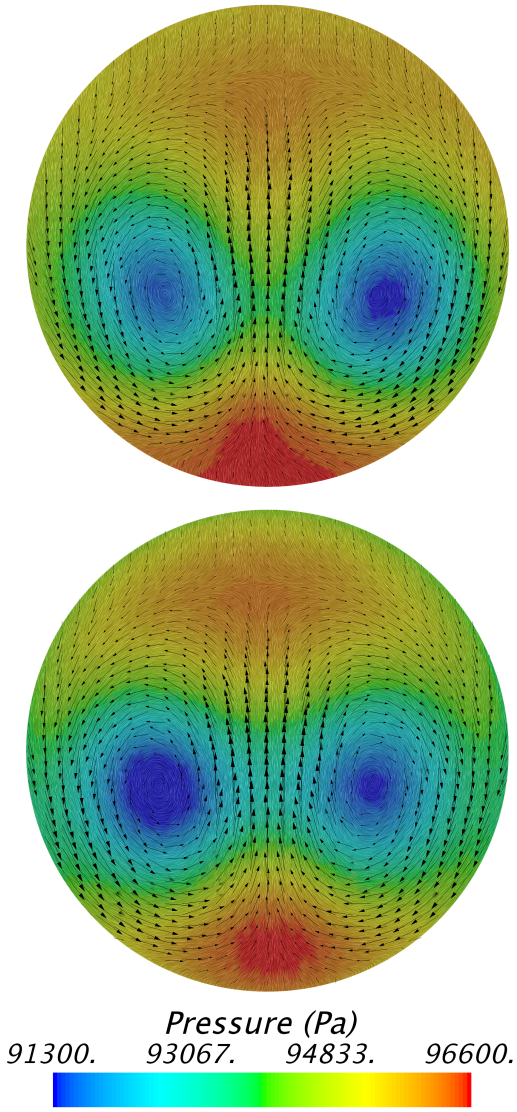

Figure 3.10: Cross-section scalar of pressure comparison at the end of the inlet cone of case 45A. Complete case on top and reduced geometry on bottom.

rate, as seen in Figs. 3.4 and 3.5.

Finally, to evaluate the extension of T-joint region affected by the compressor, the pressure contours between the solutions of the complete and reduced

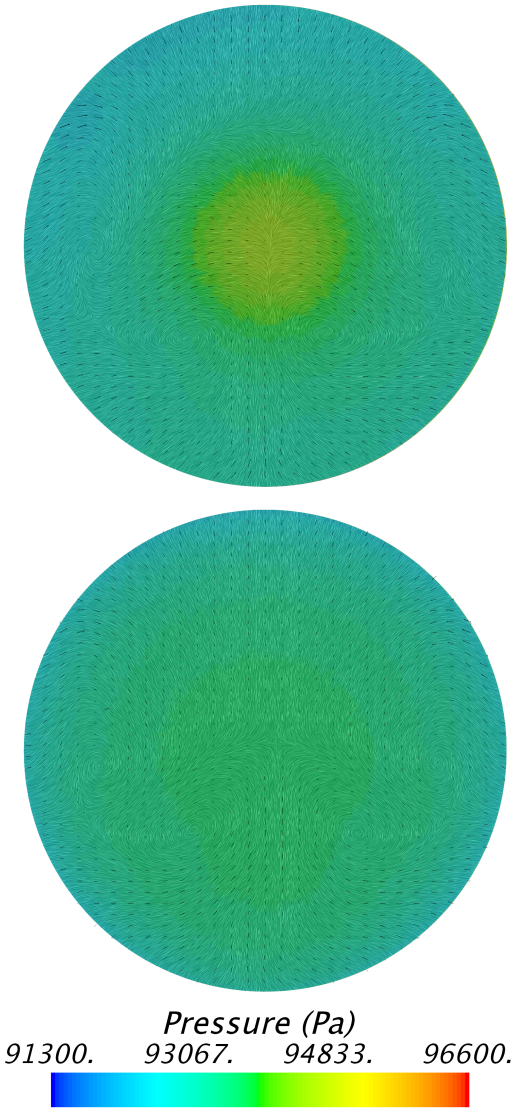

Figure 3.11: Cross-section scalar of pressure comparison at the end of the inlet cone of case 0A. Complete case on top and reduced geometry on bottom.

cases are compared in a longitudinal section of the T-joint. For this, in upper part of Fig. 3.12 pressure contours of the complete case as well as velocity vectors are shown. In the lower part of Fig. 3.12, the pressure difference be-

tween both cases is displayed as contours and the difference in velocity fields is displayed as vectors. Case 0B has been chosen as it presents the greater discrepancy of condensation rate near the end of the inlet cone (see Fig. 3.5). The pressure difference is performed as follows: First, the pressure data of that section of the reduced case is mapped and the generated data is imported by the complete case and interpolated in the same section, ready to be subtracted by its own pressure contour. Velocity vectors have been superimposed in both scenes, with a direct scaling factor (m/s $\rightarrow$ m) of 1/9000 in the pressure contours of the complete case and of 1/900 in the pressure difference. Again, the effect of the presence of the compressor is clearly noticeable due to the perturbation introduced by the impeller nut, which causes a higher pressure (lower velocity) near the central part, and a lower pressure (higher velocity) in the periphery. This effect is clearly limited to the vicinity of the outlet boundary, not even reaching the flap. There could be working points in which the influence of the compressor could reach far upstream, such as when backflows appear in stall conditions (see Chapter 5,[74]). However, in this region, the engine employs little EGR [117] to achieve high low-end torque. Additionally, perceptible pressure and velocity differences are found, although lower than the previous ones, along the inlet cone in the EGR discharge side in regions of low momentum that appear downstream the discharge of the EGR, similarly to the low pressure regions that appear downstream a backward facing step. This is probably the cause of the slight difference in condensation rate found in the comparison made from Figure 3.5. A slight shift of the EGR stream towards the inlet produce the velocity alterations found in that region.

It is worth remembering that the comparison discussed in this section is performed with same average outlet pressure. To quantify the sensitivity of imposing the outlet pressure boundary condition in the reduced simulations against the condensation rate solution, a parametric study has been set on cases 45A and 15A, adding four variations on each one in terms of outlet pressure. For each case, their reference value of outlet pressure has been modified in $\pm$3000 and $\pm$10000 Pa. Figure 3.13 shows the results of condensation rate relative to the cases with reference outlet pressure at the end of the inlet cone of both 45A and 15A cases and all the outlet pressure variations made.

In both cases, a near-linear behavior of the condensation against the outlet pressure variation is observed and according to the psychrometric physics [96]. The sensitivity is not high, since an increase of 3000 Pa implies a deviation error of around 3% in condensation rate for case 45A and lower for case 15A,

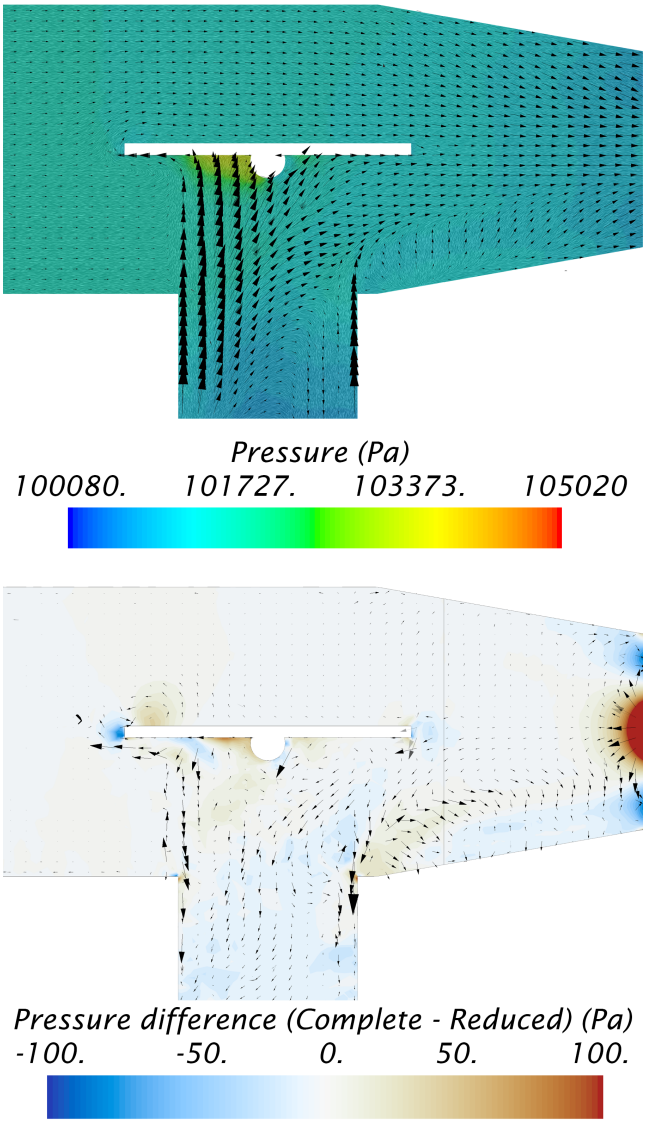

Figure 3.12: Pressure contours of complete case 0B and pressure difference with reduced case.

error at the same order of magnitude than the uncertainty accepted during the comparison between the complete and reduced cases made previously on this work. Moreover, this error is quite above the differences found in Figure 3.12,

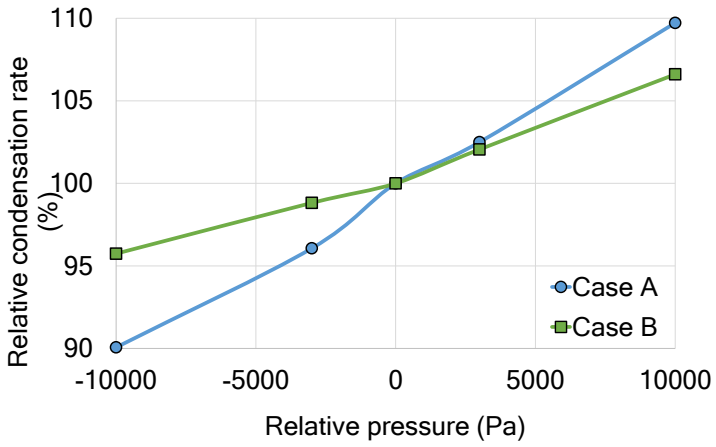

Figure 3.13: Parametric study of outlet pressure influence on condensation rate.

validating the usage of a reduced T-joint geometry for solving the condensation problem, avoiding higher computational efforts. It is worth noting that a tool for predicting the outlet T-joint pressure without the need of simulating the complete compressor should be in an accuracy range of around 1000 Pa, assuring a reduced error below 1%, which is affordable for a simple pressure losses T-joint model. As will be noted in Section 3.5, such a model is proposed as future work.

3.4.4 Computational effort

To assess the impact on computational effort of reducing the domain, the actual time each simulation took to calculate a single time step is summed up in Table 3.4, considering both complete and reduced cases and using ten cores for all the cases. For the complete cases, the time needed to turn the rotor region mesh after each time step is included as well.

A time step of a complete simulation takes about 20 times more than a time step of a simulation with only the T-joint geometry. Furthermore, for properly converging a compressor simulation, several wheel rotations must be carried out and due to the chosen time step, the final time each complete simulation needs to be converged is around two weeks, with a 10-core parallel computation. Conversely, a reduced case only takes six hours to be completely solved,

Table 3.4: Comparison of computational effort.

Geometry	**Reduced**	**Complete**
Elapsed time/time step (s)	21	447
Number of time steps (#)	1000	3000
Turnaround time (days)	0.24	15.5

even less if the solution can be solved using a steady state time discretization, as seen in Section 2.5.2.3.

3.5 Conclusions

After discussing the results and assessing the impact of decoupling the compressor from the simulation in terms of computational effort, the following conclusions are obtained.

- The condensation model presented in Chapter 2 has been used in this study. It has proved to be useful for understanding the processes that control the condensation formation due to the mixing of several gas streams at different psychrometric conditions, specifically when ICE exhaust gases mix with fresh air upstream of a compressor in a LR-EGR system.
- Condensation distribution at the compressor similarly depends on both the geometry of the LR-EGR T-joint and on the operating conditions. Particularly, the highly turbulent flow structures the intake flap creates when the angle is high is the phenomenon that greatly increases condensation.
- The comparison of the results provided by the simulations with and without the compressor has shown the compressor to have minimal influence on the condensation prediction. Only when the flow structure is not being altered by the flap or the EGR stream, and the compressor is working at low mass flow rates, where recirculations may appear, some relative error are noticeable, and even in these cases the errors are low. Conversely, if the flow structure is set by the intake flap with high turbu-

lence, condensation is controlled by it and no influence of the compressor is found.

- For summarizing, imposing a constant and homogeneous pressure as outlet boundary condition at the end of the T-joint, instead of simulating the complete geometry with the compressor, provides condensation rate predictions which are within 3% of those predicted by the complete case. By neglecting the influence of the compressor in the T-joint domain, the computational effort required is reduced by two orders of magnitude, allowing an extensive analysis of the condensation focused only on this part.

The influence of the inlet geometry and the compressor on the condensation formation has been assessed. However, as covered in next Chapter 4, the impact of the inlet configuration on the surge margin and other performance parameters will prove to be relevant, as well.

Chapter 3 Bibliography

[33] L. Vyskocil, J. Schmid, and J. Macek. "CFD simulation of air–steam flow with condensation." *Nuclear Engineering and Design* 279 (2014), pp. 147–157. DOI: 10.1016/j.nucengdes.2014.02.014 (cit. on pp. 8, 28, 31, 70).

[35] C. Moses and G. Stein. "On the growth of steam droplets formed in a Laval nozzle using both static pressure and light scattering measurements." *Journal of Fluids Engineering* 100(3) (1978), pp. 311–322. DOI: 10.1115/1.3448672 (cit. on pp. 8, 28, 70).

[74] A. Broatch, J. Galindo, R. Navarro, and J. García-Tíscar. "Numerical and experimental analysis of automotive turbocharger compressor aeroacoustics at different operating conditions." *International Journal of Heat and Fluid Flow* 61 (2016), pp. 245 –255. ISSN: 0142-727X. DOI: 10.1016/j.ijheatfluidflow.2016.04.003 (cit. on pp. 11, 28, 70, 86, 122, 136).

[77] R. Navarro. *Predicting Flow-Induced Acoustics at Near-Stall Conditions in an Automotive Turbocharger Compressor: A Numerical Approach*. Springer, 2018. ISBN: 978-3-319-72248-1. DOI: 10.1007/978-3-319-72248-1 (cit. on pp. 11, 71, 73, 122, 123).

[79] *STAR-CCM+*. Release version 11.06.010. CD-adapco. 2016. URL: http://www.cd-adapco.com (cit. on pp. 12, 70, 72, 120, 122).

[87] Y. Patel, T. Turunen-Saaresti, G. Patel, and A. Grönman. "Numerical investigation of turbulence modelling on condensing steam flows in turbine cascade." In: *ASME Turbo Expo 2014: Turbine Technical Conference and Exposition*. American Society of Mechanical Engineers. 2014, V01BT27A035–V01BT27A035 (cit. on pp. 29, 72).

[96] M. J. Moran, H. N. Shapiro, D. D. Boettner, and M. B. Bailey. *Fundamentals of engineering thermodynamics*. John Wiley & Sons, 2010 (cit. on pp. 32, 86).

[108] A. Kuczaj, E. Komen, and M. Loginov. "Large-Eddy Simulation study of turbulent mixing in a T-junction." *Nuclear Engineering and Design* 240(9) (2010). Experiments and CFD Code Applications to Nuclear Reactor Safety (XCFD4NRS), pp. 2116 –2122. ISSN: 0029-5493. DOI: 10.1016/j.nucengdes.2009.11.027 (cit. on p. 70).

[109] C. Walker, A. Manera, B. Niceno, M. Simiano, and H.-M. Prasser. "Steady-state RANS-simulations of the mixing in a T-junction." *Nuclear Engineering and Design* 240(9) (2010). Experiments and CFD Code Applications to Nuclear Reactor Safety (XCFD4NRS), pp. 2107 –2115. ISSN: 0029-5493. DOI: 10.1016/j.nucengdes.2010.05.056 (cit. on p. 70).

[110] B. Smith, J. Mahaffy, and K. Angele. "A CFD benchmarking exercise based on flow mixing in a T-junction." *Nuclear Engineering and Design* 264 (2013). SI:NURETH-14, pp. 80 –88. ISSN: 0029-5493. DOI: 10.1016/j.nucengdes.2013.02.030 (cit. on p. 70).

[111] Y. Yang, J. H. Walther, Y. Yan, and C. Wen. "CFD modeling of condensation process of water vapor in supersonic flows." *Applied Thermal Engineering* 115 (2017), pp. 1357 –1362. ISSN: 1359-4311. DOI: 10.1016/j.applthermaleng.2017.01.047 (cit. on p. 70).

[112] A. Torregrosa, A. Broatch, X. Margot, J. García-Tíscar, Y. Narvekar, and R. Cheung. "Local flow measurements in a turbocharger compressor inlet." *Experimental Thermal and Fluid Science* 88 (2017), pp. 542 –553. ISSN: 0894-1777. DOI: 10.1016/j.expthermflusci.2017.07.007 (cit. on p. 70).

[113] J. Andersen, F. Lindström, and F. Westin. "Surge definitions for radial compressors in automotive turbochargers." *SAE International Journal of Engines* 1(1) (2008), pp. 218–231. DOI: 10.4271/2008-01-0296 (cit. on p. 70).

[114] F. Mendonça, O. Baris, and G. Capon. "Simulation of Radial Compressor Aeroacoustics using CFD." In: *Proceedings of ASME Turbo Expo 2012*. GT2012-70028. ASME. 2012, pp. 1823–1832. DOI: 10.1115/GT2012-70028 (cit. on pp. 71, 120, 122).

[115] J. Galindo, A. Tiseira, P. Fajardo, and R. Navarro. "Analysis of the influence of different real flow effects on computational fluid dynamics boundary conditions based on the method of characteristics." *Mathematical and Computer Modelling* 57(7-8) (2013). Public Key Services and Infrastructures EUROPKI-2010-Mathematical Modelling in Engineering & Human Behaviour 2011, pp. 1957–1964. ISSN: 0895-7177. DOI: 10.1016/j.mcm.2012.01.016 (cit. on p. 73).

[116] B. Cabral and L. C. Leedom. "Imaging vector fields using line integral convolution." In: *Proceedings of the 20th annual conference on Computer graphics and interactive techniques*. ACM. 1993, pp. 263–270. DOI: 10.1145/166117.166151 (cit. on pp. 77, 130).

[117] Q. Zhang, M. Li, G. Li, S. Shao, and P. Li. "Transient emission characteristics of a heavy-duty natural gas engine at stoichiometric operation with EGR and TWC." *Energy* 132 (2017), pp. 225 –237. ISSN: 0360-5442. DOI: 10.1016/j.energy.2017.05.039 (cit. on pp. 82, 86, 147).

Chapter 4

Experimental assessment of inlet geometry influence on compressor performance

Contents

4.1 Introduction

Turbochargers (TC) are well known machines with a development of near a hundred years. However, the application of turbomachinery to reciprocating internal combustion engines (ICEs) is relatively new, experimenting a notable increase in the last fifteen years for diesel engines and even less for gasoline engines. Thus, there is still room for further studies of the couple TC-ICE. The study of this combination is particularly relevant due to the trend that most engines are following, the downsizing, which is the tendency of reducing the total cylinder displacement. Turbocharging is really interesting when using this approach, because it helps achieving higher specific power and efficiency (see Section 1.1).

Nevertheless, a turbocharged engine presents some drawbacks due to the coupling between two different machines. On one hand, the four stroke ICE is a reciprocating machine that performs its thermodynamic cycle in four piston strokes, generating acoustic pulses that propagate through the pipes arriving and interacting with the compressor and the turbine. Its rotational velocity varies from about 800 to 5000 rpm in common situations. On the other hand, the turbocharger is a continuous flow machine which axis rotates at very high revolutions per minute (50k to 200k depending on the size). In addition, the TC responds to mass flow rate variations with a reduced rate of change of shaft speed due to the TC rotational inertia, among other factors. The mismatch between the dynamics of the engine and the turbocharger introduces what is called turbo-lag, which consists of a delay of the turbocharger response to engine demands.

Compressor working range is limited by choke conditions at very high mass flow rates. Wheel structural integrity also constrains maximum rotating speed. At low mass flow rates the compressor flow is not capable of overcoming the adverse pressure gradient due to its reduced velocity, and reversed flow appears. This produces a drop in compression ratio until the flow goes in the right direction, the pressure ratio increases and the cycle starts again. This is clearly an oscillating phenomenon, which introduces undesirable acoustics pulsations to the pipes. Moreover, axial loads appear, forcing the wheel against the walls and potentially causing mechanical damage [118]. This phenomenon is the so-called surge, which is described as a pulsating and transversally uniform phenomenon that affects mainly the compressor inlet [45].

The research on compressor surge is addressed from different points of views. Some researches [46, 47, 48] describe the possibility of finding different types of surge depending on the pulsation frequency and its amplitude. Other consider the attenuation or delay of appearance of the phenomenon thanks to control systems placed either upstream or downstream the compressor [49, 119, 120]. Some authors obtain a clear shift of the surge margin [121, 54]. The margin can be improved or worsened depending on the element placed at the compressor inlet or outlet [57, 50, 122].

Car manufacturers may have packaging constraints that result in different compressor intake geometries which have an impact on compressor performance that is not known beforehand [55, 56]. The effect of particular compressor intake geometries (elbow, tapered duct, reservoir, etc.) has been previously covered by several researchers [123, 28, 58] and the effect of actual configurations such as a LR-EGR T-joint has been assessed in Chapter 3. However, they do not usually include the effect of the inlet pipe on compressor acoustic behavior. Turbocharger airborne noise is becoming a major issue for automotive industry because downsizing moves the compressor working zone closer to near-surge conditions [10, 73], at which whoosh noise appears [75]. 3D-CFD simulations provide satisfactory predictions of compressor acoustic signature [65], but the computational effort is so high that only a few operating conditions can be calculated.

Karim et al. [71] performed Large Eddy Simulations with 5 different inlet configurations (using swirl vanes, short and large steps and combinations of these elements) at two different operating conditions. The Sound Pressure Level (SPL) integrated over 6-12 kHz obtained at the compressor inlet is compared for the different inlet configurations. The combination of a large step with swirl vanes provides less SPL for both operating conditions. Experimental measurements with short and large step are performed in a powertrain dynamometer semi-anechoic cell. The SPL integrated between 4 and 12.7 kHz using radiated noise measurements shows the superior performance of the large step over the small step.

Compressors are generally tested in a test bench specially designed to obtain the centrifugal compressor map. Those tests are done in special conditions, such as large pipes and continuous flow [62]. But when the turbocharger is installed in the engine, the conditions are very different, with pulsating flow and short pipes, which affects the surge margin [124, 64].

Previous works show that inlet geometry has a major impact on surge, but the effect on other compressor parameters is not often considered. Moreover, not all relevant geometries have been covered and those which have been analyzed are often tested with steady working points that do not resemble their actual operating conditions. In this work, an automotive turbocharger is tested on its real engine so as to assess the actual effect of different inlet geometries on compressor performance, surge margin and noise emission.

The main disadvantage of the selected approach is the inability to perform detailed measurements at the compressor inlet. This information could be used to explain the flow behavior with the different intake configurations and thus the physical phenomena responsible for the modification of compressor performance when varying the inlet pipe. Raitor and Neise [72] were able to instrument a 224-mm-diameter compressor working at a steady rig with pressure transducers, but the procedure is more than challenging for the considered passenger car turbocharger compressor installed on an engine test bench, due to spatial constraints. Another possibility could be to perform Particle Image Velocimetry (PIV) measurements at the compressor entry, such as the campaign conducted by Guillou et al. [125]. The different shapes of the intake geometries and the reduced dimensions of the turbocharger again restrict this approach; for instance, Guillou et al. mounted a bell mouth at the compressor inlet.

Considering the aforementioned constraints for assessing the influence of the inlet geometry on the compressor performance, this chapter addresses the analysis of the impact of four inlet geometries using an experimental approach, performing both steady and transient tests to simulate realistic engine conditions. Conversely, a numerical assessment with similar inlet configurations will be performed in Chapter 5.

The outline of this chapter goes as follows: Section 4.2 describes the experimental apparatus, the tests performed and the different inlet configurations. The results of both steady and transient tests are shown in Section 4.3 and finally, the conclusions are presented in Section 4.4.

4.2 Materials and methods

4.2.1 Experimental facility

Tests were performed using a commercial engine in a test bench, allowing the compressor to achieve high loads and speeds. In addition, the compressor map that can be obtained with this set up may have some variations due to the particular matching with the engine, yielding a more realistic result. Engine main characteristics are listed below.

- Displacement: 2L.
- Number of cylinders: 4.
- Fuel type: Diesel.
- Maximum power: 120 kW (163 hp) @ 3600 rpm.
- Maximum torque: 340 Nm @ 2000 rpm.
- Injection: common rail direct injection.
- Valve system: DOHC, 16 valves.
- Turbocharger with Variable Geometry Turbine (VGT).

Figure 4.1 depicts a schematic of the test bench, including all the sensors with which the rig was instrumented. A dynamo-metric brake was used, which controlled the engine speed and its torque. Almost all variables were registered at a frequency of 100 Hz. Mass flow rate and compressor inlet pressure were recorded at a frequency of 1 kHz instead, since they were used to detect surge appearance (see Section 4.2.2). Additionally, a directional intensity probe was installed facing the inlet mouth, surrounded by acoustic insulation mats in order to avoid reflections from the walls or other components [76]. This probe measures the sound intensity level (SIL) up to 5 kHz in order to characterize the compressor intake orifice noise.

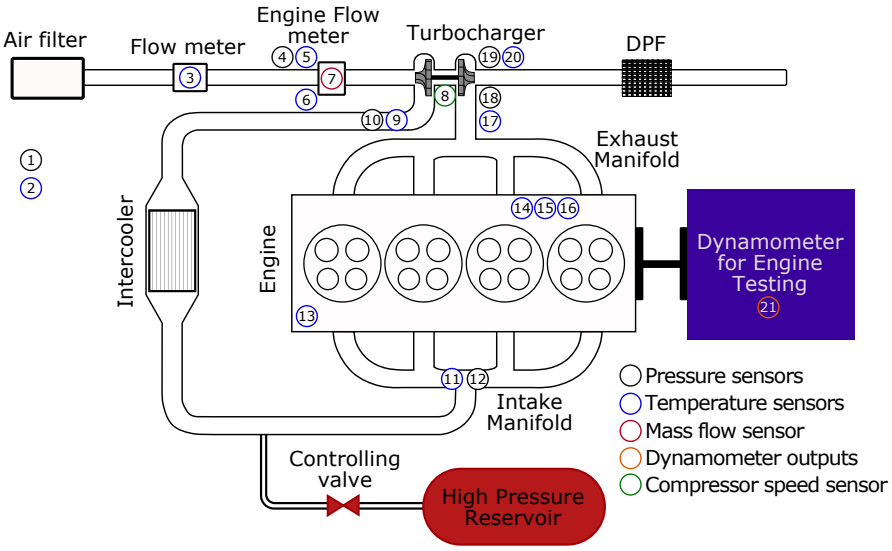

Figure 4.1: Test bench scheme.

4.2.2 Steady tests

Different tests were performed with each inlet configuration in order to obtain the compressor behavior in both steady and transient operating conditions. First, steady tests include the characterization of the surge line, what is done injecting compressed air in the inlet manifold [59, 61]. An air compressor from the workshop provides the test cell with high pressure air, which is connected to the inlet manifold through a controlled pneumatic valve. With this method, the injected air enters in the cylinders and consequently, less air passes through the compressor, which is controlled indirectly by the VGT position, forcing it to keep the pressure ratio constant. It is possible to perform this action thanks to the open ECU available in the engine. In this way the compressor operating point moves towards the surge limit until suddenly it becomes unstable and enters in deep surge. At this moment, the air injection is stopped so that the compressor does not suffer any damage. The last stable point, obtained by a frequency analysis over the instantaneous pressure recording [64], determines the surge limit and, if this process is repeated for different compression ratios, the surge line can be determined by joining these points.

The second steady-state test consists in obtaining part of the compressor map itself; from the surge line to medium mass flow rates. It is not objective

of this study to obtain the complete compressor map. The process followed in this case is very similar to the surge line method. Firstly, a compression ratio is imposed by controlling the VGT; the air injector valve is closed at the beginning and gets open progressively. For a certain valve position, the engine will eventually reach a steady-state working point, and then the acquisition systems get data from the sensors during five seconds in order to get a mean value. Afterwards, the compression ratio is changed and the process is repeated.

For every measured working point, two important parameters are calculated. One of them is the SIL, which is obtained from the intensity probe described in Section 4.2.1 and then, Eq. 4.1 is used, selecting a frequency window from 500 to 5000 Hz, which coincides with the most sensitive human audio range.

$$SIL = 10 \ \log_{10} \left(\frac{\sum_{f=500Hz}^{5000Hz} I(f)}{10^{-12}} \right) \quad (dB) \tag{4.1}$$

The other one is the compressor isentropic efficiency, which is defined by:

$$\eta_s = \frac{\dot{W}_s}{\dot{W}} = \frac{T_{in,t} \left(c_{p,in} \ \Pi_{t,t}^{\frac{\gamma-1}{\gamma}} - c_{p,in} \right)}{c_{p,out} \ T_{out,t} - c_{p,in} \ T_{in,t}}, \tag{4.2}$$

where γ is the ratio of specific heats.

The last steady test is the obtaining of the 160 krpm turbocharger isospeed line, which is used to have an estimation of the pressure drop of each inlet configuration at high air mass flow rates. Turbocharger speed is kept constant actuating over the VGT position.

4.2.3 Transient tests

In Section 4.1 the lag problem of the turbocharger was introduced. This issue may lead the TC into surge, as graphically explained by Fig. 4.2, where two processes are depicted. In the left one, an engine acceleration from point

1 to point 2 is plotted. If the evolution was quasi-steady, the path would be a straight line between these two points. Due to the turbo lag, there is an increase of the mass flow followed by an increase of the compression ratio, though. On the right hand side of Fig. 4.2, an engine deceleration from point 1 to point 2 is depicted. In this case, the compressor operation deviates from the straight path reducing the mass flow in first place and then reducing compressor pressure ratio. Stability problems may appear under this condition, since a sudden reduction of the mass flow when the starting point presents low mass flow rates can drive the compressor beyond the surge line.

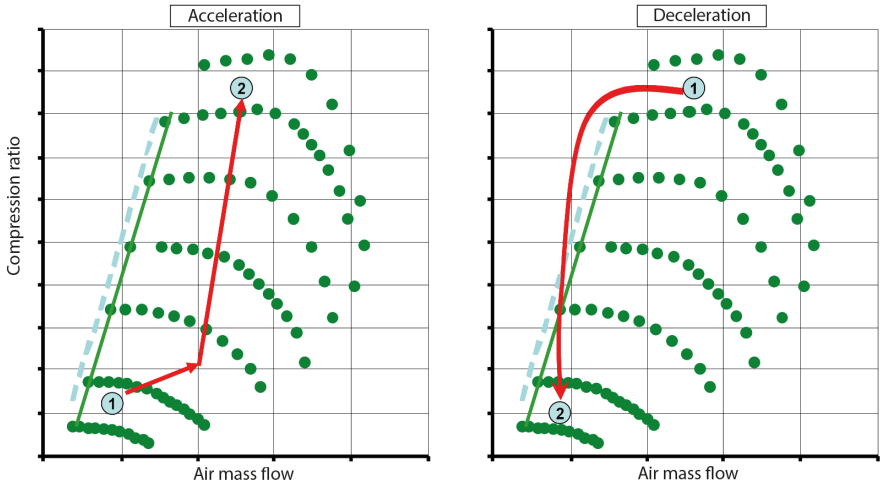

Figure 4.2: Acceleration and deceleration transient evolutions over a compressor map.

Transient tests aim to reproduce the aforementioned problem by performing sudden pedal releases at different boosting pressure, engine speed and engine decelerating rate. These tip-out experiments are of importance because they reproduce the onset of surge in real driving conditions. However, they are scarcely used in the literature, save for papers dealing with the design of surge control systems [126, 127].

In this work, boosting pressures tested varied from 1.2 to 2.4 bar, engine regimes covered a range from 1250 to 2250 rpm and deceleration rates were imposed to go from 200 to 1200 rpm/s. Due to the compressor map topology, not every combination of boosting pressure and engine speed could be achieved, neither some points were able to reach surge conditions because of

being too far from this zone. Each test was repeated three times in order to obtain averaged values. Data acquisition in these tests was performed by the high frequency acquisition system, which is able to register variables at 1 kHz, enough to get surge oscillations. Only engine speed, pedal position, mass flow, compressor outlet pressure and turbocharger speed sensors were connected to this system due to the high size of the generated files.

An example of a tip-out test is depicted in Fig. 4.3. When a sudden pedal release is produced, the compressor behavior becomes unstable, entering in and out of surge until the compression ratio is low enough to recover the stability (see Fig. 4.4). Thus, the number of oscillations is a good indicator of the surge severity. In order to count the number of surge cycles, the compressor outlet pressure is derived and the local maximums are counted with the aid of a computational tool (Fig. 4.5). The final number of cycles is the average value between the three repetitions of the same experiment. The maximum rate of pressure change (bar/s) during the surge cycles was also used to evaluate the harm caused by this phenomenon, since this parameter is related with the intensity of the axial strokes that the turbocharger bearing should deal with. Finally, the characteristic frequency of the surge cycles is calculated with a Fourier analysis.

4.2.4 Compressor housing preparation

Since different inlet geometries are tested with the same compressor, the latter needs to be modified in order to allocate all the configurations. This modification consists in drilling the inlet until 3 mm of the inducer are left uncovered. Also two aluminum blocks are welded on both sides of the volute to be used as brackets. Figure 4.6 depicts the final state of the compressor housing. The left hand side of the figure displays the modified volute with the inducer housing removed and the support aluminum blocks. On the right hand side of the figure it is shown the piece whose function is to join the compressor with the different configurations. In this piece an orifice is drilled where the compressor speed sensor is placed. A groove in its edge hosts an O-ring which seals the junction between both pieces.

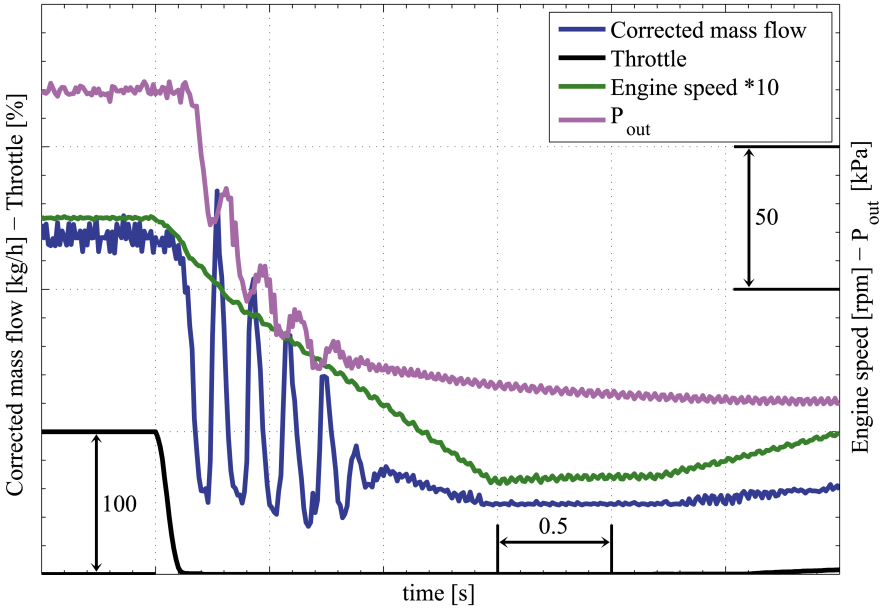

Figure 4.3: Sudden pedal release variable evolution.

4.2.5 Inlet configuration

In section 4.1 several intake geometries that may be considered (elbow, tapered duct, reservoir, etc.) were appointed. To decide which of them are more interesting to be investigated, a Pugh matrix was done in the following manner. In first place, important features of each mechanism are considered, such as complexity, scalability, noise emission or global performance. Then, each feature of each configuration is preliminarily evaluated and given a score from 0 to 5. Finally, scores are counted, high scores meaning interesting configurations. This step ended with the tapered duct and the nozzle as the chosen geometries. An additional geometry is considered as a baseline to assess the impact of each configuration. It consists in a straight pipe, just enlarging the compressor inlet with constant diameter long enough to assure developed flow at the inlet (>10 Diameters). This baseline geometry is depicted in Fig. 4.7(a), where the inducer plane is also schematically represented. For future comparisons it will be treated as configuration a).

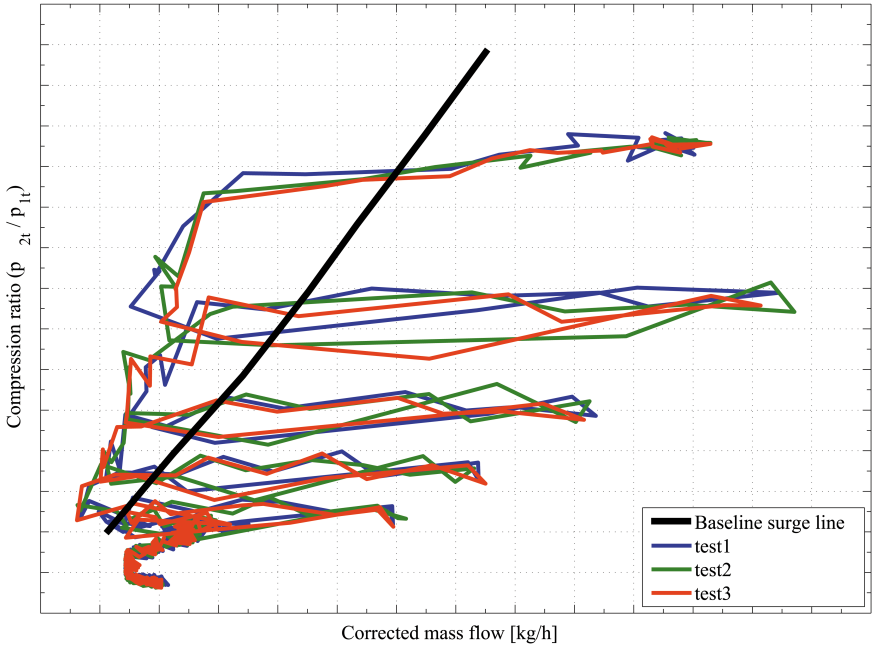

Figure 4.4: Transient evolution of a sudden pedal release over the compressor map.

4.2.5.1 Tapered duct

A tapered duct consists in a progressive narrowing towards the compressor wheel. This narrowing can be more or less pronounced, the slope can be constant (straight) or variable (curved) and the joints can be angled or smooth. In this case, due to constructive restrictions, the tapered part is straight and the joints are quite angled. A 90° semi-angle would represent the sudden expansion of a reservoir, device which provides a significant surge margin improvement according to Lang [58]. However, a reduction in the angle should decrease the pressure drop introduced by the device. The schematic of this design can be noticed in Fig. 4.7(b), from now on, configuration b).

4.2.5.2 Nozzle

The other device chosen is the nozzle. Desantes et al. [60] obtained the compressor map of a turbocharger with a nozzle in its inlet. The nozzle was

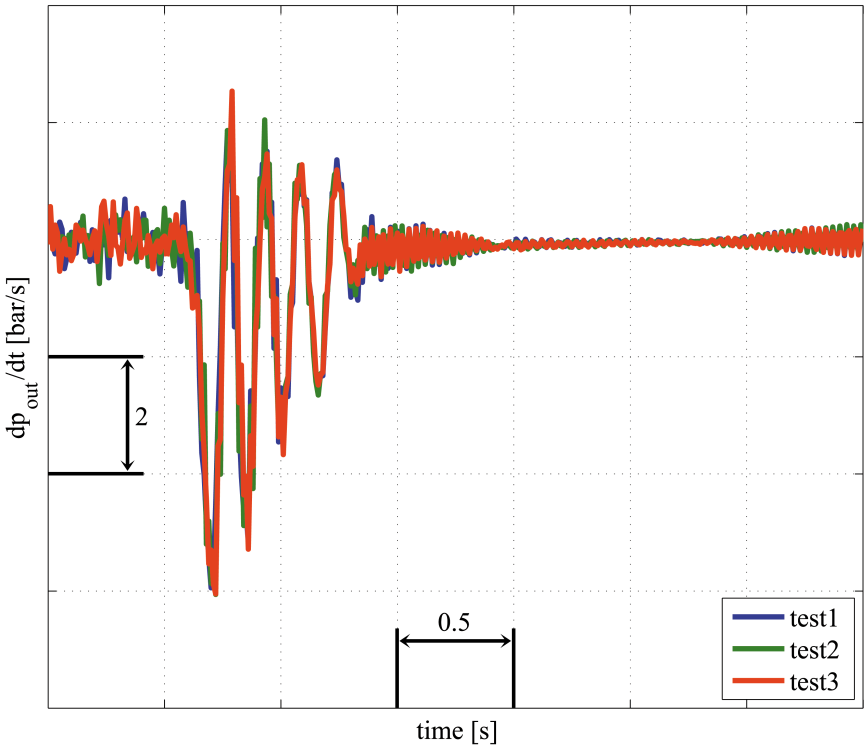

Figure 4.5: Derivative of the boosting pressure of a sudden pedal.

designed with a Convergent-Divergent (C-D) shape optimized to minimize the pressure loss. The resulting compressor map had its surge line significantly shifted to the left and the efficiency was globally increased. The obvious drawback of this element is the limited maximum flow rate and important pressure losses when the operating point is near this limit. These losses are due to the near transonic conditions through the throat. The final design of the nozzle used is depicted in Fig. 4.7(c) (configuration c)).

4.2.5.3 Final configurations

Once the basic designs have been decided, the particular configurations that were actually mounted and tested were selected with the following considerations.

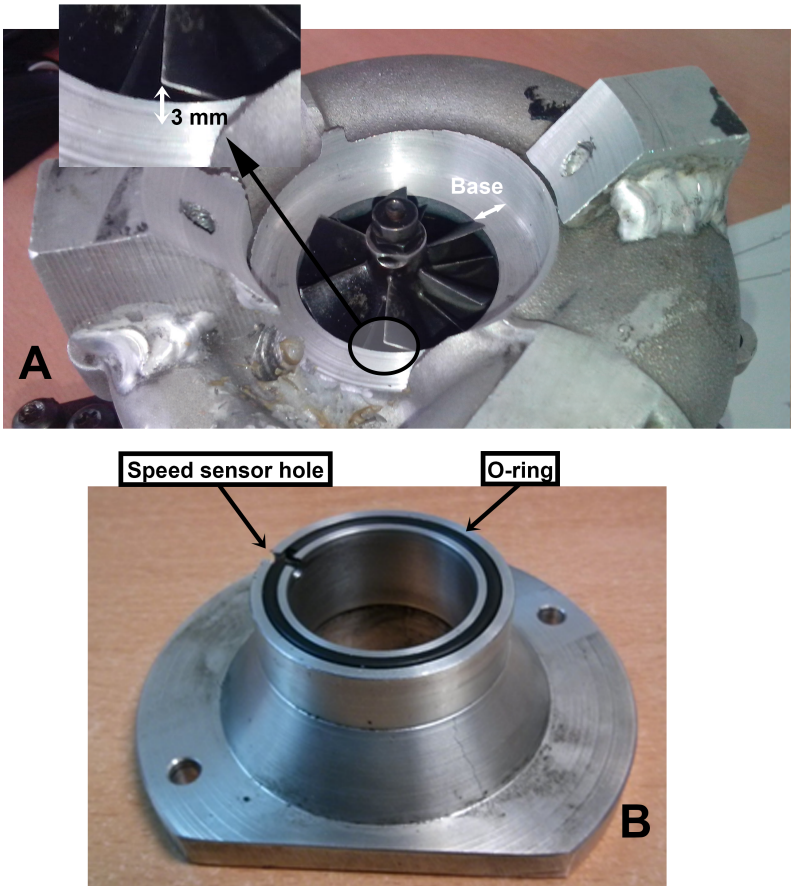

Figure 4.6: A) Modified compressor housing, B) Coupling piece.

- The baseline case (straight duct) required no additional information. Steady and transient test were performed with this configuration as a reference for subsequent comparisons.
- Several distances of wheel-to-tapered duct were tested to obtain the surge line, and a complete test was therefore performed with the configuration with the best performance.
- For the nozzle, another study of the surge margin sensitivity to the device position was performed, investigating now the distance from the wheel to the nozzle throat. Separators of different length were mounted between the device and the compressor and tested. Again, the particular distance

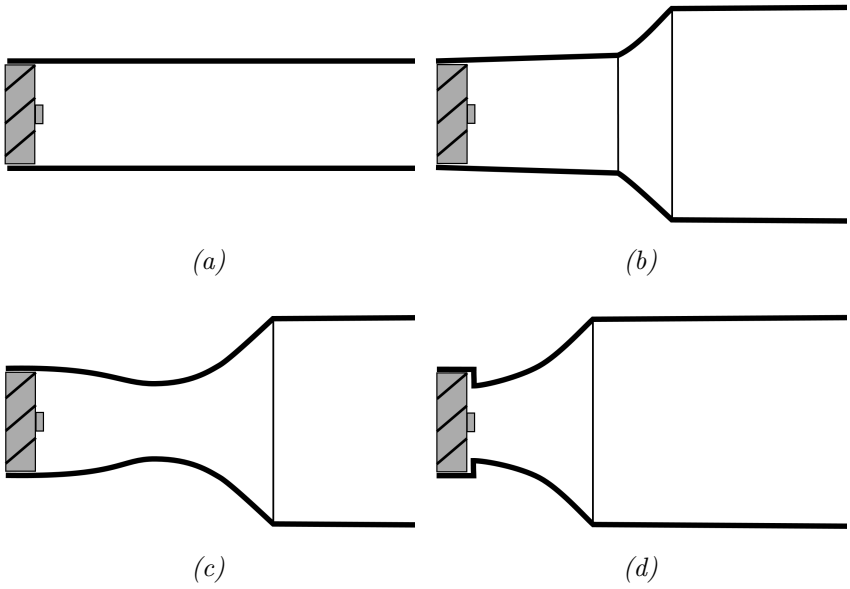

Figure 4.7: Configuration schemes

that provided the best results was selected for the full experimental campaign.

- Additionally, the divergent part of the nozzle was removed, allowing the throat to discharge directly against the compressor wheel (see Fig. 4.7(d)). A complete test with this last configuration was also conducted (configuration d)).

4.3 Results

4.3.1 Steady results

4.3.1.1 Surge and 160 krpm lines

Steady tests were performed as described in Section 4.2.2, obtaining surge and 160 krpm lines for the configurations selected in Section 4.2.5.3. Figure 4.8 depicts the corrected mass flow of the surge line (expressed relatively to the

baseline configuration) at three different compression ratios.

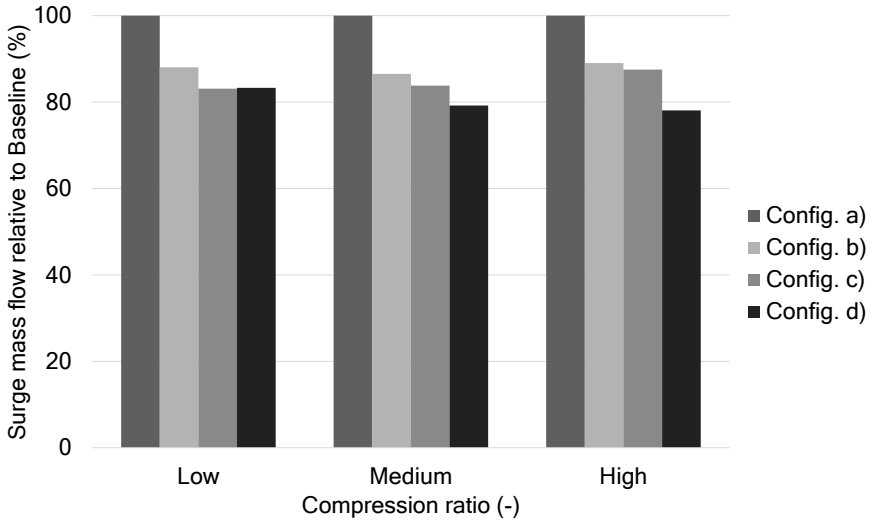

Figure 4.8: Surge improvement at different compression ratios.

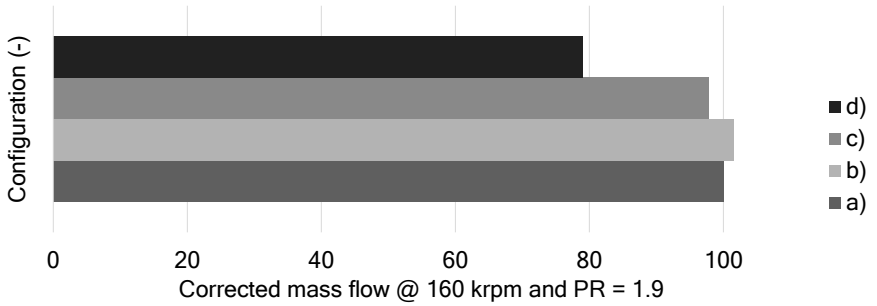

Figure 4.9: Corrected mass flow at $\Pi_c = 1.9$ for 160 krpm lines.

Surge lines are significantly shifted to lower mass flow rates for all the configurations. The tapered duct and the C-D nozzle achieve a similar gain, which is kept through all the compressor pressure ratio range. However, the convergent nozzle increases the surge margin for higher pressure ratios even more. In Fig. 4.9 it is shown another histogram about the relative corrected mass flow at 160 krpm and at the same compression ratio near choke conditions. This figure illustrates the important drawback of the convergent nozzle, which is its bad performance at high mass flow rates. This is due to the change in

the relative position of the throat to the inducer. With the throat discharging directly to the wheel, the periphery of the inducer plane gets blocked, reducing the flow effective cross-section at the inducer plane. A similar effect would be obtained by reducing the compressor trim, what would decrease the maximum mass flow rate. On the contrary, the C-D nozzle provides a similar pressure drop compared with the straight duct because the inducer plane remains unblocked. Finally, the tapered duct slightly improves pressure ratio due to the inlet duct cross-section increase.

4.3.1.2 Compressor efficiency

Using a computer tool, it is possible to interpolate the results of the points obtained during the steady test and plot isentropic efficiency (see Eq. 4.2.2) contours over a compressor map. Figure 4.10 depicts such map for the studied configurations. Green represents higher efficiencies and red lowers. The axes have been normalized using the following equations:

$$\hat{\dot{m}}^* = \frac{\dot{m}^*}{\dot{m}_d^*} \tag{4.3}$$

$$\hat{\Pi}_c = \frac{\Pi_c - 1}{\Pi_{c,d} - 1}, \tag{4.4}$$

where $\dot{m}_d^*$ and $\Pi_{c,d}$ correspond to a design operating point of the compressor with the baseline configuration.

The augmented surge margin of the tapered duct entails an increase of isentropic efficiency in the surge side of the compressor map for this configuration. The C-D nozzle seems to shift best efficiency point (BEP) towards a lower mass flow and compressor speed, with an efficiency enhancement near the surge line, particularly at low compressor speeds. The BEP shift to a reduced mass flow rate and compressor speed is clear for the case of the convergent nozzle. Although the efficiency near surge is improved compared to the baseline case, maximum efficiency is decreased and the rest of the compressor map (higher mass flows) presents an efficiency loss.

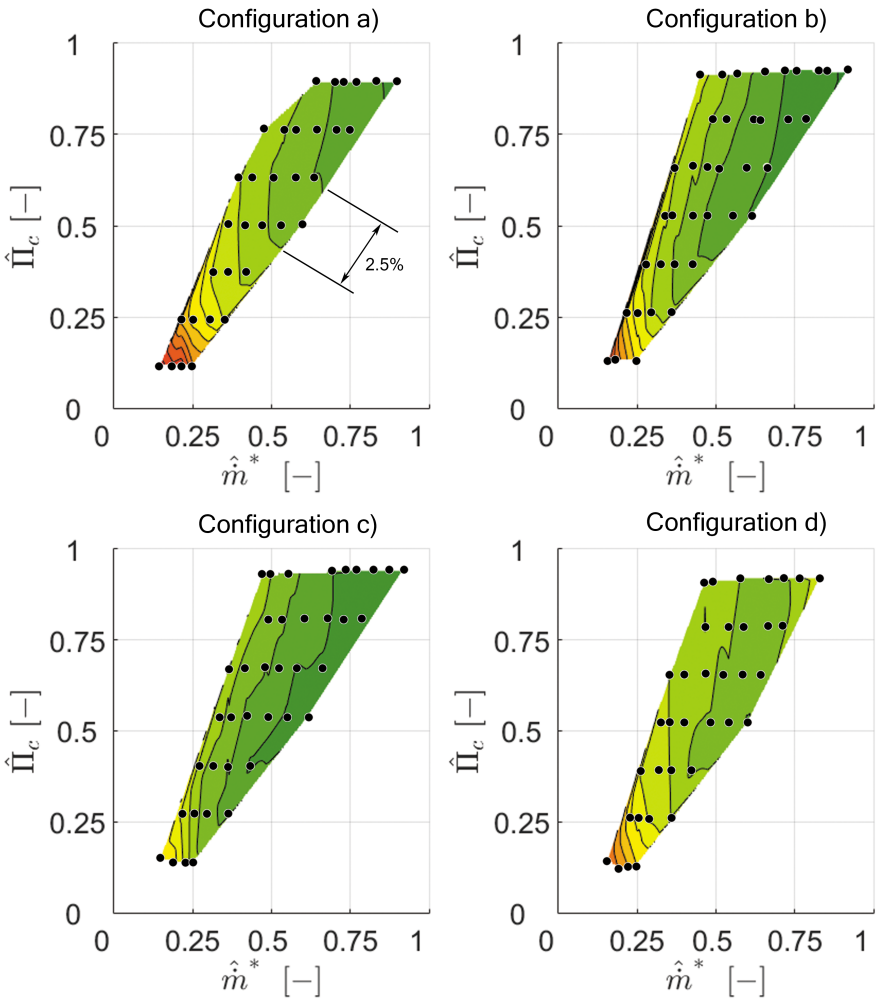

Figure 4.10: Compressor efficiency maps (warmer colors mean less efficiency).

4.3.1.3 Noise emission

Figure 4.11 uses the same approach of Section 4.3.1.2 to plot the SIL map for the different configurations. SIL was calculated from 20 to 5000 Hz with the intensity probe described in Section 4.2.1. In this case, green colors mean softer noise and red represent louder noise. The axes have been normalized using equations (4.3) and (4.4).

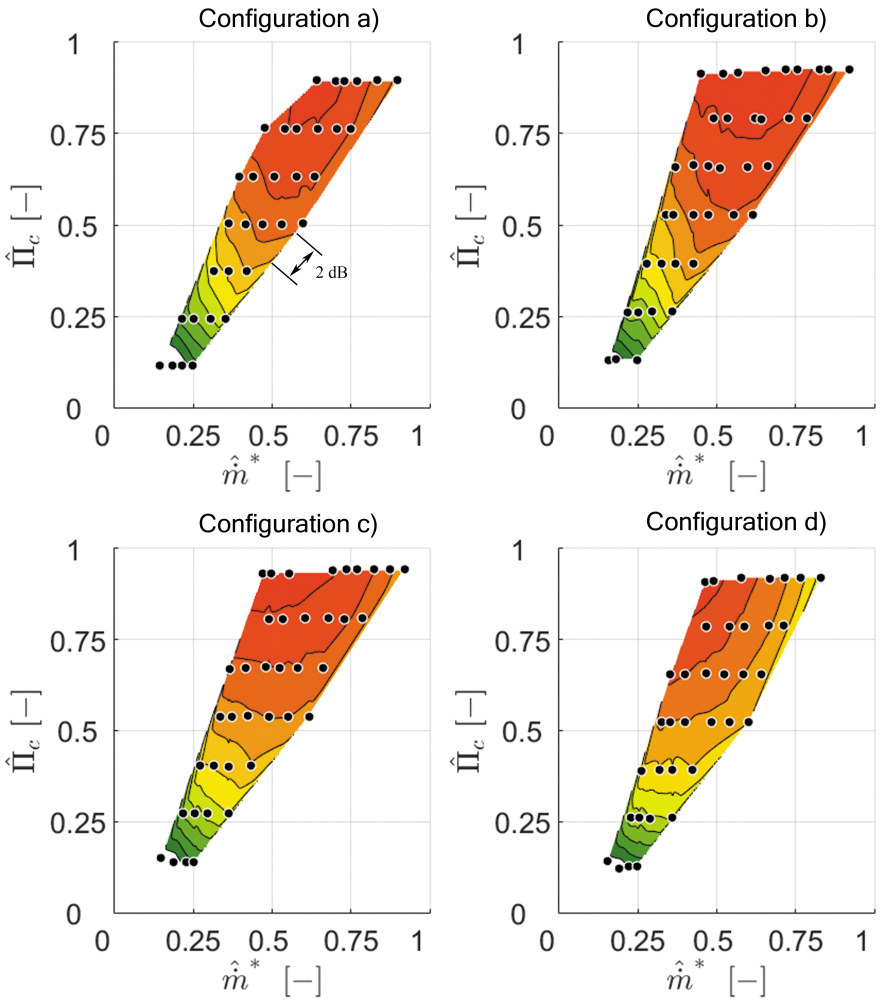

Figure 4.11: Compressor SIL maps (warmer colors mean higher SIL).

Observing the figure, the tapered duct is slightly noisier than the C-D nozzle. This is due to the higher diameter of the tapered intake duct. As aforementioned, the reduction of the flow effective cross-section at the inducer plane caused by the convergent nozzle also reduces the area of the noise emission, lowering the measured intensity notably.

4.3.2 Transient results

The complete amount of data obtained during the transient tests described in Section 4.2.3 is quite extensive, so Table 4.1 presents a summary of these results. First column shows the percentage of the tip-out tests at which surge occurred for each configuration. The average number of surge cycles per test (only considering those tests at which surge appears), their frequency and the maximum rate of pressure change (see Section 4.2.3) are also included in Table 4.1.

All the modified inlet geometries reduce the amount of tests at which surge appears. The effectiveness of a device in reducing surge occurrence is correlated with its surge margin improvement (see Fig. 4.8). However, the surge line of the C-D nozzle is only slightly better than the one obtained by the tapered duct, since surge occurs 10% times more for the tapered duct than for the C-D nozzle.

Even though the tapered duct only reduces by 5% the number of tests at which surge happens compared to the baseline case, the average number of surge cycles at these experiments is 30% less than with the straight duct, being (by far) the most effective intake geometry in this particular aspect. The tapered duct also reduces the surge frequency by almost 20% regarding the reference case. In terms of decreasing the maximum rate of pressure change, the best geometries are the nozzles, with a reduction of about 20% compared to the case with a straight duct.

Config.	**Surge occurrence**	**Surge cycles**	**Surge frequency**	**Rate of pres. change**
	(%)	**(#)**	**(Hz)**	**(-bar/s)**
a)	43	4.8	6.5	4.1
b)	41	3.3	5.3	4
c)	37	4.6	6.8	3.3
d)	35	4.4	6.7	3.4

Table 4.1: Summarizing table of transient results.

4.4 Conclusions

Four different geometries have been assembled into a compressor entry. The studied geometries are a straight duct, a tapered duct, a convergent nozzle and a Convergent-Divergent nozzle. Steady and transient tests have been performed in an engine test bench for each configuration, thus reproducing the actual performance of each set of intake geometry and turbocharger. The experiments are conducted to assess the influence of the intake geometry not only on compression ratio but also on efficiency and noise emissions near surge conditions. The transient tests are particularly relevant because they consist in a sudden pedal release, which reproduces a driver's tip-out maneuver that may lead the compressor into surge.

- The standard straight duct presents the worst performance in the surge side of the compressor map. Its surge line is the most restrictive, isentropic efficiency at this zone is the lowest and it is the most likely to enter into surge and produce the maximum harm in driving-like conditions.
- The tapered duct improves the surge margin and slightly increases the pressure ratio at high mass flow rates as well. It presents an enhanced isentropic efficiency and the number of surge cycles (and surge frequency) is reduced when surge happens due to a sudden pedal release.
- The Convergent-Divergent nozzle shifts the surge line slightly more than the tapered duct, presenting the greatest isentropic efficiency of all the studied geometries at the surge side of the compressor map. Additionally, the performance at the transient tests is improved in terms of surge occurrence and maximum rate of pressure change.
- Finally, the convergent nozzle behavior is similar to its C-D nozzle counterpart, but it produces the maximum surge margin gain and intake orifice noise is strongly reduced. However, it performs poorly at high mass flow rates, showing a reduced pressure ratio due to the reduced flow effective cross-section at the inducer plane.

The most promising inlet geometries are therefore the tapered duct and the Convergent-Divergent nozzle. However, the limitations of this study should be taken into account: only intake geometries that are easy to construct have

been considered, and they may not be optimized; in addition, only the surge side of the compressor map and an isospeed line (160 krpm) has been measured. These inlet geometries may change the compressor performance at other operating conditions.

Moreover, some particular aspects of the impact of the intake geometries cannot be explained without additional information, such as the efficiency increase of the C-D nozzle. To shed more light on this topic, 3D-CFD simulations of the whole compressor with similar intake geometries are performed in Chapter 5.

Chapter 4 Bibliography

[10] D. Evans and A. Ward. "Minimizing Turbocharger Whoosh Noise for Diesel Powertrains." *SAE Technical Paper* 2005-01-2485 (2005). DOI: 10.4271/2005-01-2485 (cit. on pp. 3, 11, 96).

[28] J. R. Serrano, X. Margot, A. Tiseira, and L. M. García-Cuevas. "Optimization of the inlet air line of an automotive turbocharger." *International Journal of Engine Research* 14(1) (2013), pp. 92–104. DOI: 10.1177/1468087412449085 (cit. on pp. 6, 9, 28, 96).

[45] E. M. Greitzer. "Surge and rotating stall in axial flow compressors–Part I: Theoretical compression system model." *Journal of Engineering for Gas Turbines and Power* 98(2) (1976), pp. 190–198. DOI: 10.1115/1.3446138 (cit. on pp. 8, 95).

[46] M. C. Huppert. *Compressor surge*. Tech. rep. 1965 (cit. on pp. 8, 96).

[47] D. Fink, N. Cumpsty, and E. Greitzer. "Surge dynamics in a free-spool centrifugal compressor system." *Journal of Turbomachinery* 114(2) (1992), pp. 321–332. DOI: 10.1115/91-GT-031 (cit. on pp. 8, 96).

[48] F. Willems and B. De Jager. "Modeling and control of compressor flow instabilities." *Control Systems, IEEE* 19(5) (1999), pp. 8–18. DOI: 10.1109/37.793434 (cit. on pp. 8, 96).

[49] A. Epstein, J. Ffowcs Williams, and E. Greitzer. "Active suppression of aerodynamic instabilities in turbomachines." *Journal of Propulsion and Power* 5(2) (1989), pp. 204–211. DOI: 10.2514/3.23137 (cit. on pp. 8, 96).

[50] J. T. Gravdahl, O. Egeland, and S. O. Vatland. "Drive torque actuation in active surge control of centrifugal compressors." *Automatica* 38(11) (2002), pp. 1881–1893. DOI: 10.1016/S0005-1098(02)00113-9 (cit. on pp. 8, 96).

[54] I. Ariga, N. Kasai, S. Masuda, Y. Watanabe, and I. Watanabe. "The effect of inlet distortion on the performance characteristics of a centrifugal compressor." *Journal of Engineering for Gas Turbines and Power* 105(2) (1983), pp. 223–230. DOI: 10.1115/82-GT-92 (cit. on pp. 9, 96).

[55] G. Capon and T. Morris. "The effect of air inlet system features on automotive turbocharger compressor performance." In: 9^{th} *International Conference on Turbochargers and Turbocharging*. 2010 (cit. on pp. 9, 96).

[56] O. Baris and F. Mendonça. "Automotive Turbocharger Compressor CFD and Extension Towards Incorporating Installation Effects." In: *Proceedings of ASME Turbo Expo 2011: Power for Land, Sea and Air*. ASME, 2011, pp. 2197–2206. DOI: 10.1115/GT2011-46796 (cit. on pp. 9, 10, 96).

[57] J. Galindo, J. R. Serrano, X. Margot, A. Tiseira, N. Schorn, and H. Kindl. "Potential of flow pre-whirl at the compressor inlet of automotive engine turbochargers to enlarge surge margin and overcome packaging limitations." *International journal of heat and fluid flow* 28(3) (2007), pp. 374–387. DOI: 10.1016/j.ijheatfluidflow.2006.06.002 (cit. on pp. 9, 96, 128).

[58] R. Lang. "Contribución a la Mejora del Margen de Bombeo en Compresores Centrífugos de Sobrealimentación." PhD thesis. Universitat Politècnica de València, 2011 (cit. on pp. 9, 96, 104, 120, 147).

[59] J. Galindo, F. Arnau, A. Tiseira, R. Lang, H. Lahjaily, and T. Gimenes. "Measurement and Modeling of Compressor Surge on Engine Test Bench for Different Intake Line Configurations." *SAE Technical Paper* 2011-01-0370 (2011). DOI: 10.4271/2011-01-0370 (cit. on pp. 9, 10, 99, 125).

[60] J. Desantes, J. M. Luján, B Pla, and J. Soler. "Potential of using a nozzle at the compressor inlet of a high-speed direct-injection diesel engine." *Proceedings of the Institution of Mechanical Engineers, Part D: Journal of Automobile Engineering* 225(2) (2011), pp. 178–189. DOI: 10.1243/09544070JAUTO1429 (cit. on pp. 9, 104, 121, 125, 135, 148).

[61] J. Galindo, A. Tiseira, F. J. Arnau, and R. Lang. "On-Engine Measurement of Turbocharger Surge Limit." *Experimental Techniques* 37(1) (2013), pp. 47–54. ISSN: 1747-1567. DOI: 10.1111/j.1747-1567.2010.00697.x (cit. on pp. 9, 10, 99, 150).

[62] J. Luján, V. Bermúdez, J. R. Serrano, and C. Cervelló. "Test bench for turbocharger groups characterization." *SAE Technical Paper* 2002-01-0163 (2002). DOI: 10.4271/2002-01-0163 (cit. on pp. 9, 44, 96).

[64] J. Galindo, H. Climent, C. Guardiola, and A. Tiseira. "On the effect of pulsating flow on surge margin of small centrifugal compressors for automotive engines." *Experimental Thermal and Fluid Science* 33(8) (2009), pp. 1163–1171. DOI: 10.1016/j.expthermflusci.2009.07.006 (cit. on pp. 10, 96, 99).

[65] A. Broatch, J. Galindo, R. Navarro, and J. García-Tíscar. "Methodology for experimental validation of a CFD model for predicting noise generation in centrifugal compressors." *International Journal of Heat and Fluid Flow* 50 (2014), pp. 134–144. DOI: 10.1016/j.ijheatfluidflow.2014.06.006 (cit. on pp. 10, 96, 120, 124).

[71] A. Karim, K. Miazgowicz, B. Lizotte, and A. Zouani. "Computational Aero-Acoustics Simulation of Compressor Whoosh Noise in Automotive Turbochargers." *SAE Technical Paper* 2013-01-1880 (2013). DOI: 10.4271/2013-01-1880 (cit. on pp. 11, 96).

[72] T. Raitor and W. Neise. "Sound generation in centrifugal compressors." *Journal of Sound and Vibration* 314 (2008), pp. 738–756. ISSN: 0022-460X. DOI: 10.1016/j.jsv.2008.01.034 (cit. on pp. 11, 97).

[73] C. Teng and S. Homco. "Investigation of Compressor Whoosh Noise in Automotive Turbochargers." *SAE Int. J. of Passeng. Cars-Mech. Syst.* 2(1) (2009), pp. 1345–1351. DOI: 10.4271/2009-01-2053 (cit. on pp. 11, 96).

[75] A. Broatch, J. Galindo, R. Navarro, J. García-Tíscar, A. Daglish, and R. K. Sharma. "Simulations and measurements of automotive turbocharger compressor whoosh noise." *Engineering Applications of Computational Fluid Mechanics* 9(1) (2015). DOI: 10.1080/19942060.2015.1004788 (cit. on pp. 11, 96, 122).

[76] A. J. Torregrosa, A. Broatch, R. Navarro, and J. García-Tíscar. "Acoustic characterization of automotive turbocompressors." *International Journal of Engine Research* 16(1) (2015), pp. 31–37. DOI: 10.1177/1468087414562866 (cit. on pp. 11, 98, 137).

[118] J. Galindo, J. R. Serrano, C. Guardiola, and C. Cervelló. "Surge limit definition in a specific test bench for the characterization of automotive turbochargers." *Experimental Thermal and Fluid Science* 30(5) (2006), pp. 449–462. DOI: 10.1016/j.expthermflusci.2005.06.002 (cit. on p. 95).

[119] B. de Jager. "Rotating stall and surge control: A survey." 2 (1995), pp. 1857–1862. DOI: 10.1109/CDC.1995.480612 (cit. on p. 96).

[120] D. L. Gysling, J Dugundji, E. Greitzer, and A. Epstein. "Dynamic control of centrifugal compressor surge using tailored structures." *Journal of Turbomachinery* 113(4) (1991), pp. 710–722. DOI: 10.1115/90-GT-122 (cit. on p. 96).

[121] A. Whitfield, A. Sutton, and H. Leonard. "The development of turbocharger compressors with improved surge margin." *ImechE C433/063* (1991), p. 9 (cit. on p. 96).

[122] A. Engeda, Y. Kim, R. Aungier, and G. Direnzi. "The inlet flow structure of a centrifugal compressor stage and its influence on the compressor performance." *Journal of fluids engineering* 125(5) (2003), pp. 779–785. DOI: 10.1115/1.1601255 (cit. on p. 96).

[123] R. C. Pampreen. *Compressor surge and stall*. Concepts Eti Vermont, 1993 (cit. on p. 96).

[124] E. Jenny. "Uber Instationnäire Vorgänge in Radialverdichtern Insbesondere in Aufladegruppen Von Verbrennungmotoren." *Schweiz. Bauztg* 79(46) (1961), pp. 802–817 (cit. on p. 96).

[125] E. Guillou, M. Gancedo, E. Gutmark, and A. Mohamed. "PIV investigation of the flow induced by a passive surge control method in a radial compressor." *Experiments in fluids* 53(3) (2012), pp. 619–635. DOI: 10.1007/s00348-012-1310-8 (cit. on pp. 97, 120).

[126] O. Leufvén and L. Eriksson. "Time to surge concept and surge control for acceleration performance." In: *Proceedings of the* 17^{th} *IFAC World Congress, 2008*. International Federation of Automatic Control (IFAC). 2008, pp. 2063–2068. DOI: 10.3182/20080706-5-KR-1001.00350 (cit. on p. 101).

[127] C.-H. Wang and C.-C. Wang. "Design and Implementation of Intelligent Surge Controller for Modern Turbo Charged Automobiles." *International Journal of Fuzzy Systems* 16(2) (2014), pp. 222–232 (cit. on p. 101).

Chapter 5

3D-CFD assessment of inlet geometry influence on compressor performance

Contents

5.1 Introduction

Although the impact of the compressor inlet geometry on its surge line and performance can be assessed by comparing experimental measurements, as described in Chapter 4, only a better understanding of the flow behavior may allow researchers to extract design guidelines. Due to the complex geometry of the compressor and packaging constraints, it is hard to perform non-intrusive flow measurements near the compressor mouth, neither it is possible to have local measurements along the impeller passages. Experimental measurements can be made with, for example, optical techniques such as LDV or PIV [125]. However, in order to have a complete solution of the flow field, CFD calculations provide results that have proven to be meaningful in the past for studying several compressor inlet geometries [128] and noise emissions [65, 114].

In this chapter, the influence of different promising compressor inlet geometries in its performance is analyzed using the CFD software STAR-CCM+ [79], allowing a fundamental analysis of the flow structures that appear within each configuration. In Section 5.2, the geometries selected are introduced and described. The methodology and the numerical setup is noted in Section 5.3. The discussion of the results is written in Section 5.4 and finally, the concluding remarks are shown in Section 5.5.

5.2 Background and selection of geometries

The geometries selected for this work are inspired on the ones that have been experimentally analyzed in Chapter 4. Steady and transient measurements were made using an engine test bench in order to simulate real pulsating conditions. A straight duct will be used as the reference case. The modeled geometry is shown in Fig. 5.1(a) with the impeller on the bottom part.

The first of the proposed geometries is the tapered duct. It is created by reducing the inlet duct diameter approximately from 2 times to 1 time the impeller diameter in the direction of the incoming flow. Previous studies [58], found a surge margin increase when using this intake of about 20%. A detailed view of this geometry is shown in Fig. 5.1(b).

The next intake line is composed by a nozzle with a convergent part that reaches a throat and then a divergent part that recovers the upstream di-

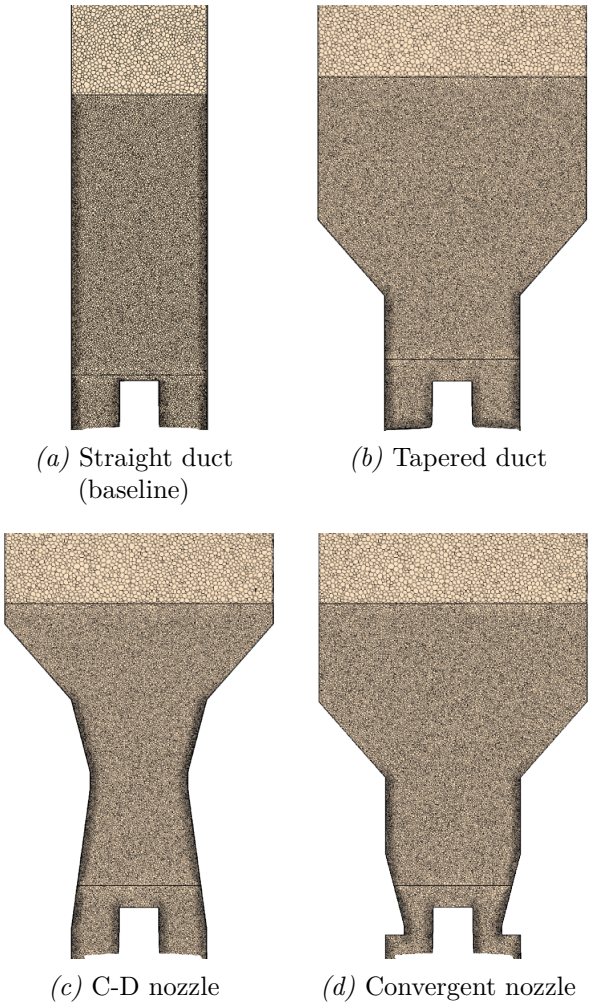

(a) Straight duct (baseline)

(b) Tapered duct

(c) C-D nozzle

(d) Convergent nozzle

Figure 5.1: Inlet geometries outline and cross-section of mesh.

ameter and discharges close to the inducer. The potential benefits of this geometry were described by Desantes et al. [60] in a study where a surge margin improvement of 30% and a slight efficiency rise was observed on the whole compressor map. Alas, at high mass flow rates a worsening of the compressor performance appeared. A section of the Convergent-Divergent (C-D) nozzle designed for this work can be seen in Fig. 5.1(c).

Finally, the previous configuration is modified by removing the divergent part from the throat, so that it discharges directly on the inducer. The inlet section is apparently reduced, virtually modifying the trim of the compressor and greatly affecting on its performance. In Fig. 5.1(d) is depicted a detailed view of this convergent nozzle.

The 3D model of the compressor used in this study and the compressor used in Chapter 4 in the aforementioned experimental work are much alike (same number of blades and splitters, similar trim...). A slight difference in impeller diameter is corrected scaling the inlet geometries accordingly.

5.3 CFD setup and methodology

Concerning the numerical domain, all the cases share the housing, the rotor, the volute and the outlet duct, differing only in their specific inlet geometry. In Fig. 5.2 is depicted a close-up view of the geometry and the mesh of the compressor wheel. It can be appreciated that the full 360°-resolved rotor is considered, including the tip clearance between the blade tips and the housing in CAD-like conditions, since Galindo et al. [129] proved that the actual tip profile in working conditions does not affect noise prediction and only increases slightly pressure ratio and compressor efficiency. The mesh settings were previously used by Navarro [77] for a similar compressor showing grid independence. The complete mesh is composed by about 10 million polyhedral cells, distributed among the different regions as seen in Table 5.1. The wall resolution is increased by reducing the cell size and adding prism layers, producing y^+ values below 5 on the surfaces, thus assuring these cells are in the viscous sub-layer zone and properly solving the flow [114]. For a better solution of the flow structures in the inlet ducts near the impeller, a finer meshing is applied in these areas, specifically two inducer diameters upstream from the inducer planes, a distance in which backflows are expected to be confined [74], as can be observed in Figure 5.1.

Regarding the numerical setup, the STAR-CCM+ [79] segregated flow solver with ideal gas properties for the air is employed. The turbulent approach is addressed using Detached Eddy Simulation, with $k-\omega$ SST submodel "which functions as a sub-grid-scale model in regions where the grid density is fine enough for a large-eddy simulation, and as a Reynolds-averaged model in regions where it is not" [130]. Several researchers [131, 132, 75]

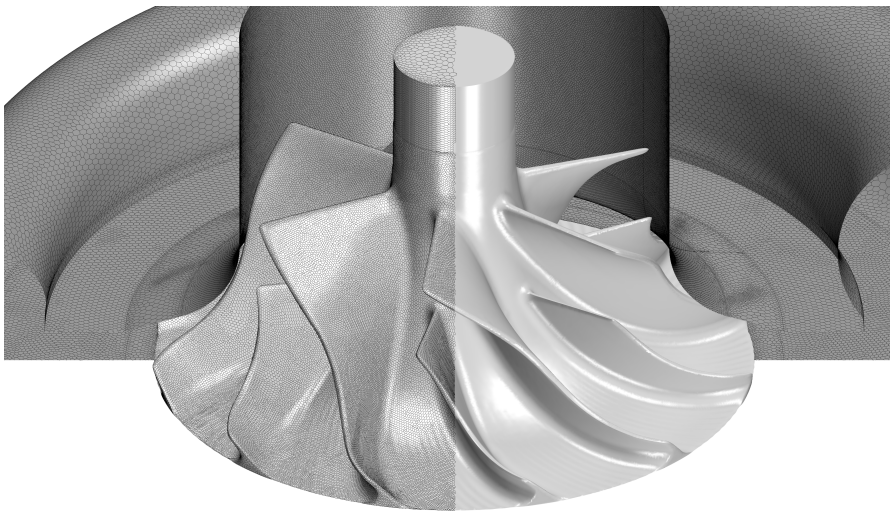

Figure 5.2: Rotor geometry and mesh.

Region	**Cells (M)**	**Intake**	**Cells (M)**
Rotor	4.1	Straight	1.9
Diff.,volute	1.6	Tapered	4.3
Outlet	0.7	C-D nozzle	3.9
Intake	1.9-4.4	Conv. nozzle	4.4

Table 5.1: Millions of cells in each region, distinguishing between intake geometries.

have satisfactorily used this same approach with similar compressor simulations. The problem is solved using a 2^{nd} order transient solver, with a time step equivalent to a compressor wheel spin of 4°. This time-step size allows a proper prediction of noise emission in plane wave range, enough to allow the proposed noise assessment [77].

Due to the high computational effort that each simulation implies, it is decided to analyze two operating conditions per geometry along the 160 krpm isospeed line, one point at 30 g/s close to the surge line to study the flow structures that appear at these conditions, and one at operating point at 100 g/s to determine the impact of the inlet geometries on the global variables of the compressor. Additionally to the mass flow rate, it is imposed the compressor outlet pressure at 2 bar and the compressor speed at 160 krpm.

Once the relevant signals have reached periodicity (after ≈100 compressor rotations), the simulation is run for 170 additional rotations to record time history of variables. Time-averaged values of pressure, temperature and velocity at the whole domain can be then obtained for post processing, creating scalar scenes as well as global variables, namely the compressor efficiency and the compression ratio, defined in Equations 4.2.2 and 5.1 respectively.

$$\Pi_{t,t} = \frac{p_{out,t}}{p_{in,t}} \tag{5.1}$$

Concerning the noise emission analysis, surface average monitors are set in two cross-sections close both to inlet and outlet corresponding boundaries. Then, using the Method of Characteristics (MoC) as defined in Eq. 5.2 [133], the forward and backward pressure waves are obtained.

$$\begin{aligned} p_{forw} &= p_{ref}\left[\frac{1}{2}\left(1+\left(\frac{p}{p_{ref}}\right)^{\frac{\gamma-1}{2\gamma}}\left(1+\frac{\gamma-1}{2}M\right)\right)\right]^{\frac{2\gamma}{\gamma-1}} \\ p_{back} &= p_{ref}\left[\frac{1}{2}\left(1+\left(\frac{p}{p_{ref}}\right)^{\frac{\gamma-1}{2\gamma}}\left(1-\frac{\gamma-1}{2}M\right)\right)\right]^{\frac{2\gamma}{\gamma-1}} \end{aligned} \tag{5.2}$$

Broatch et al. [65] showed that these MoC-decomposed pressure signals obtained at cross-section were comparable to that measured experimentally at plane-wave range. According to Eriksson [134], the threshold of this range is set by the onset of the first asymmetric mode, which occurs at a frequency of:

$$f_{c,a} = 1.84\frac{a}{\pi D}(1-M^2)^{1/2}. \tag{5.3}$$

This expression predicts the onset of the asymmetric modes at 3.8 kHz and 6 kHz for inlet and outlet ducts, respectively. The Power Spectral Density (PSD) of these pressure traces is calculated using Welch's overlapped segmented averaged [135] approach. The Hamming function is selected for defining the window length of the blocks, setting the frequency resolution in

100 Hz for the outlet PSD and 50 Hz for the inlet (0.01 s are recorded). Additionally, the sound intensity is calculated using Eq. 5.4, according to Holland and Davies [136]. A frequency range from 300 Hz to the corresponding first asymmetric mode onset frequencies is considered for computing the Sound Intensity Level (SIL). Low-end frequencies are not taken into account for the calculation of this parameter due to their reduced impact on the human subjective noise perception. A reference sound intensity of 10^{-12} W/m^2 is used the SIL calculation (Eq. 4.1).

$$\begin{aligned} I &= I_{forw} - I_{back} \\ &= \frac{1}{\rho_0 a_0}\left(|\hat{p}_{forw}|^2(1+M)^2 - |\hat{p}_{back}|^2(1-M)^2\right) \quad \frac{W}{m^2} \end{aligned} \tag{5.4}$$

5.4 Results and discussion

Regarding the experimental tests exposed in Section 4.3, the results showed a clear advantageous influence on the compressor parameters, highlighting the increased surge margin of all the proposed configurations against the baseline straight duct. A qualitative summary of the surge margin improvements found in different researches is shown in Table 5.2. Each plus sign (+) represents a surge improvement of 10%.

Auth./Geom.	**Tap. duct**	**C-D Nozzle**	**C. Nozzle**
Galindo et al. [59]	++		
Desantes et al. [60]		+++	
Chapter 4	+	+	++

Table 5.2: Summary table of the impact of different inlet geometries from different studies on the compressor surge margin.

In the case of the tapered duct and the C-D nozzle, the compression ratio at high mass flow rates was kept without detriment and the efficiency was also kept or slightly increased with the C-D nozzle through all the compressor map. Conversely, the convergent nozzle showed an efficiency decrease and worse compression ratio at high mass flow rates but lower noise emission, both phenomena possibly caused by the cross-section restriction of the throat.

It would be desirable to find the actual surge limit of each configuration at a given compressor speed, however with the current methodology it would require an excessive computational effort. Instead, this work is mainly devoted to the phenomena involved with the inception of surge appearance, studying, as aforementioned, different quantitative and qualitative parameters that may point out the closeness of this stability limit. However, to avoid neglecting the behavior of the compressor at other operating conditions, in section 5.4.2 the compressor performance is assessed as well.

5.4.1 Points of low mass flow rate

Focusing the attention on the low mass flow rate operating points, Figure 5.3 depicts the streamlines upstream the compressor for different intake geometries. Streamlines in blue represent the downstream flow coming from the inlet boundary and red streamlines highlight the backflow that is being recirculated from the inducer plane of the compressor.

As can be seen in Fig. 5.3, each configuration produces a different recirculation pattern. In the reference straight duct, the recirculation reaches about two inducer diameters upstream of the wheel, but for the C-D nozzle, this region is contained in the divergent part, with a length of about an inducer diameter. With the convergent nozzle, the recirculation is only produced within the free space between the throat and the wheel. Conversely, the tapered geometry offers a sudden increase of the diameter to the backflows that travel upstream, where lower inlet velocities are found, reducing the momentum and swirl transmission between both flows and causing a recirculation region larger than five inducer diameters. It is worth mentioning that this recirculation phenomenon appears at low mass flow rates, positively impacting on the stability of the compressor [51]. It generates a rise of the incoming mass flow rate and thus, an increase in momentum. In addition, the available cross-section the flow has to enter through the inducer plane is reduced, implying a further rise in velocity and momentum.

Using the time-averaged flow parameters at the inducer plane, the incoming and outgoing (recirculation) mass flow rates and the incoming momentum relative to the momentum of the straight configuration are calculated. In Table 5.3 a quantitative evaluation of these indicators is provided.

Compared with the reference configuration, the results show that higher

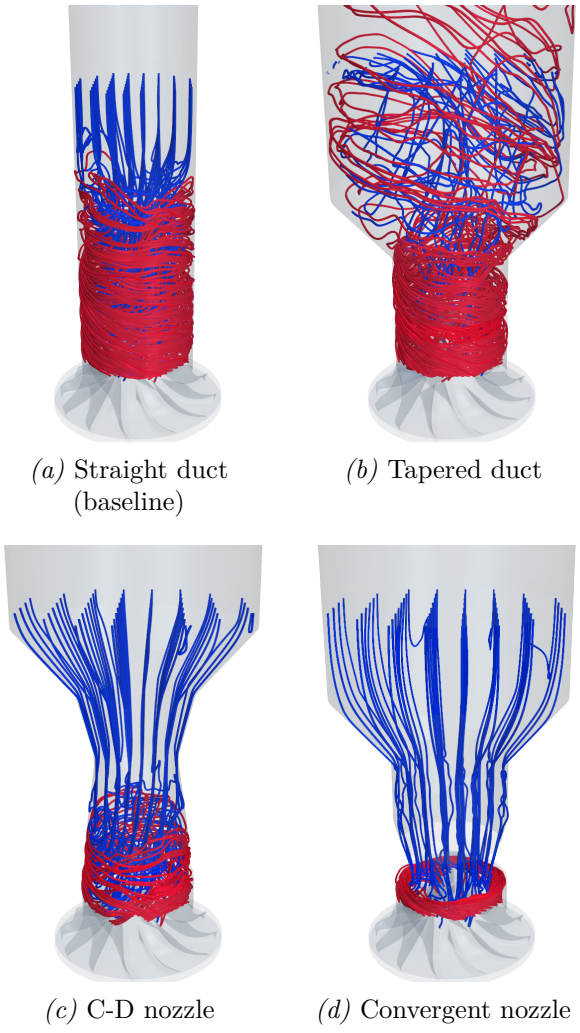

(a) Straight duct (baseline)

(b) Tapered duct

(c) C-D nozzle

(d) Convergent nozzle

Figure 5.3: Inlet (blue) and recirculated (red) streamlines for the different inlet geometries at low mass flow rate.

recirculation mass flow rates are obtained with the tapered duct and lower with the nozzles. Although this is consistent with the length of the recirculations, it does not imply a direct correlation with the improvements of surge margin obtained on the experimental tests carried out in Chapter 4. A similar reasoning can be drawn from the incoming momentum results. Thus, in spite

	Str.	**Tap.**	**CD-N**	**C-N**
Upstream (g/s)	8.2	8.5	7.0	6.3
Downstream (g/s)	38.2	38.5	37.0	36.3
Momentum (%)	100	100.87	91.82	91.48

Table 5.3: Recirculated mass flow ratios at low mass flow rate.

of being interesting indicators of the state of the flow at the compressor inlet, these parameters cannot be directly used to predict the surge appearance.

Please note that due to the rotation of the wheel, the tangential velocity of the recirculated flow is high and has a swirl component that is transferred to the incoming flow, acting like a pre-swirl device, increasing pre-rotation of flow [57, 137, 138]. The increase of momentum and reduction of incidence angle due to those backflows delay onset of surge.

Other parameters that can be extracted from the state of the flow at the compressor inducer are the angles of the velocity triangle of the compressor inducer, defined in Fig 5.4. Using a cylindrical coordinate system, the axial and tangential time-averaged components of the velocity are considered in an annulus-shape region in the inducer plane. The annulus is defined between the spans 0.3 and 0.7 of the impeller passage, representing a characteristic incoming flow region (the recirculation area is skipped, as well as the area very close to the hub). The inducer plane is moved an offset of 2 mm upstream of the leading edge, avoiding the perturbations of the leading edges on the averaged velocity components. Additionally, between the aforementioned spans where the annulus is defined, the blade angle at the leading edge ($\beta_{l.e.}$) is also averaged. Then, using Equations 5.5, 5.6 and 5.7, α and β angles and the incidence are respectively obtained.

$$\tan\alpha = \frac{c_u}{c_a} \tag{5.5}$$

$$\tan\beta = \frac{c_u - u}{c_a} = \frac{c_u - \omega\ r}{c_a} = \frac{c_u - N(rpm)\frac{2\pi}{60}\ r}{c_a} \tag{5.6}$$

$$Incidence = \beta - \beta_{l.e.} \tag{5.7}$$

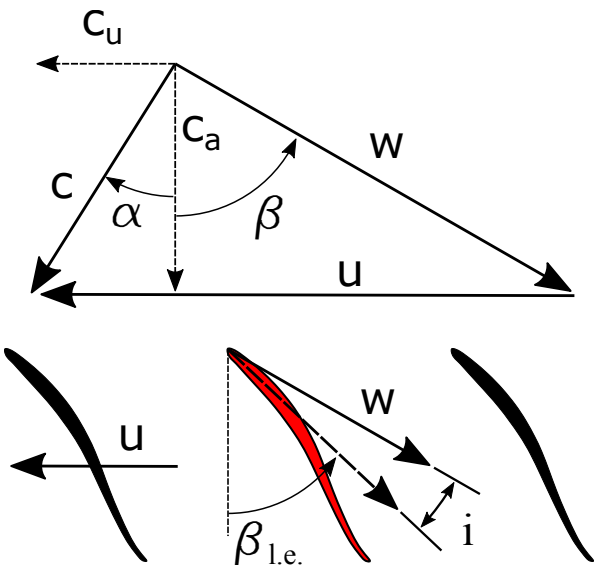

Figure 5.4: Velocity triangle at the compressor inducer plane.

The results of the velocity triangle angles and incidence for the low mass flow rate operating points are shown in Table 5.4.

Angle (°)	**Str.**	**Tap.**	**CD-N**	**C-N**
Alpha	36.8	36.9	39.6	45.1
Beta	55.6	56.0	57.0	54.4
Incidence	8.6	9.0	10.0	7.4

Table 5.4: α and β angles and incidence at low mass flow rate.

The first feature that outstands when analyzing Table 5.4 is the non-null values of the α terms for all cases, even though there are no pre-swirling devices mounted on the compressor inlet. This is only explained by a swirl transmission of the recirculated flow to the incoming stream. This mechanism is produced due to the rotation of the wheel, which sets a high tangential component of the flow that exits the inducer in an upward direction. Then, depending on different factors, such as the available recirculation region, the recirculated mass flow rate and the outgoing swirl, the transmission of swirl may vary and a different alpha angle will be produced. On the other side, the beta angle depends on the alpha angle, the speed of the compressor wheel (which is constant in this case for all the configurations), and the axial compo-

nent of the incoming flow. It is worth mentioning that a higher recirculation imply higher axial velocities, which affects these angles (see Table 5.3).

Analyzing the results obtained for the simulations of low mass flow rates displayed in Table 5.4, it is observed that a similar velocity triangle is obtained with the straight and tapered ducts. This is consistent with the results obtained in Table 5.3, where similar values of backflows were obtained with these two intake geometries. Conversely, with both nozzles is obtained a higher α angle, implying that more swirl transfer is being produced. However, the lower recirculation of the C-D nozzle produce a higher incoming area and lower axial average velocities on the annular section where the angles are calculated, producing a slightly higher β angle and incidence. Finally, the combination of the acceleration of the flow due to the throat restriction and the reduced recirculation flow produce an increased swirl transfer and α angle, which produce in this case a lower β angle and incidence, improving the flow attachment in the suction face of the blades and thus, the stability increases. Again, in spite of being interesting parameters of the behavior of the flow at the compressor inlet, these angles cannot be taken independently as unique indicators of the closeness of the surge limit.

The reach of the recirculation and its impact on the incoming flow may also be graphically analyzed thanks to the longitudinal sections shown in Fig. 5.5. In these figures, combinations of linear integral convolutions [116] of the time-averaged velocity are used with the mean temperature in the color field. In addition, average velocity vectors and a null axial velocity line are added to the figures, highlighting backflow region. The location of the inducer plane is marked in each geometry.

The solutions of the reference case and the tapered duct are shown in Figs. 5.5(a) and 5.5(b), where the backflows freely traveling upstream can be seen, transferring swirl and enthalpy to the incoming flow. Notice the non-axisymmetry of the time-averaged flow, particularly at the tapered duct (Fig. 5.5(b)). This is due to the non-axisymmetric shape of the volute. On the other side, in Figs. 5.5(c) and 5.5(d) it can be observed how the nozzles confine this region, limiting that transfer. As aforementioned, higher confinement of the backflows implies lower meridional momentum transfer and thus, a different velocity triangle configuration.

The same variables used in Fig. 5.5 are depicted in Fig. 5.6 on the inducer plane sections of all the configurations, seeking an understanding of secondary

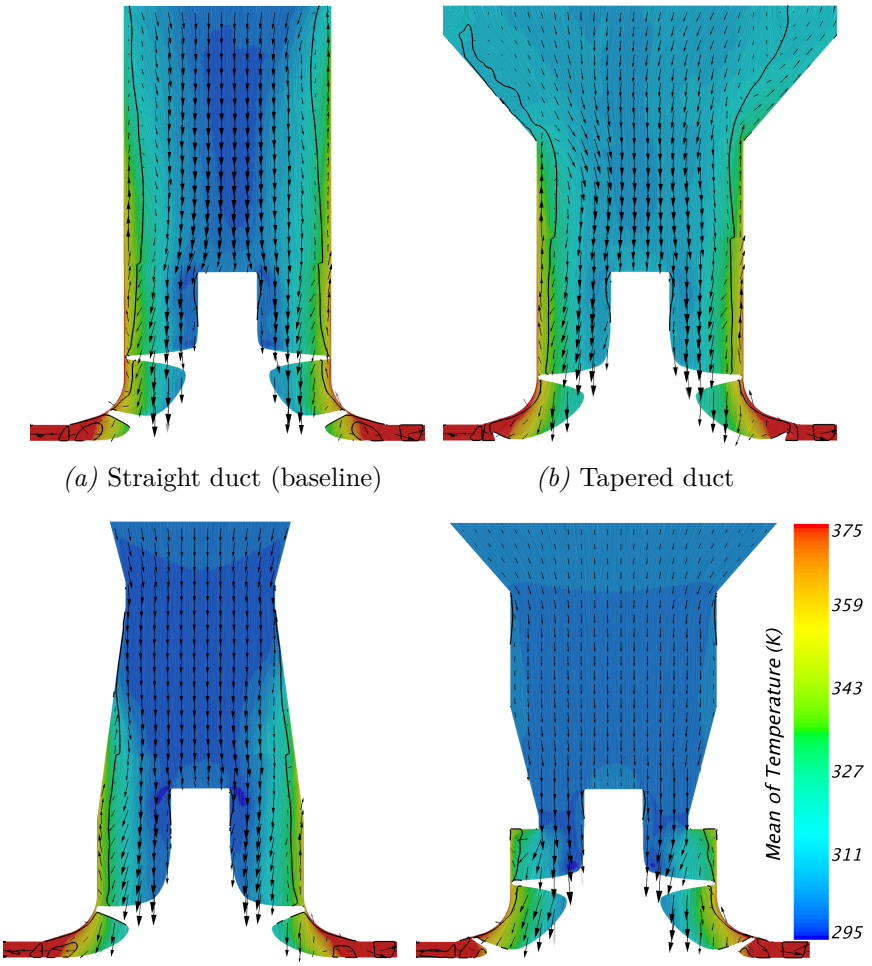

(a) Straight duct (baseline) *(b)* Tapered duct

(c) C-D nozzle *(d)* Convergent nozzle

Figure 5.5: Axial section of linear integral convolution of mean velocity, scalar of mean temperature, mean velocity vectors and black solid line indicates null axial velocity for the low mass flow rates simulations.

flows. However, the pre-rotation due to the recirculation already commented (see α values in Table 5.4) dominates over other secondary flows. Higher temperatures can be seen in the inducer plane of the tapered configuration (5.6(b)), not only across the incoming boundary but also the backflows are hotter compared with the results of the nozzles. The explanation resides in

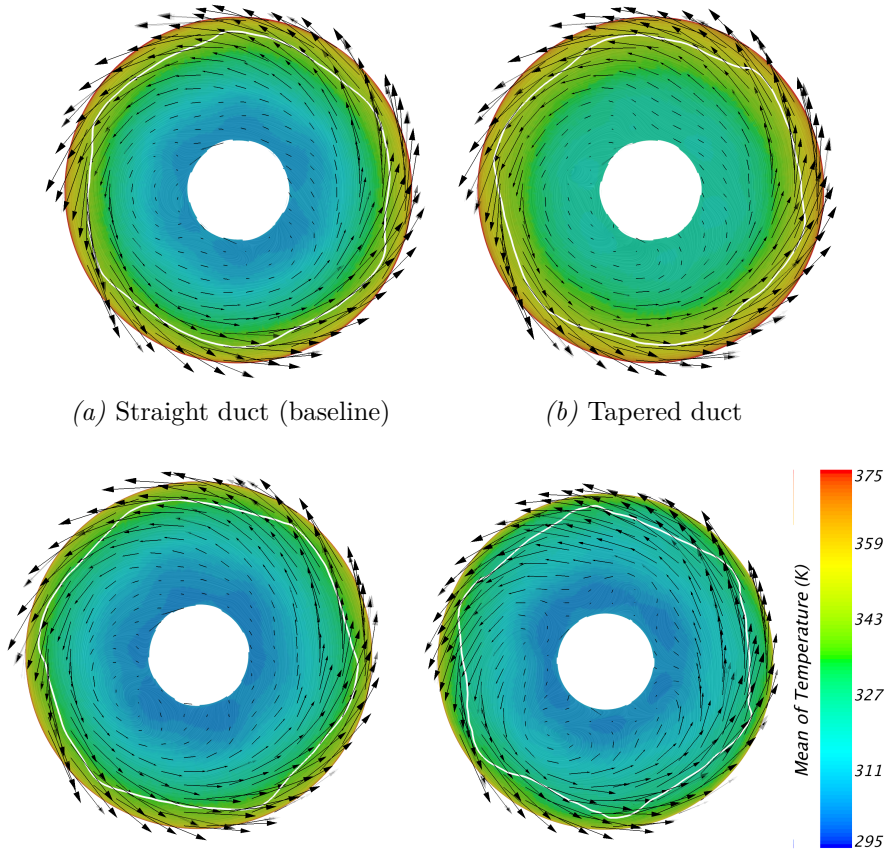

(a) Straight duct (baseline) *(b)* Tapered duct

(c) C-D nozzle *(d)* Convergent nozzle

Figure 5.6: Inducer cross-section of linear integral convolution of mean velocity, scalar of mean temperature, mean velocity vectors and white solid line indicates null axial velocity for the low mass flow rates simulations.

the backflows that start in a region where the gas is partially compressed and heated, implying that the higher the incoming temperature the higher the temperature of the outgoing backflows, what increases, additionally, the incoming flow temperature. This is a problem that feeds itself back and produces an amplified solution, which should be considered for the selection of materials that can bear such temperatures. On the other side, the velocity vectors and the backflow contour delimitation is similar across all the configurations.

A different approach to analyze the momentum distribution may be done performing a meridional averaging of the axial momentum parameter, as seen in Fig. 5.7. The solid line indicates the region of null meridional averaged momentum, and thus null meridional averaged velocity.

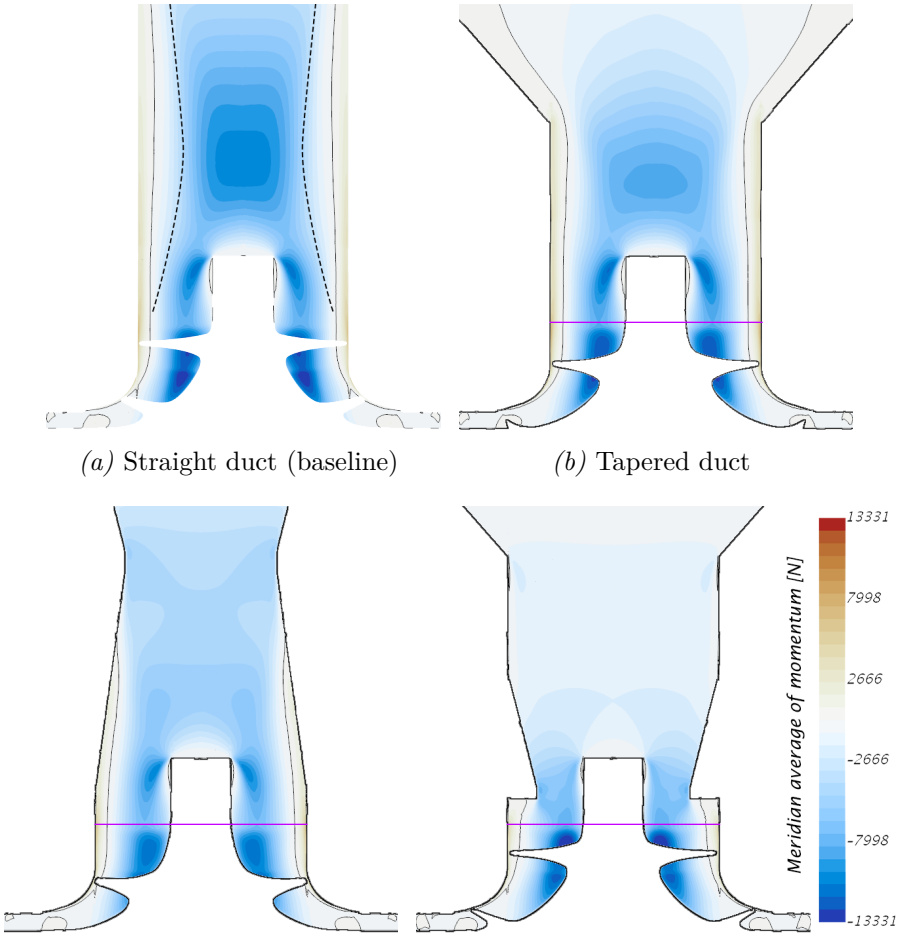

(a) Straight duct (baseline) *(b)* Tapered duct

(c) C-D nozzle *(d)* Convergent nozzle

Figure 5.7: Axial section of meridian average of momentum and line of null momentum.

First, a local maximums of axial velocity are found upstream the impeller nut for the straight and tapered ducts. Incoming velocity contours show a C-D nozzle-like pattern due to the backflows. This effect is clearer for the

	Str.	**Tap.**	**CD-N**	**C-N**
$\Pi_{t,t}$	2.12	2.11	2.13	2.15
η_s	56.3	56.1	58.5	59.2
T_{ind} (°C)	46.3	49.1	41.6	39.1

Table 5.5: Results of compression ratio, efficiency and average incoming temperature for the low mass flow rate points.

straight duct (see dashed line, made just for remarking this effect). In fact, the divergent part of this "nozzle" may reach an angle that the flow cannot withstand without detachment with lower mass flow rate. Contradictorily, the acceleration of the flow in the throat and thus, the momentum on the inducer plane, is lower for the C-D nozzle. This is due to the lower room occupied by the backflows in the latter configuration which in the end sets the effective throat. Finally, the acceleration produced in the convergent nozzle is moved downstream, closer to the impeller and reducing the deflection produced by the nut. Again, due to the confinement of the backflows the momentum in the inducer plane is lower than the baseline, as already seen in Table 5.3.

Regarding the global variables obtained for the points of low mass flow rate, Equations 5.1 and 4.2.2 are used to calculate the compression ratio and the isentropic efficiency and showed in Table 5.5. The average incoming temperature in the inducer plane of each intake geometry is written as well.

Higher efficiencies are found for both nozzles, which correlates with lower recirculation ratios, as seen in Table 5.3. Moreover, considering the values of incoming temperature, it can be concluded that confining the backflows reduces their interaction with the incoming flow and thus, friction losses decrease as well, what translates into an isentropic efficiency rise. However, it is worth noticing that the different friction losses are not the only responsible of different efficiencies, an alteration of the flow pattern on the inducer may also affect the resulting efficiency, as a different compressor trim would do. Conversely, similar results of momentum and recirculation between the tapered duct and the baseline straight duct also produce similar friction losses and thus, efficiencies. The compression ratio is marginally influenced by any intake geometry.

The efficiency rise obtained for both nozzles at low mass flow rate cannot be directly extrapolated to different regions of the compressor map, since the flow structures would be quite different. Nevertheless, as seen in Chapter 4

using a C-D nozzle increases the efficiency not only at points close to surge also at mid mass flow rates and according to Desantes et al. [60] the maximum efficiency of the compressor may even increase by 6 percentage points.

Concerning the noise assessment, the PSD is calculated using the Method of Characteristics wave decomposition defined in Eq. 5.2 and the Welch's averaging introduced in section 5.3. Figure 5.8(a) shows the PSD results at the inlet ducts.

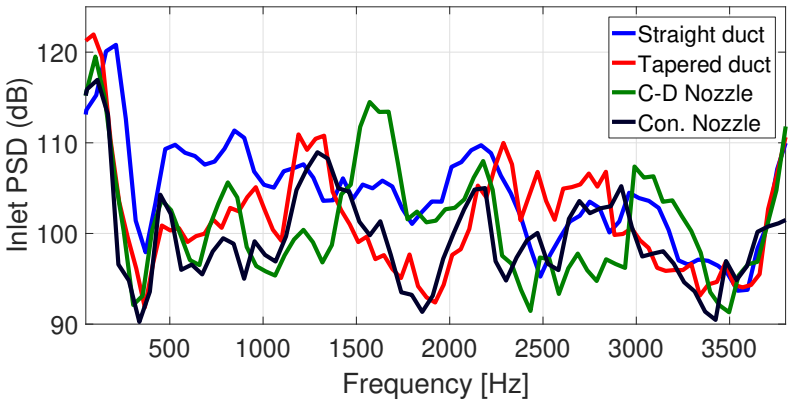

(a) Inlet PSD

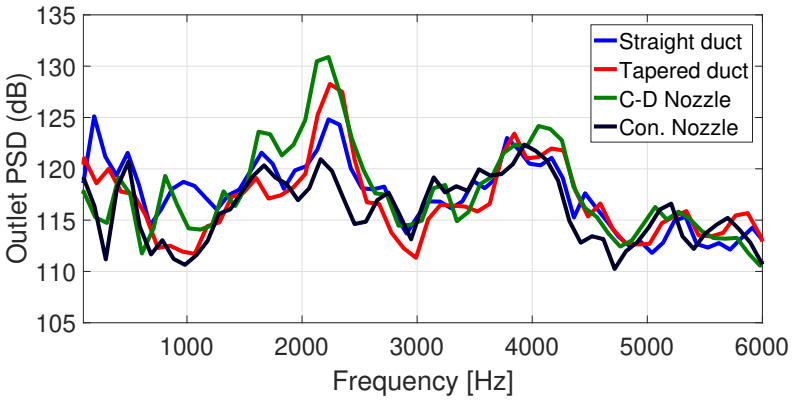

(b) Outlet PSD

Figure 5.8: Inlet and outlet power spectral densities.

It is noticeable that each case presents a different PSD profile for frequencies between 800 and 2500 Hz, coinciding with the common range of the

whoosh noise [139, 140, 141]. Nevertheless, except the straight duct, that presents a flat and noisy spectra at very-low frequencies, the rest of the configurations show a noticeable peak in the aforementioned whoosh noise range possibly responsible of this characteristic noise. Also, all PSD show an important peak at very low frequencies, nearly about 100 Hz or RO=0.04, which according to Sundström et al. [51] is due to the dominant surge oscillation. Using Equations 5.4 and 4.1, the SIL are computed and the results are shown in Table 5.6. It can be seen that, in average, the straight duct produces a significantly higher noise emission, which according to Evans et al. [139], may suggest that the compressor is operating very close to surge, as would be consistent with the experimental campaign.

SIL (dB)	**Str.**	**Tap.**	**CD-N**	**C-N**
Inlet	131	126	126	122
Outlet	151	152	154	149

Table 5.6: Inlet and outlet SIL in a frequency window from 300 to corresponding cut-off frequency.

Broatch et al. [74] stated that the whoosh noise is affected by inducer rotating stall, which in turn, can be enhanced by the onset of low-pressure bubbles that appear at low mass flow rates. In Fig. 5.9 the low-pressure bubbles at the straight inlet duct are shown, displaying the region whose pressure is below 90 kPa. The bubbles rotate in the same direction as the wheel, due to the angular momentum transfer from the recirculations to the intake mass flow, but at a lower speed rate. The rotating speed was assessed and resulted to be spinning nearly at RO=0.5, this is, at around 1333 Hz, which coincide with the aforementioned peaks found within the whoosh noise range [142]. Conversely, from 3500 Hz to higher frequencies, the inlet geometry appears to have no impact on the PSD, except for the convergent nozzle. The PSD spectra profile of this geometry is strongly modified due to the partial blockage of the inducer area. Actually, the convergent nozzle case produce, in average, a lower noise emission (see Table 5.6). The experimental tests carried out in Chapter 4 showed a lower SIL emission of the convergent nozzle inlet as well.

Although the outlet duct does not directly discharge to the ambient, the analysis of its spectra is important since the intensity of the noise is greater than at the inlet ([139], Table 5.6) and therefore the compressor housing and outlet pipe may significantly radiate noise to the surroundings, as described by

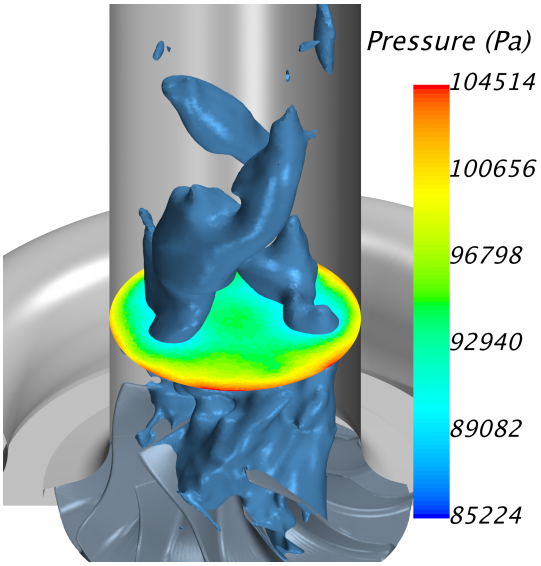

Figure 5.9: Low-pressure bubble at low mass flow rates for the straight duct.

Torregrosa et al. [76]. Additionally, being that the engine is placed downstream of the compressor and it is greatly influenced by the acoustic signature of its intake flow, special attention needs to be paid when coupling both thermal machines. Figure 5.8(b) shows the PSD of the outlet ducts, where a similar spectral profile is generated by all four configurations, differing only in the power density of the peaks around 2200 Hz. Analogously to the inlet PSD, the convergent nozzle case produce the lower peak, whereas the tapered and the C-D nozzle cases produce higher values.

5.4.2 Points of high mass flow rate

At high mass flow rates, the effect of the inlet geometry is clear on the evolution of the static pressure through the intake duct, since the pressure losses grow with the square of the mass flow rate. However, phenomena such as recirculation normally vanish at this conditions, unless a part of the inducer cross-section is physically blocked, like it is in the convergent nozzle case. Along with the fading of recirculation, swirl transfer to the incoming flow also decreases, impacting on the velocity triangles of the inducer plane, which in addition has a higher axial velocity component compared with the low mass

flow rate points. The angles of the velocity triangles of these points are shown in Table 5.7.

Angle (°)	**Str.**	**Tap.**	**CD-N**	**C-N**
Alpha	0.2	0.2	1.1	4.0
Beta	50.1	49.9	44.9	32.9
Incidence	3.1	2.9	-2.1	-14.1

Table 5.7: Alpha and beta angles for the high mass flow cases.

As aforementioned, there is no swirl transmission to the incoming flow, which is kept almost axial until entering the compressor inducer, producing low alpha values. The presence of the throat near of the inducer in the convergent nozzle case generates a detachment of the flow and a rotating bubble that covers the backside of the step and the inducer region close to the shroud, as can be seen in Fig. 5.10. Swirl transfer is produced there, slightly increasing the averaged alpha angle, similarly as found in the low mass flow rate cases.

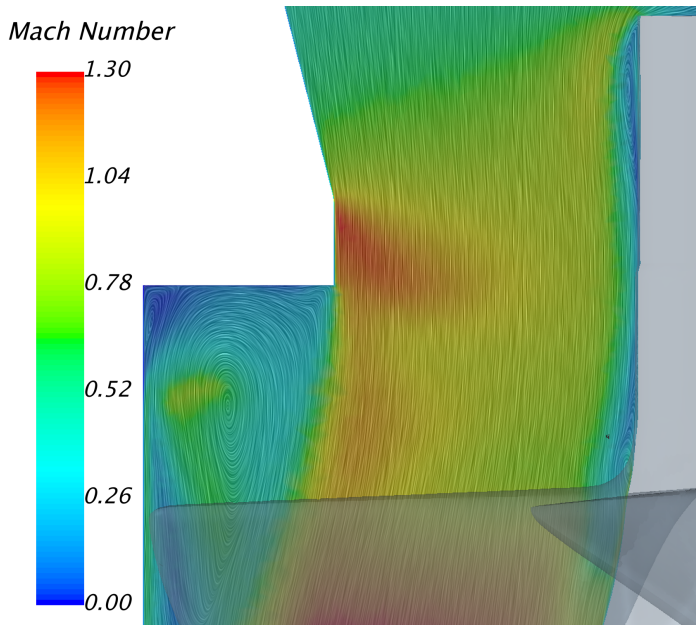

Figure 5.10: LIC of mean absolute velocity with color field of Mach number of convergent nozzle at high mass flow rates.

The lower beta angle of the convergent nozzle is due to the higher axial

velocity generated at the throat, which also noticeably decreases the incidence angle down to -14° and generates the pressure losses that strongly worsens the compressor efficiency. The results of the global variables for the high mass flow rates are written in the Table 5.8.

	Str.	**Tap.**	**CD-N**	**C-N**
$\Pi_{t,t}$	1.65	1.64	1.56	1.11
η_s	63.0	62.3	55.1	14.1

Table 5.8: Results of compression ratio and efficiency for the high mass flow rate points.

The higher pressure losses of the convergent nozzle worsen both the compression ratio and the efficiency. A different point of view to approach this would be assessing the Mach number at the inducer plane. In Fig. 5.10 it can be seen how the Mach number reaches supersonic velocities in some regions of the impeller. First, the throat appears to be partially blocked and even producing super-sonic flows. The presence of shock waves and supersonic flow imply important losses of the total conditions, responsible of the efficiency decrease. The same effect would be found for the rest of the configurations at higher mass flow rates or at the same conditions with a smaller compressor (or with a compressor with a lower trim). It is worth mentioning that this effect is also noticeable with the C-D nozzle, but not as importantly. On the contrary, the tapered duct does not have any worse or better influence on the compression ratio or on the efficiency compared with the straight duct.

5.5 Conclusions

Four compressor inlet geometries were selected and modeled. Compressor simulations with these geometries were made setting two operating points, one close to surge at 30 g/s and one at very high mass flow rates at 100 g/s, both at the same compressor speed of 160 krpm. From the converged simulations, global variables were obtained, local observations in different section planes were assessed and the noise emission produced in both inlet and outlet ducts were measured, using the Method of Characteristics for the wave decomposition.

From the results of each intake geometry in comparison to the baseline at

low mass flow rate can be extracted that:

- Tapered duct: similar results are obtained in all the quantitative parameters that has been assessed (recirculation, incidence angle, global variables, etc.), in both low and high mass flow rates. The effective "nozzle" that appears when the recirculation constraints the incoming flow is less visible than in the straight duct, possibly influencing on the surge limit.
- Convergent-Divergent nozzle: less incoming momentum and recirculation values resulted from the simulation, but the lower interaction with the backflows reduced the enthalpy transfer and the friction losses, which implied a colder incoming flow and an increased compressor efficiency. The area restriction of the throat worsens the performance at high mass flow rates.
- Convergent nozzle: the effects found in the C-D nozzle are aggravated with this intake geometry. Nevertheless, in spite of having the lowest recirculation and momentum values, the swirl at the inducer plane produces the highest α and incidence values, increasing the stability at low mass flow rates. The incoming temperature is lower as well, producing an increase in efficiency. Drawbacks of this configuration appear when the mass flow rate increases and the pressure losses of the cross-section restriction counter-acts the aforementioned benefits.

Finally, concerning the noise analysis, it is concluded that the inlet geometry plays an important role on the characterization of the emitted spectra at low mass flow rates, not only setting the global intensity but also altering the noise signature, potentially impacting in the subjective perception of the complete engine noise, aspect that has grown in importance in the latter years. The outlet pressure waves are also influenced by the inlet geometry, so its study cannot be discarded beforehand for modeling the acoustic response of the whole gas exchange process of the engine. A slight noise reduction is found for the tapered and C-D nozzle and a significant reduction is produced by the convergent nozzle, due to the partial blockage of the inlet area.

Chapter 5 Bibliography

[51] E. Sundström, B. Semlitsch, and M. Mihăescu. "Generation Mechanisms of Rotating Stall and Surge in Centrifugal Compressors." *Flow, Turbulence and Combustion* 100(3) (2018), pp. 705–719. ISSN: 1573-1987. DOI: 10.1007/s10494-017-9877-z (cit. on pp. 9, 126, 136).

[57] J. Galindo, J. R. Serrano, X. Margot, A. Tiseira, N. Schorn, and H. Kindl. "Potential of flow pre-whirl at the compressor inlet of automotive engine turbochargers to enlarge surge margin and overcome packaging limitations." *International journal of heat and fluid flow* 28(3) (2007), pp. 374–387. DOI: 10.1016/j.ijheatfluidflow.2006.06.002 (cit. on pp. 9, 96, 128).

[58] R. Lang. "Contribución a la Mejora del Margen de Bombeo en Compresores Centrífugos de Sobrealimentación." PhD thesis. Universitat Politècnica de València, 2011 (cit. on pp. 9, 96, 104, 120, 147).

[59] J. Galindo, F. Arnau, A. Tiseira, R. Lang, H. Lahjaily, and T. Gimenes. "Measurement and Modeling of Compressor Surge on Engine Test Bench for Different Intake Line Configurations." *SAE Technical Paper* 2011-01-0370 (2011). DOI: 10.4271/2011-01-0370 (cit. on pp. 9, 10, 99, 125).

[60] J. Desantes, J. M. Luján, B Pla, and J. Soler. "Potential of using a nozzle at the compressor inlet of a high-speed direct-injection diesel engine." *Proceedings of the Institution of Mechanical Engineers, Part D: Journal of Automobile Engineering* 225(2) (2011), pp. 178–189. DOI: 10.1243/09544070JAUTO1429 (cit. on pp. 9, 104, 121, 125, 135, 148).

[65] A. Broatch, J. Galindo, R. Navarro, and J. García-Tíscar. "Methodology for experimental validation of a CFD model for predicting noise generation in centrifugal compressors." *International Journal of Heat and Fluid Flow* 50 (2014), pp. 134–144. DOI: 10.1016/j.ijheatfluidflow.2014.06.006 (cit. on pp. 10, 96, 120, 124).

[74] A. Broatch, J. Galindo, R. Navarro, and J. García-Tíscar. "Numerical and experimental analysis of automotive turbocharger compressor aeroacoustics at different operating conditions." *International Journal of Heat and Fluid Flow* 61 (2016), pp. 245 –255. ISSN: 0142-727X. DOI: 10.1016/j.ijheatfluidflow.2016.04.003 (cit. on pp. 11, 28, 70, 86, 122, 136).

[75] A. Broatch, J. Galindo, R. Navarro, J. García-Tíscar, A. Daglish, and R. K. Sharma. "Simulations and measurements of automotive turbocharger compressor whoosh noise." *Engineering Applications of Computational Fluid Mechanics* 9(1) (2015). DOI: 10.1080/19942060.2015.1004788 (cit. on pp. 11, 96, 122).

[76] A. J. Torregrosa, A. Broatch, R. Navarro, and J. García-Tíscar. "Acoustic characterization of automotive turbocompressors." *International Journal of Engine Research* 16(1) (2015), pp. 31–37. DOI: 10.1177/1468087414562866 (cit. on pp. 11, 98, 137).

[77] R. Navarro. *Predicting Flow-Induced Acoustics at Near-Stall Conditions in an Automotive Turbocharger Compressor: A Numerical Approach*. Springer, 2018. ISBN: 978-3-319-72248-1. DOI: 10.1007/978-3-319-72248-1 (cit. on pp. 11, 71, 73, 122, 123).

[79] *STAR-CCM+*. Release version 11.06.010. CD-adapco. 2016. URL: http://www.cd-adapco.com (cit. on pp. 12, 70, 72, 120, 122).

[114] F. Mendonça, O. Baris, and G. Capon. "Simulation of Radial Compressor Aeroacoustics using CFD." In: *Proceedings of ASME Turbo Expo 2012*. GT2012-70028. ASME. 2012, pp. 1823–1832. DOI: 10.1115/GT2012-70028 (cit. on pp. 71, 120, 122).

[116] B. Cabral and L. C. Leedom. "Imaging vector fields using line integral convolution." In: *Proceedings of the 20th annual conference on Computer graphics and interactive techniques*. ACM. 1993, pp. 263–270. DOI: 10.1145/166117.166151 (cit. on pp. 77, 130).

[125] E. Guillou, M. Gancedo, E. Gutmark, and A. Mohamed. "PIV investigation of the flow induced by a passive surge control method in a radial compressor." *Experiments in fluids* 53(3) (2012), pp. 619–635. DOI: 10.1007/s00348-012-1310-8 (cit. on pp. 97, 120).

[128] S.-B. Ma and K.-Y. Kim. "Optimization of discrete cavities in a centrifugal compressor to enhance operating stability." *Aerospace Science and Technology* 68 (2017), pp. 308 –319. ISSN: 1270-9638. DOI: 10.1016/j.ast.2017.05.029 (cit. on p. 120).

[129] J. Galindo, A. Tiseira, R. Navarro, and M. López. "Influence of tip clearance on flow behavior and noise generation of centrifugal compressors in near-surge conditions." *International Journal of Heat and Fluid Flow* 52 (2015), pp. 129–139. DOI: 10.1016/j.ijheatfluidflow.2014.12.004 (cit. on p. 122).

[130] A. Travin, M. Shur, M. Strelets, and P. Spalart. "Detached-eddy simulations past a circular cylinder." *Flow, Turbulence and Combustion* 63(1-4) (2000), pp. 293–313 (cit. on p. 122).

[131] S. Fontanesi, S. Paltrinieri, and G. Cantore. "CFD Analysis of the Acoustic Behavior of a Centrifugal Compressor for High Performance Engine Application." *Energy Procedia* 45(0) (2014). ATI 2013 - 68th Conference of the Italian Thermal Machines Engineering Association, pp. 759–768. DOI: 10.1016/j.egypro.2014.01.081 (cit. on p. 122).

[132] R. van Rennings, K. Shi, S. Fu, and F. Thiele. "Delayed-Detached-Eddy Simulation of Near-Stall Axial Compressor Flow with Varying Passage Numbers." In: *Progress in Hybrid RANS-LES Modelling*. Ed. by S. Fu, W. Haase, S.-H. Peng, and D. Schwamborn. Vol. 117. Notes on Numerical Fluid Mechanics and Multidisciplinary Design. Springer Berlin Heidelberg, 2012, pp. 439–448. ISBN: 978-3-642-31817-7. DOI: 10.1007/978-3-642-31818-4_38 (cit. on p. 122).

[133] A. J. Torregrosa, P. Fajardo, A. Gil, and R. Navarro. "Development of a non-reflecting boundary condition for application in 3D computational fluid dynamic codes." *Engineering Applications of Computational Fluid Mechanics* 6(3) (2012), pp. 447–460. DOI: 10.1080/19942060.2012.11015434 (cit. on p. 124).

[134] L. J. Eriksson. "Higher order mode effects in circular ducts and expansion chambers." *The Journal of the Acoustical Society of America* 68 (1980), p. 545. DOI: 10.1121/1.384768 (cit. on p. 124).

[135] P. Welch. "The use of fast Fourier transform for the estimation of power spectra: a method based on time averaging over short, modified periodograms." *Audio and Electroacoustics, IEEE Transactions on* 15(2) (1967), pp. 70–73 (cit. on p. 124).

[136] K. Holland and P. Davies. "The measurement of sound power flux in flow ducts." *Journal of Sound and Vibration* 230(4) (2000), pp. 915–932. DOI: 10.1006/jsvi.1999.2656 (cit. on p. 125).

[137] I. Tomita, B. An, and T. Nanbu. "A new operating range enhancement device combined with a casing treatment and inlet guide vanes for centrifugal compressors." In: *11th International Conference on Turbochargers and Turbocharging*. Ed. by I. o. M. Engineers. Oxford: Woodhead Publishing, 2014, pp. 79 –87. ISBN: 978-0-08-100033-5. DOI: 10.1533/978081000342.79 (cit. on p. 128).

[138] B. Semlitsch and M. Mihaescu. "Flow phenomena leading to surge in a centrifugal compressor." *Energy* 103 (2016), pp. 572 –587. ISSN: 0360-5442. DOI: 10.1016/j.energy.2016.03.032 (cit. on p. 128).

[139] D. Evans and A. Ward. "The reduction of turbocharger whoosh noise." In: 8^{th} *International Conference on Turbochargers and Turbocharging*. IMechE. 2006 (cit. on p. 136).

[140] E. P. Trochon. "A new type of silencers for turbocharger noise control." *SAE Technical Paper* 110(6) (2001), pp. 1587–1592. DOI: 10.4271/2001-01-1436 (cit. on p. 136).

[141] G. Gaudé, T. Lefèvre, R. Tanna, K. Jin, T. J. B. McKitterick, and S. Armenio. "Experimental and computational challenges in the quantification of turbocharger vibro-acoustic sources." In: *Proceedings of the 37th International Congress and Exposition on Noise Control Engineering 2008*. Vol. 2008. 3. Institute of Noise Control Engineering. 2008, pp. 5598–5611. ISBN: 978-1-60560-989-8 (cit. on p. 136).

[142] R. Kabral and M. Abom. "Investigation of turbocharger compressor surge inception by means of an acoustic two-port model." *Journal of Sound and Vibration* 412 (2018), pp. 270–286. ISSN: 0022-460X. DOI: 10.1016/j.jsv.2017.10.003 (cit. on p. 136).

Chapter 6

Concluding remarks

Contents

6.1 Introduction

A summary of the milestones and achievements made throughout this document are gathered in the current chapter. The main findings and contributions of the different performed studies are addressed in Section 6.2. Section 6.3 is devoted to the limitations of the proposed model, which affects the validity of the results obtained, and of the methodologies selected both for the experimental campaign and the simulation cases. Finally, improvement suggestion and potential applications of the condensation model, and possible further research on the exposed fields are covered in Section 6.4.

6.2 Summary of findings and contributions

6.2.1 Main original contributions

Developing this thesis implied the creation of new tools for better understanding the physical world and the attainment of remarkable conclusions from several studies, including both experimental tests and numerical simulations, which has modestly contributed, along with the effort of thousands of researchers, to the existent human knowledge. The highlighted contributions of the current document are presented next.

- A condensation model has been implemented in a commercial CFD code and validated against experimental data. The model considers the psychrometric state of the fluid, checking if over-saturation conditions of water vapor in dry air are given in any cells. If so, the amount of vapor that must condense in a given cell to return to a saturated state (RH=100%) is calculated. Due to the nature of the equations that control this phenomenon, the solution is implicit, so an iterative weighing equation as a function of the enthalpy is proposed for solving the condensed vapor. Then, custom source terms are defined for modifying the transport equations accordingly. A comparison between the condensation rate predicted in several configurations and the erosion found on the impeller after performing durability tests on the same geometries proved that the model provides consistent and meaningful information about the condensation capability of a given stream mixing geometry.

- Condensation simulation results of a parametric study of the intake flap angle in a LR-EGR T-joint showed a significant sensitivity of the mixing flow structures to the intake flap angle. A different study evidenced a high influence of the EGR rate (i.e., operating condition) on the mixing structures as well. Condensation rates found on these studies were correlated with the turbulence intensity of the flow structures, proving a direct relation between the LR-EGR T-joint and flap geometries and the operating conditions with the liquid water condensation.

- The impact of the compressor impeller on the mixing process and its consequent condensation is relatively low. Pressure perturbations generated by the presence of the rotating compressor wheel are not high enough to have a significant impact either on the flow structures or on the psychrometric conditions in charge of the condensation definition. Thus, simulating the T-joint without considering the compressor is admissible. Nevertheless, at very low mass flow rate operating conditions, for example in points similar to the one used in Chapter 5, the backflows that appear may, conversely, have a noticeable impact on these parameters, due to the important disruption of the main flow pattern. In any case, lower EGR rates are usually used under these conditions [117].

- The influence of the inlet geometry of the compressor on its performance has been assessed, highlighting the effect of different specific configurations:

  - Straight duct: this baseline inlet configuration produced the worst performance from the point of view of surge margin, going into deep surge during the transient tests more often that the rest of the configurations. The isentropic efficiency on the operating points near surge showed to be the lowest as well.
  - Tapered duct: as well as other researchers found [58], this configuration shifted the surge limit toward lower mass flow rates an average value of about ∼13%. The efficiency on the complete compressor map slightly increased respect to the baseline configuration and did not introduce pressure losses at very high mass flow rates. During the transient tests, surge occurred less, the surge cycles were noticeably reduced and the recovery time improved. However, a subtle increase in noise emission was measured at the intake orifice.
  - Convergent-Divergent nozzle: an average surge shift of ∼16% was

obtained with this nozzle. Analogously to the results obtained by Desantes et al. [60], a generalized efficiency improvement was measured across all the compressor map but the performance at very high mass flow rates slightly decreased, due to the pressure losses introduced by the throat restriction. Surge occurrence significantly decreased during the transient tests. The recovery time of deep surge remained the same but the pressure gradient of the oscillations decreased, implying a reduced axial loads over the compressor wheel.

- Convergent nozzle: this geometry resulted interesting as concept but impractical due to the dramatic performance loss at mid and high mass flow rates. The presence of the throat very close to the compressor nut restricted even more the available area, producing high pressure losses. Nevertheless, the most tilted surge line was obtained with this nozzle, resulted in about a ∼20% increase of surge margin. Additionally, noise emission also decreased.

- 3D-CFD simulations of very low mass flow rates using geometries similar to the experimentally tested in Chapter 4 provided meaningful information regarding the flow structures differences generated in each one and their implications. Additional points at very high mass flow rate were simulated to compare the performance under these conditions. Next are listed the most remarkable conclusions:

  - Straight duct: recirculating backflows appeared and traveled far upstream, due to the absence of any geometrical restriction. This backflows interacted with the incoming flow, transferring swirl and enthalpy to it and increasing friction losses, which translates into a reference efficiency that will be lower than other configurations. An interesting consequence of the backflows is the generation of an effective "nozzle" that constraints the incoming flow and delays the onset of surge.
  - Tapered duct: the parameters extracted from this case were very similar to the baseline results, for both low and high mass flow rates. The "nozzle" effect observed in the baseline case is also present but less visible.
  - Convergent-Divergent nozzle: the backflows were confined between the throat and the inducer, showing a decreased enthalpy transfer

(and friction) to the incoming flow, which was detected in a lower incoming temperature and a higher efficiency. Similarly found during the experimental campaign, at high mass flow rates the presence of the throat is noticed in the worse performance and lower compression ratio.

  - Convergent nozzle: the confinement in this case is tightened to a reduced region very close to the impeller, amplifying the effects found on the C-D nozzle. Nevertheless, the confinement also produced an increase of the tangential component, resulting in the highest α angle incidence among all the configurations, increasing the stability and delaying surge entrance. Friction losses are reduced as well, increasing the isentropic efficiency. Inevitably, at high mass flow rates the compression ratio and the efficiency drop, due to the presence of sonic flow conditions in the available cross-section left between the throat and the compressor nut.

- Concerning the noise emission assessment of the CFD simulations, it is concluded that the inlet geometry strongly impacts the acoustic signature at low mass flow rates, especially in the broad-band of frequencies related with the whoosh noise, i.e. between 0.05 and 0.5 RO. This is caused because the interaction between the backflows and the passing blades generate low pressure patterns, or bubbles, rotating at a lower rate than the impeller, which generate the aforementioned noise. The acoustic signature and the sound intensity have repercussions on both the subjective perception of the emitted noise, aspect that has been important recently, and also on the acoustic response of the gas exchange process, critical for designing the piping of the complete engine.

- As ultimate statement, it has been proved that the inlet geometry of the compressor affects, from one side, the condensation generation in case of making use of a LR-EGR system and thus, the durability of the turbocharger, and from the other side the efficiency, noise emission and especially the surge margin of the compressor.

6.2.2 Other findings

In addition to the main contributions, several methodological goals and side conclusions are described below:

- The proposed condensation model is based on the psychrometric state of the flow and interacts with the transport equations through a set of source terms, specifically built in STAR-CCM+®. However, porting this model to a different CFD software should be straightforward and easy, provided that the target CFD code is equipped with the required tools.

- Additionally to the implementation of the model itself, a set of field functions is also defined to allow a proper and meaningful processing of the condensation results.

- The model can be used along different turbulent models (RANS, DES) and time discretization (steady, transient).

- Since the model considers the psychrometric state of each cell, condensation mechanisms different to streams mixing condensation are also possible. A good example consists in condensation due to temperature drop caused by the acceleration of the flow, given in multiple confined flow applications, such as nozzles [143] or turbine stages [144]. However, the constraints of the model impose a velocity range validity at low values due to the supposition of instantaneous condensation, which would not be correct for moderate and high Mach numbers.

- Useful experimental techniques have been employed during the different testing campaigns, highlighting the compressor durability tests that were possible thanks to the usage of water injection in a hot stream to simulate EGR conditions, removing the necessity of generating real exhaust gases [41]. Tip-out tests for characterizing real surge onset [145] and intake manifold air injection to measure the compressor map [61] on an engine test bench also provided representative parameters to categorize the influence of each inlet geometry.

- A side benefit of being able to neglect the effect of the compressor on the mixing process is the possibility of not having to simulate both elements, especially considering the computational effort it implies. The total time required for a T-joint simulation is reduced in two orders of magnitude, passing from several weeks to about 6 hours.

- The uncertainty in condensation rate caused by the simplification of imposing a constant pressure as outlet boundary condition in the T-joint simulation in found below 3%.

- The aforementioned conclusion concerning the possibility of decoupling the LR-EGR from the compressor can also be applied to the experimental field. If the compressor is not placed a the outlet of the T-joint in a test bench, the access to different measurement techniques become possible, such as measurements of local flow velocity, temperature or even humidity. Laser techniques, such as PIV [146, 147, 148] or LDV [149, 150], widely used by different researchers, may also be used in this case, providing information enough to fully characterize the flow pattern and the condensation evolution.
- When the mass flow rate through the compressor decreases enough, backflows from the compressor naturally recirculate upstream of the impeller, contributing to stabilize the flow structures and delaying the surge onset. A small contribution to understand this phenomenon has been made in this thesis, however further studies and insights would allow taking advantage of it for improving the compressor performance and the engine features as well.

6.3 Limitations

The objectives introduced in Chapter 1 have been successfully achieved, however the limitations imposed during the implementation of the model, the experimental measurements and the numerical simulations need to be stated.

- It was required to develop a condensation model that introduced as low computational effort as possible. For achieving this, simplifications and assumptions were made, such as instantaneous condensation, neglecting the consideration of liquid water, making use of a passive scalar to track condensed vapor instead, etc. The reader may refer to Section 2.4 for a complete description of the hypothesis made. As already discussed, there are certain applications at which these assumptions do not hold (highly compressible flow at C-D nozzles, etc.)
- The field functions proposed for solving the psychrometry and the condensation source terms may not work as intended if directly ported to a different 3D-CFD code. A subsequent verification process should be carried (see Section 2.4) to check whether the particular implementation of the condensation submodel is behaving as intended or not.

- The experimental tests and the measurement techniques present uncertainties that have to be considered, as well as the results from the numerical simulations, which have to be carefully interpreted. To limit the latter, though, sensitivity studies (Section 2.5.2) have addressed the error for the most important parameters (mesh, time step, etc.).
- The inlet configuration simulation campaign was carried out using a single compressor geometry, so conclusions may only apply to that specific case. Moreover, this compressor model does not correspond with the turbocharger used in the experimental analysis. Both compressors share most of their features, though.
- Only simple compressor inlet geometries that are easy to build were considered during the selection. Besides, these were not even refined for optimum surge margin improvements, results of surge margin improvements should be considered accordingly.
- Only two mass flow rate points on the same iso-speed line have been simulated, thus, phenomena observed may be closely related to those specific solutions. The same compressor outlet pressure was imposed for all the cases, so corrected mass flow values are not completely identical, besides for the low mass flow rates the error is negligible, due to similar compression ratio obtained. Simulating the same corrected conditions would have required an iterative process, which would have added an excessive computational time.
- The comparison between the experimental tests with the numerical simulations concerning the influence of the compressor inlet are not conclusive in terms of surge limit, this is, simulations were not run until surge onset.

6.4 Suggestions for future studies

Like branches in a tree, each new scientific contribution offers the possibility of deepen on the topic through several ways. Below, a brief list of different suggestions for future studies is offered.

- Improving the model: Enhancing the realism of the model is potentially endless, being only limited by the desired complexity of the physical

equations involved. However, sticking to the current low computational effort approach, the author proposes to define a probabilistic distribution of the size and quantity of the droplets with a set of coefficients that would propagate and evolve along the flow to simulate phenomena such atomization and coalescence.

- Different condensation models may be explored. For instance, with a Lagrangian multiphase approach, modeling droplet evolution (coalescence) and impact on surfaces (damage or stress) may be feasible. Water droplet transport through the walls may be considered as well.

- Thanks to the possibility of decoupling the compressor from the T-joint without impacting on the mixing and condensation processes, characterizing the flow would be possible, including droplet assessment, as stated in Section 6.2.2. Experimental campaigns with different operating conditions and T-joint geometries would allow validating and adjusting the improved model exposed in the previous point.

- Other effects neglected for exceeding the scope of this application may be added, such as evaporation, condensation on surfaces or possible icing.

- A comparison could be made between the amount of condensates produced in LR-EGR T-joints due to mixing and other sources of condensation upstream the compressor, such as the one produced in the EGR cooler during engine warm-up.

- A simple compressor model would be required for accurately predicting the outlet pressure of the T-joint. Experimental data would be used for adjusting and validating this model.

- Simulations with different mass flow rates and compressor speeds would be meaningful to further characterizing the flow and assess the exposed intake geometries. Specifically, progressively lowering the mass flow rate until surge onset would offer valuable information, and points of maximum compressor efficiency would shed light about actual potentiality of using these geometries.

- The impact of in-flow condensation on 0D-1D gas-dynamic engine codes could be included.

- The impact of the EGR flow on the compressor could be assessed: the heterogeneity of the mixed flow through the compressor channels may

cause high temperature peaks that would not be present in an homogeneous mixed flow. The influence of the EGR on the surge line and the compressor parameters could also be analyzed using an analogous approach as performed in Chapter 5, stablishing a parametric campaign with different conditions of EGR rate and compressor operating points.

- An optimal design of the LR-EGR T-joint could be addressed, minimizing condensation production for a wide range of operating conditions and at the same time improving the compressor performance, i.e., shifting the surge line for a low-end torque enhance without worsening the behavior at high mass flow rates.

Chapter 6 Bibliography

[41] J. R. Serrano, P. Piqueras, E. Angiolini, C. Meano, and J. De La Morena. "On Cooler and Mixing Condensation Phenomena in the Long-Route Exhaust Gas Recirculation Line." In: *SAE Technical Paper*. 2015. DOI: 10.4271/2015-24-2521 (cit. on pp. 8, 10, 28, 32, 41, 54, 150).

[58] R. Lang. "Contribución a la Mejora del Margen de Bombeo en Compresores Centrífugos de Sobrealimentación." PhD thesis. Universitat Politècnica de València, 2011 (cit. on pp. 9, 96, 104, 120, 147).

[60] J. Desantes, J. M. Luján, B Pla, and J. Soler. "Potential of using a nozzle at the compressor inlet of a high-speed direct-injection diesel engine." *Proceedings of the Institution of Mechanical Engineers, Part D: Journal of Automobile Engineering* 225(2) (2011), pp. 178–189. DOI: 10.1243/09544070JAUTO1429 (cit. on pp. 9, 104, 121, 125, 135, 148).

[61] J. Galindo, A. Tiseira, F. J. Arnau, and R. Lang. "On-Engine Measurement of Turbocharger Surge Limit." *Experimental Techniques* 37(1) (2013), pp. 47–54. ISSN: 1747-1567. DOI: 10.1111/j.1747-1567.2010.00697.x (cit. on pp. 9, 10, 99, 150).

[117] Q. Zhang, M. Li, G. Li, S. Shao, and P. Li. "Transient emission characteristics of a heavy-duty natural gas engine at stoichiometric operation with EGR and TWC." *Energy* 132 (2017), pp. 225 –237. ISSN: 0360-5442. DOI: 10.1016/j.energy.2017.05.039 (cit. on pp. 82, 86, 147).

[143] C. Wang, L. Wang, H. Zhao, Z. Du, and Z. Ding. "Effects of superheated steam on non-equilibrium condensation in ejector primary nozzle." *International Journal of Refrigeration* 67 (2016), pp. 214 –226. ISSN: 0140-7007. DOI: 10.1016/j.ijrefrig.2016.02.022 (cit. on p. 150).

[144] I. Roumeliotis and K. Mathioudakis. "Analysis of moisture condensation during air expansion in turbines." *International Journal of Refrigeration* 29(7) (2006), pp. 1092 –1099. ISSN: 0140-7007. DOI: 10.1016/j.ijrefrig.2006.03.001 (cit. on p. 150).

[145] O. Leufvén and L. Eriksson. "A surge and choke capable compressor flow model – Validation and extrapolation capability." *Control Engineering Practice* 21(12) (2013), pp. 1871 –1883. ISSN: 0967-0661. DOI: 10.1016/j.conengprac.2013.07.005 (cit. on p. 150).

[146] X.-J. Yu and B.-J. Liu. "Stereoscopic PIV measurement of unsteady flows in an axial compressor stage." *Experimental Thermal and Fluid Science* 31(8) (2007), pp. 1049 –1060. ISSN: 0894-1777. DOI: 10.1016/j.expthermflusci.2006.11.001 (cit. on p. 151).

[147] S. K. Dahikar, M. J. Sathe, and J. B. Joshi. "Investigation of flow and temperature patterns in direct contact condensation using PIV, PLIF and CFD." *Chemical Engineering Science* 65(16) (2010), pp. 4606 – 4620. ISSN: 0009-2509. DOI: 10.1016/j.ces.2010.05.004 (cit. on p. 151).

[148] C. Espinoza, M. Simmons, F. Alberini, O. Mihailova, D. Rothman, and A. Kowalski. "Flow studies in an in-line Silverson 150/250 high shear mixer using PIV." *Chemical Engineering Research and Design* (2018). ISSN: 0263-8762. DOI: 10.1016/j.cherd.2018.01.028 (cit. on p. 151).

[149] A. Darisse, J. Lemay, and A. Benaïssa. "Investigation of passive scalar mixing in a turbulent free jet using simultaneous LDV and cold wire measurements." *International Journal of Heat and Fluid Flow* 44 (2013), pp. 284 –292. ISSN: 0142-727X. DOI: 10.1016/j.ijheatfluidflow.2013.06.012 (cit. on p. 151).

[150] A. Mychkovsky, D. Rangarajan, and S. Ceccio. "LDV measurements and analysis of gas and particulate phase velocity profiles in a vertical jet plume in a 2D bubbling fluidized bed: Part I: A two-phase LDV measurement technique." *Powder Technology* 220 (2012). Selected Papers from the 2010 NETL Multiphase Flow Workshop, pp. 55 –62. ISSN: 0032-5910. DOI: 10.1016/j.powtec.2011.09.027 (cit. on p. 151).

Global bibliography

[1] J. R. Serrano, P. Piqueras, R. Navarro, D. Tarí, and C. M. Meano. "Development and verification of an in-flow water condensation model for 3D-CFD simulations of humid air streams mixing." *Computers & Fluids* 167 (2018), pp. 158 –165. ISSN: 0045-7930. DOI: 10.1016/j.compfluid.2018.02.032 (cit. on p. x).

[2] J. Galindo, P. Piqueras, R. Navarro, D. Tarí, and C. M. Meano. "Validation and sensitivity analysis of an in-flow water condensation model for 3D-CFD simulations of humid air streams mixing." *Manuscript submitted to scientific journal* (2018) (cit. on p. x).

[3] J. Galindo, R. Navarro, D. Tarí, and G. García. "Centrifugal compressor influence on condensation due to Long Route-Exhaust Gas Recirculation mixing." *Manuscript submitted to scientific journal* (2018) (cit. on p. x).

[4] J. Galindo, A. Tiseira, R. Navarro, D. Tarí, and C. M. Meano. "Effect of the inlet geometry on performance, surge margin and noise emission of an automotive turbocharger compressor." *Applied Thermal Engineering* 110 (2017), pp. 875–882. DOI: 10.1016/j.applthermaleng.2016.08.099 (cit. on p. x).

[5] J. Galindo, A. Gil, R. Navarro, and D. Tarí. "Analysis of the impact of the geometry on the performance of an automotive centrifugal compressor using CFD simulations." *Manuscript submitted to scientific journal* (2018) (cit. on p. x).

[6] J. Galindo, R. Navarro, L. M. García-Cuevas, D. Tarí, H. Tartoussi, and S. Guilain. "A zonal approach for estimating pressure ratio at compressor extreme off-design conditions." *International Journal of*

Engine Research (2018). DOI: 10.1177/1468087418754899 (cit. on p. xi).

[7] J. Galindo, A. Tiseira, R. Navarro, D. Tarí, H. Tartoussi, and S. Guilain. "Compressor Efficiency Extrapolation for 0D-1D Engine Simulations." In: *SAE Technical Paper*. SAE International, Apr. 2016. DOI: 10.4271/2016-01-0554 (cit. on p. xi).

[8] J. Galindo, R. Navarro, L. M. García-Cuevas, and D. Tarí. "An approach for extrapolating turbocharger compression ratio maps for engine simulations." In: *Mathematical modelling in engineering and human behaviour 2015*. Ed. by L. Jódar, L. Acedo, J. C. Cortés, and F. Pedroche. 2015 (cit. on p. xi).

[9] F. Millo, F. Mallamo, E. Pautasso, and G. Ganio Mego. "The Potential of Electric Exhaust Gas Turbocharging for HD Diesel Engines." In: *SAE 2006 World Congress & Exhibition*. SAE International, 2006. DOI: 10.4271/2006-01-0437 (cit. on p. 3).

[10] D. Evans and A. Ward. "Minimizing Turbocharger Whoosh Noise for Diesel Powertrains." *SAE Technical Paper* 2005-01-2485 (2005). DOI: 10.4271/2005-01-2485 (cit. on pp. 3, 11, 96).

[11] Q. Yang, L. Li, Y. Zhao, J. Xiao, Y. Shu, and Q. Zhang. "Experimental investigation of an active control casing treatment of centrifugal compressors." *Experimental Thermal and Fluid Science* 83 (2017), pp. 107 – 117. ISSN: 0894-1777. DOI: 10.1016/j.expthermflusci.2016.12.013 (cit. on p. 3).

[12] M. Gancedo, E. Guillou, and E. Gutmark. "Effect of bleed slots on turbocharger centrifugal compressor stability." *International Journal of Heat and Fluid Flow* 70 (2018), pp. 206 –215. ISSN: 0142-727X. DOI: 10.1016/j.ijheatfluidflow.2017.12.007 (cit. on p. 3).

[13] J. S. Gaffney and N. A. Marley. "The impacts of combustion emissions on air quality and climate - From coal to biofuels and beyond." *Atmospheric Environment* 43(1) (2009). Atmospheric Environment - Fifty Years of Endeavour, pp. 23 –36. ISSN: 1352-2310. DOI: 10.1016/j.atmosenv.2008.09.016 (cit. on p. 4).

[14] J. E. Kirwan, M. Shost, G. Roth, and J. Zizelman. "3-Cylinder Turbocharged Gasoline Direct Injection: A High Value Solution for Low CO2 and NOx Emissions." *SAE International Journal of Engines* 3(1) (2010), pp. 355–371. DOI: 10.4271/2010-01-0590 (cit. on p. 4).

[15] P. Michel, A. Charlet, G. Colin, Y. Chamaillard, G. Bloch, and C. Nouillant. "Optimizing fuel consumption and pollutant emissions of gasoline-HEV with catalytic converter." *Control Engineering Practice* 61 (2017), pp. 198 –205. ISSN: 0967-0661. DOI: 10.1016/j.conengprac.2015.12.010 (cit. on p. 4).

[16] J. R. Serrano, H. Climent, P. Piqueras, and E. Angiolini. "Filtration modelling in wall-flow particulate filters of low soot penetration thickness." *Energy* 112 (2016), pp. 883 –898. ISSN: 0360-5442. DOI: 10.1016/j.energy.2016.06.121 (cit. on p. 4).

[17] B. Guan, R. Zhan, H. Lin, and Z. Huang. "Review of state of the art technologies of selective catalytic reduction of NOx from diesel engine exhaust." *Applied Thermal Engineering* 66(1) (2014), pp. 395 –414. ISSN: 1359-4311. DOI: 10.1016/j.applthermaleng.2014.02.021 (cit. on p. 4).

[18] Petersen Publishing Company and E. Rosen. *The Petersen Automotive Troubleshooting & Repair Manual*. Grosset & Dunlap, 1975. ISBN: 9780448119465 (cit. on p. 4).

[19] A. Cairns, N. Fraser, and H. Blaxill. "Pre versus post compressor supply of cooled EGR for full load fuel economy in turbocharged gasoline engines." In: *SAE Technical Paper*. 2008. DOI: 10.4271/2008-01-0425 (cit. on pp. 4, 27).

[20] J. M. Luján, H. Climent, R. Novella, and M. E. Rivas-Perea. "Influence of a low pressure EGR loop on a gasoline turbocharged direct injection engine." *Applied Thermal Engineering* 89 (2015), pp. 432–443. DOI: 10.1016/j.applthermaleng.2015.06.039 (cit. on pp. 4, 27).

[21] J. M. Desantes, J. M. Luján, B. Pla, and J. A. Soler. "On the combination of high-pressure and low-pressure exhaust gas recirculation loops for improved fuel economy and reduced emissions in high-speed direct-injection engines." *International Journal of Engine Research* 14(1) (2013), pp. 3–11. DOI: 10.1177/1468087412437623 (cit. on p. 5).

[22] N. Ladommatos, S. Abdelhalim, and H. Zhao. "The effects of exhaust gas recirculation on diesel combustion and emissions." *International Journal of Engine Research* 1(1) (2000), pp. 107–126. DOI: 10.1243/1468087001545290 (cit. on p. 5).

[23] L. Cornolti, A. Onorati, T. Cerri, G. Montenegro, and F. Piscaglia. "1D simulation of a turbocharged Diesel engine with comparison of short and long EGR route solutions." *Applied Energy* 111 (2013), pp. 1–15. DOI: 10.1016/j.apenergy.2013.04.016 (cit. on p. 5).

[24] J. Luján, B Pla, S Moroz, and G Bourgoin. "Effect of low pressure EGR on gas exchange processes and turbocharging of a HSDI engine." In: *Proceedings of the conference on thermo-and fluid-dynamic processes in diesel engines (THIESEL 2008), Valencia, Spain, paper E.* Vol. 2. 2008 (cit. on p. 5).

[25] J. M. Luján, J. Galindo, J. R. Serrano, and B. Pla. "A methodology to identify the intake charge cylinder-to-cylinder distribution in turbocharged direct injection Diesel engines." *Measurement Science and Technology* 19(6) (2008), p. 065401. DOI: 10.1088/0957-0233/19/6/065401 (cit. on p. 5).

[26] A. Maiboom, X. Tauzia, and J.-F. Hétet. "Influence of EGR unequal distribution from cylinder to cylinder on NOx–PM trade-off of a HSDI automotive Diesel engine." *Applied Thermal Engineering* 29(10) (2009), pp. 2043 –2050. ISSN: 1359-4311. DOI: 10.1016/j.applthermaleng.2008.10.017 (cit. on p. 5).

[27] J. Benajes, J. R. Serrano, S. Molina, and R. Novella. "Potential of Atkinson cycle combined with EGR for pollutant control in a HD diesel engine." *Energy Conversion and Management* 50(1) (2009), pp. 174 – 183. ISSN: 0196-8904. DOI: 10.1016/j.enconman.2008.08.034 (cit. on p. 5).

[28] J. R. Serrano, X. Margot, A. Tiseira, and L. M. García-Cuevas. "Optimization of the inlet air line of an automotive turbocharger." *International Journal of Engine Research* 14(1) (2013), pp. 92–104. DOI: 10.1177/1468087412449085 (cit. on pp. 6, 9, 28, 96).

[29] Dirección General de Tráfico. Gobierno de España. *Vehicles in operation in Spain.* 2016. URL: https://sedeapl.dgt.gob.es (cit. on pp. 6, 7).

[30] S. J. Kim and H. C. No. "Turbulent film condensation of high pressure steam in a vertical tube." *International Journal of Heat and Mass Transfer* 43(21) (2000), pp. 4031–4042. DOI: 10.1016/S0017-9310(00)00015-6 (cit. on pp. 8, 28).

[31] P. Panday. "Two-dimensional turbulent film condensation of vapours flowing inside a vertical tube and between parallel plates: a numerical approach." *International journal of refrigeration* 26(4) (2003), pp. 492–503. DOI: 10.1016/S0140-7007(02)00162-7 (cit. on pp. 8, 28).

[32] J. Liu, H. Aizawa, and H. Yoshino. "CFD prediction of surface condensation on walls and its experimental validation." *Building and Environment* 39(8) (2004), pp. 905–911. DOI: 10.1016/j.buildenv.2004.01.015 (cit. on pp. 8, 28).

[33] L. Vyskocil, J. Schmid, and J. Macek. "CFD simulation of air–steam flow with condensation." *Nuclear Engineering and Design* 279 (2014), pp. 147–157. DOI: 10.1016/j.nucengdes.2014.02.014 (cit. on pp. 8, 28, 31, 70).

[34] D.-Y. Shang and L.-C. Zhong. "Extensive study on laminar free film condensation from vapor–gas mixture." *International Journal of Heat and Mass Transfer* 51(17) (2008), pp. 4300–4314. DOI: 10.1016/j.ijheatmasstransfer.2008.03.004 (cit. on pp. 8, 28).

[35] C. Moses and G. Stein. "On the growth of steam droplets formed in a Laval nozzle using both static pressure and light scattering measurements." *Journal of Fluids Engineering* 100(3) (1978), pp. 311–322. DOI: 10.1115/1.3448672 (cit. on pp. 8, 28, 70).

[36] M. Grubel, J. Starzmann, M. Schatz, T. Eberle, and D. Vogt. "Two-phase flow modeling and measurements in low-pressure turbines-Part 1: Numerical validation of wet steam models and turbine modeling." In: 2014. DOI: 10.1115/GT2014-25244 (cit. on pp. 8, 28).

[37] M. Abarham, T. Chafekar, J. Hoard, D. Styles, and D. Assanis. "A visualization test setup for investigation of water-deposit interaction in a surrogate rectangular cooler exposed to diesel exhaust flow." *SAE Technical Paper* 2012-01-0364 (2012). DOI: 10.4271/2012-01-0364 (cit. on pp. 8, 28).

[38] A. Warey, A. S. Bika, D. Long, S. Balestrino, and P. Szymkowicz. "Influence of water vapor condensation on exhaust gas recirculation cooler fouling." *International Journal of Heat and Mass Transfer* 65 (2013), pp. 807–816. DOI: 10.1016/j.ijheatmasstransfer.2013.06.063 (cit. on pp. 8, 28).

[39] G. Bourgoin, E. Tomas, J. Luján, and B. Pla. "Acidic Condensation in HP EGR Systems Cooled at Low Temperature Using Diesel and Biodiesel Fuels." *SAE Technical Paper* 2010-01-1530 (2010). DOI: 10.4271/2010-01-1530 (cit. on pp. 8, 28).

[40] S. Moroz, G. Bourgoin, J. M. Luján, and B. Pla. "Acidic condensation in low pressure EGR systems using diesel and biodiesel fuels." *SAE Int. J. Fuels Lubr* 2009-01-2805 (2009). DOI: 10.4271/2009-01-2805 (cit. on pp. 8, 28).

[41] J. R. Serrano, P. Piqueras, E. Angiolini, C. Meano, and J. De La Morena. "On Cooler and Mixing Condensation Phenomena in the Long-Route Exhaust Gas Recirculation Line." In: *SAE Technical Paper*. 2015. DOI: 10.4271/2015-24-2521 (cit. on pp. 8, 10, 28, 32, 41, 54, 150).

[42] A. Castorrini, A. Corsini, F. Rispoli, P. Venturini, K. Takizawa, and T. E. Tezduyar. "Computational analysis of wind-turbine blade rain erosion." *Computers & Fluids* 141(Supplement C) (2016), pp. 175 –183. ISSN: 0045-7930. DOI: 10.1016/j.compfluid.2016.08.013 (cit. on pp. 8, 28).

[43] P. Z. John, T. Koka, and S. Dayalan. "Water droplet erosion simulation of a turbocharger compressor wheel." In: *ASME Turbo Expo 2014: Turbine Technical Conference and Exposition*. GT2014-26974. American Society of Mechanical Engineers. 2014 (cit. on pp. 8, 28).

[44] A. Surendran and H. D. Kim. "Effects of Wet Compression on the Flow Behavior of a Centrifugal Compressor: A CFD Analysis." In: *ASME Turbo Expo 2014: Turbine Technical Conference and Exposition*. GT2014-25035. American Society of Mechanical Engineers. 2014, V02DT42A002. DOI: 10.1115/GT2014-25035 (cit. on pp. 8, 28).

[45] E. M. Greitzer. "Surge and rotating stall in axial flow compressors–Part I: Theoretical compression system model." *Journal of Engineering for Gas Turbines and Power* 98(2) (1976), pp. 190–198. DOI: 10.1115/1.3446138 (cit. on pp. 8, 95).

[46] M. C. Huppert. *Compressor surge*. Tech. rep. 1965 (cit. on pp. 8, 96).

[47] D. Fink, N. Cumpsty, and E. Greitzer. "Surge dynamics in a free-spool centrifugal compressor system." *Journal of Turbomachinery* 114(2) (1992), pp. 321–332. DOI: 10.1115/91-GT-031 (cit. on pp. 8, 96).

[48] F. Willems and B. De Jager. "Modeling and control of compressor flow instabilities." *Control Systems, IEEE* 19(5) (1999), pp. 8–18. DOI: 10.1109/37.793434 (cit. on pp. 8, 96).

[49] A. Epstein, J. Ffowcs Williams, and E. Greitzer. "Active suppression of aerodynamic instabilities in turbomachines." *Journal of Propulsion and Power* 5(2) (1989), pp. 204–211. DOI: 10.2514/3.23137 (cit. on pp. 8, 96).

[50] J. T. Gravdahl, O. Egeland, and S. O. Vatland. "Drive torque actuation in active surge control of centrifugal compressors." *Automatica* 38(11) (2002), pp. 1881–1893. DOI: 10.1016/S0005-1098(02)00113-9 (cit. on pp. 8, 96).

[51] E. Sundström, B. Semlitsch, and M. Mihăescu. "Generation Mechanisms of Rotating Stall and Surge in Centrifugal Compressors." *Flow, Turbulence and Combustion* 100(3) (2018), pp. 705–719. ISSN: 1573-1987. DOI: 10.1007/s10494-017-9877-z (cit. on pp. 9, 126, 136).

[52] A. Zamiri, B. J. Lee, and J. T. Chung. "Numerical evaluation of transient flow characteristics in a transonic centrifugal compressor with vaned diffuser." *Aerospace Science and Technology* 70 (2017), pp. 244 –256. ISSN: 1270-9638. DOI: 10.1016/j.ast.2017.08.003 (cit. on p. 9).

[53] I. Shahin, M. Alqaradawi, M. Gadala, and O. Badr. "Large eddy simulation of surge inception and active surge control in a high speed centrifugal compressor with a vaned diffuser." *Applied Mathematical Modelling* 40(23) (2016), pp. 10404 –10418. ISSN: 0307-904X. DOI: 10.1016/j.apm.2016.07.030 (cit. on p. 9).

[54] I. Ariga, N. Kasai, S. Masuda, Y. Watanabe, and I. Watanabe. "The effect of inlet distortion on the performance characteristics of a centrifugal compressor." *Journal of Engineering for Gas Turbines and Power* 105(2) (1983), pp. 223–230. DOI: 10.1115/82-GT-92 (cit. on pp. 9, 96).

[55] G. Capon and T. Morris. "The effect of air inlet system features on automotive turbocharger compressor performance." In: 9^{th} *International Conference on Turbochargers and Turbocharging*. 2010 (cit. on pp. 9, 96).

[56] O. Baris and F. Mendonça. "Automotive Turbocharger Compressor CFD and Extension Towards Incorporating Installation Effects." In: *Proceedings of ASME Turbo Expo 2011: Power for Land, Sea and Air*. ASME, 2011, pp. 2197–2206. DOI: 10.1115/GT2011-46796 (cit. on pp. 9, 10, 96).

[57] J. Galindo, J. R. Serrano, X. Margot, A. Tiseira, N. Schorn, and H. Kindl. "Potential of flow pre-whirl at the compressor inlet of automotive engine turbochargers to enlarge surge margin and overcome packaging limitations." *International journal of heat and fluid flow* 28(3) (2007), pp. 374–387. DOI: 10.1016/j.ijheatfluidflow.2006.06.002 (cit. on pp. 9, 96, 128).

[58] R. Lang. "Contribución a la Mejora del Margen de Bombeo en Compresores Centrífugos de Sobrealimentación." PhD thesis. Universitat Politècnica de València, 2011 (cit. on pp. 9, 96, 104, 120, 147).

[59] J. Galindo, F. Arnau, A. Tiseira, R. Lang, H. Lahjaily, and T. Gimenes. "Measurement and Modeling of Compressor Surge on Engine Test Bench for Different Intake Line Configurations." *SAE Technical Paper* 2011-01-0370 (2011). DOI: 10.4271/2011-01-0370 (cit. on pp. 9, 10, 99, 125).

[60] J. Desantes, J. M. Luján, B Pla, and J. Soler. "Potential of using a nozzle at the compressor inlet of a high-speed direct-injection diesel engine." *Proceedings of the Institution of Mechanical Engineers, Part D: Journal of Automobile Engineering* 225(2) (2011), pp. 178–189. DOI: 10.1243/09544070JAUTO1429 (cit. on pp. 9, 104, 121, 125, 135, 148).

[61] J. Galindo, A. Tiseira, F. J. Arnau, and R. Lang. "On-Engine Measurement of Turbocharger Surge Limit." *Experimental Techniques* 37(1) (2013), pp. 47–54. ISSN: 1747-1567. DOI: 10.1111/j.1747-1567.2010.00697.x (cit. on pp. 9, 10, 99, 150).

[62] J. Luján, V. Bermúdez, J. R. Serrano, and C. Cervelló. "Test bench for turbocharger groups characterization." *SAE Technical Paper* 2002-01-0163 (2002). DOI: 10.4271/2002-01-0163 (cit. on pp. 9, 44, 96).

[63] M. Tancrez, J. Galindo, C. Guardiola, P. Fajardo, and O. Varnier. "Turbine adapted maps for turbocharger engine matching." *Experimental Thermal and Fluid Science* 35(1) (2011), pp. 146–153. DOI: 10.1016/j.expthermflusci.2010.07.018 (cit. on pp. 9, 44).

[64] J. Galindo, H. Climent, C. Guardiola, and A. Tiseira. "On the effect of pulsating flow on surge margin of small centrifugal compressors for automotive engines." *Experimental Thermal and Fluid Science* 33(8) (2009), pp. 1163–1171. DOI: 10.1016/j.expthermflusci.2009.07.006 (cit. on pp. 10, 96, 99).

[65] A. Broatch, J. Galindo, R. Navarro, and J. García-Tíscar. "Methodology for experimental validation of a CFD model for predicting noise generation in centrifugal compressors." *International Journal of Heat and Fluid Flow* 50 (2014), pp. 134–144. DOI: 10.1016/j.ijheatfluidflow.2014.06.006 (cit. on pp. 10, 96, 120, 124).

[66] A. J. Torregrosa, A. Broatch, X. Margot, and J. García-Tíscar. "Experimental methodology for turbocompressor in-duct noise evaluation based on beamforming wave decomposition." *Journal of Sound and Vibration* 376 (2016), pp. 60–71. DOI: 10.1016/j.jsv.2016.04.035 (cit. on p. 10).

[67] A. Sakowitz, M. Mihaescu, and L. Fuchs. "Turbulent flow mechanisms in mixing T-junctions by Large Eddy Simulations." *International Journal of Heat and Fluid Flow* 45 (2014), pp. 135–146. DOI: 10.1016/j.ijheatfluidflow.2013.06.014 (cit. on pp. 10, 29, 47).

[68] A. Sakowitz, M. Mihaescu, and L. Fuchs. "Effects of velocity ratio and inflow pulsations on the flow in a T-junction by Large Eddy Simulation." *Computers & Fluids* 88 (2013), pp. 374–385. ISSN: 0045-7930. DOI: 10.1016/j.compfluid.2013.10.001 (cit. on p. 10).

[69] A. Sakowitz, M. Mihaescu, and L. Fuchs. "Flow decomposition methods applied to the flow in an IC engine manifold." *Applied Thermal Engineering* 65(1–2) (2014), pp. 57–65. ISSN: 1359-4311. DOI: 10.1016/j.applthermaleng.2013.12.082 (cit. on p. 10).

[70] B. Semlitsch, V JyothishKumar, M. Mihaescu, L. Fuchs, E. Gutmark, and M. Gancedo. "Numerical Flow Analysis of a Centrifugal Compressor with Ported and without Ported Shroud." *SAE Technical Paper* 2014-01-1655 (2014). DOI: 10.4271/2014-01-1655 (cit. on p. 10).

[71] A. Karim, K. Miazgowicz, B. Lizotte, and A. Zouani. "Computational Aero-Acoustics Simulation of Compressor Whoosh Noise in Automotive Turbochargers." *SAE Technical Paper* 2013-01-1880 (2013). DOI: 10.4271/2013-01-1880 (cit. on pp. 11, 96).

[72] T. Raitor and W. Neise. "Sound generation in centrifugal compressors." *Journal of Sound and Vibration* 314 (2008), pp. 738–756. ISSN: 0022-460X. DOI: 10.1016/j.jsv.2008.01.034 (cit. on pp. 11, 97).

[73] C. Teng and S. Homco. "Investigation of Compressor Whoosh Noise in Automotive Turbochargers." *SAE Int. J. of Passeng. Cars-Mech. Syst.* 2(1) (2009), pp. 1345–1351. DOI: 10.4271/2009-01-2053 (cit. on pp. 11, 96).

[74] A. Broatch, J. Galindo, R. Navarro, and J. García-Tíscar. "Numerical and experimental analysis of automotive turbocharger compressor aeroacoustics at different operating conditions." *International Journal of Heat and Fluid Flow* 61 (2016), pp. 245 –255. ISSN: 0142-727X. DOI: 10.1016/j.ijheatfluidflow.2016.04.003 (cit. on pp. 11, 28, 70, 86, 122, 136).

[75] A. Broatch, J. Galindo, R. Navarro, J. García-Tíscar, A. Daglish, and R. K. Sharma. "Simulations and measurements of automotive turbocharger compressor whoosh noise." *Engineering Applications of Computational Fluid Mechanics* 9(1) (2015). DOI: 10.1080/19942060.2015.1004788 (cit. on pp. 11, 96, 122).

[76] A. J. Torregrosa, A. Broatch, R. Navarro, and J. García-Tíscar. "Acoustic characterization of automotive turbocompressors." *International Journal of Engine Research* 16(1) (2015), pp. 31–37. DOI: 10.1177/1468087414562866 (cit. on pp. 11, 98, 137).

[77] R. Navarro. *Predicting Flow-Induced Acoustics at Near-Stall Conditions in an Automotive Turbocharger Compressor: A Numerical Approach*. Springer, 2018. ISBN: 978-3-319-72248-1. DOI: 10.1007/978-3-319-72248-1 (cit. on pp. 11, 71, 73, 122, 123).

[78] *STAR-CCM+*. Release version 9.04.011. CD-adapco. 2014. URL: http://www.cd-adapco.com (cit. on pp. 12, 29, 30, 35, 36, 47, 60).

[79] *STAR-CCM+*. Release version 11.06.010. CD-adapco. 2016. URL: http://www.cd-adapco.com (cit. on pp. 12, 70, 72, 120, 122).

[80] M. Perić. "Acoustics and Turbulence: Aerodynamics Applications of STAR-CCM+." In: *South East Asian Conference*. 2012 (cit. on p. 12).

[81] F. Posada, A. Bandivadekar, and J. German. "Estimated cost of emission control technologies for light-duty vehicles Part 1-Gasoline." In: *SAE Technical Paper*. 2013. DOI: 10.4271/2013-01-0534 (cit. on p. 27).

[82] F. Posada, A. Bandivadekar, and J. German. "Estimated cost of emission control technologies for light-duty vehicles Part 2-Diesel." In: *SAE Technical Paper*. 2013. DOI: 10.4271/2013-01-0539 (cit. on p. 27).

[83] R. Mobasheri and Z. Peng. "CFD investigation into diesel fuel injection schemes with aid of Homogeneity Factor." *Computers & Fluids* 77(Supplement C) (2013), pp. 12 –23. ISSN: 0045-7930. DOI: 10.1016/j.compfluid.2013.02.013 (cit. on p. 27).

[84] J. M. Luján, H. Climent, V. Dolz, A. Moratal, J. Borges-Alejo, and Z. Soukeur. "Potential of exhaust heat recovery for intake charge heating in a diesel engine transient operation at cold conditions." *Applied Thermal Engineering* 105 (2016), pp. 501–508. DOI: 10.1016/j.applthermaleng.2016.03.028 (cit. on p. 27).

[85] T. V. Johnson. "Review of Vehicular Emissions Trends." *SAE Int. J. Engines* 8 (Apr. 2015), pp. 1152–1167. DOI: 10.4271/2015-01-0993 (cit. on p. 27).

[86] C. Guardiola, B. Pla, P. Piqueras, J. Mora, and D. Lefebvre. "Model-based passive and active diagnostics strategies for diesel oxidation catalysts." *Applied Thermal Engineering* 110 (2017), pp. 962–971. DOI: 10.1016/j.applthermaleng.2016.08.207 (cit. on p. 27).

[87] Y. Patel, T. Turunen-Saaresti, G. Patel, and A. Grönman. "Numerical investigation of turbulence modelling on condensing steam flows in turbine cascade." In: *ASME Turbo Expo 2014: Turbine Technical Conference and Exposition*. American Society of Mechanical Engineers. 2014, V01BT27A035–V01BT27A035 (cit. on pp. 29, 72).

[88] H. K. Versteeg and W. Malalasekera. *An introduction to computational fluid dynamics: the finite volume method*. 2nd ed. Harlow: Pearson Education Limited, 2007 (cit. on pp. 29, 40, 44).

[89] AIAA. *Guide for the Verification and Validation of Computational Fluid Dynamics Simulations*. Vol. G-077-1998. AIAA, 1998. DOI: 10.2514/4.472855.001 (cit. on p. 29).

[90] W. L. Oberkampf and T. G. Trucano. "Verification and validation in computational fluid dynamics." *Progress in Aerospace Sciences* 38(3) (2002), pp. 209–272. ISSN: 0376-0421. DOI: 10.1016/S0376-0421(02)00005-2 (cit. on p. 29).

[91] P. J. Roache. *Verification and validation in computational science and engineering*. Vol. 895. Hermosa Albuquerque, NM, 1998 (cit. on pp. 29, 40).

[92] S. P. Veluri, C. J. Roy, and E. A. Luke. "Comprehensive code verification techniques for finite volume CFD codes." *Computers & Fluids* 70(Supplement C) (2012), pp. 59 –72. ISSN: 0045-7930. DOI: 10.1016/j.compfluid.2012.04.028 (cit. on pp. 29, 40).

[93] S. Sen, M. Selokar, D. Nisad, and K. Kishore. "Design and Development of Demisting Device of a Commercial Vehicle and its Numerical as Well as Experimental Validation." In: *SAE Technical Paper*. 2016. DOI: 10.4271/2016-01-0217 (cit. on p. 30).

[94] *Psychrometric Chart - Structure and Application*. Siemens Building Technologies Group, 2014. URL: www.siemens.com (cit. on pp. 30, 32, 34).

[95] D. C. Shallcross. "Psychrometric charts for water vapour in natural gas." *Journal of Petroleum Science and Engineering* 61(1) (2008), pp. 1–8. DOI: 10.1016/j.petrol.2007.10.002 (cit. on pp. 30, 32, 34).

[96] M. J. Moran, H. N. Shapiro, D. D. Boettner, and M. B. Bailey. *Fundamentals of engineering thermodynamics*. John Wiley & Sons, 2010 (cit. on pp. 32, 86).

[97] G. Ferron and S. Soderholm. "Estimation of the evaporation or stabilization times of water droplets." *Journal of Aerosol Science* 18(6) (1987), pp. 639 –642. ISSN: 0021-8502. DOI: 10.1016/0021-8502(87)90086-3 (cit. on p. 34).

[98] H. Barrow and C. Pope. "Droplet evaporation with reference to the effectiveness of water-mist cooling." *Applied Energy* 84(4) (2007), pp. 404 –412. ISSN: 0306-2619. DOI: 10.1016/j.apenergy.2006.09.007 (cit. on p. 34).

[99] D. R. Stull. "Vapor pressure of pure substances. Organic and inorganic compounds." *Industrial & Engineering Chemistry* 39(4) (1947), pp. 517–540. DOI: 10.1021/ie50448a022 (cit. on p. 35).

[100] Y. Tominaga and T. Stathopoulos. "Turbulent Schmidt numbers for CFD analysis with various types of flowfield." *Atmospheric Environment* 41(37) (2007), pp. 8091 –8099. ISSN: 1352-2310. DOI: 10.1016/j.atmosenv.2007.06.054 (cit. on p. 39).

[101] D. C. Wilcox. "Reassessment of the scale-determining equation for advanced turbulence models." *AIAA journal* 26(11) (1988), pp. 1299–1310. DOI: 10.2514/3.10041 (cit. on p. 40).

[102] D. C. Wilcox. *Turbulence Modeling for CFD (Hardcover)*. 3rd ed. La Cañada, California: Dcw Industries Inc., 2006 (cit. on p. 47).

[103] W. Jones and B. Launder. "The prediction of laminarization with a two-equation model of turbulence." *International Journal of Heat and Mass Transfer* 15(2) (1972), pp. 301–314. DOI: 10.1016/0017-9310(72)90076-2 (cit. on p. 47).

[104] J. Costa, L. Oliveira, and D Blay. "Test of several versions for the k–ε type turbulence modelling of internal mixed convection flows." *International Journal of Heat and Mass Transfer* 42(23) (1999), pp. 4391–4409. DOI: 10.1016/S0017-9310(99)00075-7 (cit. on p. 47).

[105] Ferziger, J.H. and Perić, M. *Computational Methods for Fluid Dynamics*. 3rd rev. Berlin: Springer, 2002 (cit. on p. 48).

[106] J. M. Chen and Y.-C. Fang. "Strouhal numbers of inclined flat plates." *Journal of wind engineering and industrial aerodynamics* 61(2) (1996), pp. 99–112. DOI: 10.1016/0167-6105(96)00044-X (cit. on p. 51).

[107] F. R. Menter. "Two-equation eddy-viscosity turbulence models for engineering applications." *AIAA journal* 32(8) (1994), pp. 1598–1605. DOI: 10.2514/3.12149 (cit. on p. 52).

[108] A. Kuczaj, E. Komen, and M. Loginov. "Large-Eddy Simulation study of turbulent mixing in a T-junction." *Nuclear Engineering and Design* 240(9) (2010). Experiments and CFD Code Applications to Nuclear Reactor Safety (XCFD4NRS), pp. 2116 –2122. ISSN: 0029-5493. DOI: 10.1016/j.nucengdes.2009.11.027 (cit. on p. 70).

[109] C. Walker, A. Manera, B. Niceno, M. Simiano, and H.-M. Prasser. "Steady-state RANS-simulations of the mixing in a T-junction." *Nuclear Engineering and Design* 240(9) (2010). Experiments and CFD Code Applications to Nuclear Reactor Safety (XCFD4NRS), pp. 2107 –2115. ISSN: 0029-5493. DOI: 10.1016/j.nucengdes.2010.05.056 (cit. on p. 70).

[110] B. Smith, J. Mahaffy, and K. Angele. "A CFD benchmarking exercise based on flow mixing in a T-junction." *Nuclear Engineering and Design* 264 (2013). SI:NURETH-14, pp. 80 –88. ISSN: 0029-5493. DOI: 10.1016/j.nucengdes.2013.02.030 (cit. on p. 70).

[111] Y. Yang, J. H. Walther, Y. Yan, and C. Wen. "CFD modeling of condensation process of water vapor in supersonic flows." *Applied Thermal Engineering* 115 (2017), pp. 1357 –1362. ISSN: 1359-4311. DOI: 10.1016/j.applthermaleng.2017.01.047 (cit. on p. 70).

[112] A. Torregrosa, A. Broatch, X. Margot, J. García-Tíscar, Y. Narvekar, and R. Cheung. "Local flow measurements in a turbocharger compressor inlet." *Experimental Thermal and Fluid Science* 88 (2017), pp. 542 – 553. ISSN: 0894-1777. DOI: 10.1016/j.expthermflusci.2017.07.007 (cit. on p. 70).

[113] J. Andersen, F. Lindström, and F. Westin. "Surge definitions for radial compressors in automotive turbochargers." *SAE International Journal of Engines* 1(1) (2008), pp. 218–231. DOI: 10.4271/2008-01-0296 (cit. on p. 70).

[114] F. Mendonça, O. Baris, and G. Capon. "Simulation of Radial Compressor Aeroacoustics using CFD." In: *Proceedings of ASME Turbo Expo 2012*. GT2012-70028. ASME. 2012, pp. 1823–1832. DOI: 10.1115/GT2012-70028 (cit. on pp. 71, 120, 122).

[115] J. Galindo, A. Tiseira, P. Fajardo, and R. Navarro. "Analysis of the influence of different real flow effects on computational fluid dynamics boundary conditions based on the method of characteristics." *Mathematical and Computer Modelling* 57(7-8) (2013). Public Key Services and Infrastructures EUROPKI-2010-Mathematical Modelling in Engineering & Human Behaviour 2011, pp. 1957–1964. ISSN: 0895-7177. DOI: 10.1016/j.mcm.2012.01.016 (cit. on p. 73).

[116] B. Cabral and L. C. Leedom. "Imaging vector fields using line integral convolution." In: *Proceedings of the 20th annual conference on Computer graphics and interactive techniques*. ACM. 1993, pp. 263–270. DOI: 10.1145/166117.166151 (cit. on pp. 77, 130).

[117] Q. Zhang, M. Li, G. Li, S. Shao, and P. Li. "Transient emission characteristics of a heavy-duty natural gas engine at stoichiometric operation with EGR and TWC." *Energy* 132 (2017), pp. 225 –237. ISSN: 0360-5442. DOI: 10.1016/j.energy.2017.05.039 (cit. on pp. 82, 86, 147).

[118] J. Galindo, J. R. Serrano, C. Guardiola, and C. Cervelló. "Surge limit definition in a specific test bench for the characterization of automotive turbochargers." *Experimental Thermal and Fluid Science* 30(5) (2006),

pp. 449–462. DOI: 10.1016/j.expthermflusci.2005.06.002 (cit. on p. 95).

[119] B. de Jager. "Rotating stall and surge control: A survey." 2 (1995), pp. 1857–1862. DOI: 10.1109/CDC.1995.480612 (cit. on p. 96).

[120] D. L. Gysling, J Dugundji, E. Greitzer, and A. Epstein. "Dynamic control of centrifugal compressor surge using tailored structures." *Journal of Turbomachinery* 113(4) (1991), pp. 710–722. DOI: 10.1115/90-GT-122 (cit. on p. 96).

[121] A. Whitfield, A. Sutton, and H. Leonard. "The development of turbocharger compressors with improved surge margin." *ImechE C433/063* (1991), p. 9 (cit. on p. 96).

[122] A. Engeda, Y. Kim, R. Aungier, and G. Direnzi. "The inlet flow structure of a centrifugal compressor stage and its influence on the compressor performance." *Journal of fluids engineering* 125(5) (2003), pp. 779–785. DOI: 10.1115/1.1601255 (cit. on p. 96).

[123] R. C. Pampreen. *Compressor surge and stall*. Concepts Eti Vermont, 1993 (cit. on p. 96).

[124] E. Jenny. "Uber Instationnäire Vorgänge in Radialverdichtern Insbesondere in Aufladegruppen Von Verbrennungmotoren." *Schweiz. Bauztg* 79(46) (1961), pp. 802–817 (cit. on p. 96).

[125] E. Guillou, M. Gancedo, E. Gutmark, and A. Mohamed. "PIV investigation of the flow induced by a passive surge control method in a radial compressor." *Experiments in fluids* 53(3) (2012), pp. 619–635. DOI: 10.1007/s00348-012-1310-8 (cit. on pp. 97, 120).

[126] O. Leufvén and L. Eriksson. "Time to surge concept and surge control for acceleration performance." In: *Proceedings of the* 17^{th} *IFAC World Congress, 2008*. International Federation of Automatic Control (IFAC). 2008, pp. 2063–2068. DOI: 10.3182/20080706-5-KR-1001.00350 (cit. on p. 101).

[127] C.-H. Wang and C.-C. Wang. "Design and Implementation of Intelligent Surge Controller for Modern Turbo Charged Automobiles." *International Journal of Fuzzy Systems* 16(2) (2014), pp. 222–232 (cit. on p. 101).

[128] S.-B. Ma and K.-Y. Kim. "Optimization of discrete cavities in a centrifugal compressor to enhance operating stability." *Aerospace Science and Technology* 68 (2017), pp. 308 –319. ISSN: 1270-9638. DOI: 10.1016/j.ast.2017.05.029 (cit. on p. 120).

[129] J. Galindo, A. Tiseira, R. Navarro, and M. López. "Influence of tip clearance on flow behavior and noise generation of centrifugal compressors in near-surge conditions." *International Journal of Heat and Fluid Flow* 52 (2015), pp. 129–139. DOI: 10.1016/j.ijheatfluidflow.2014.12.004 (cit. on p. 122).

[130] A. Travin, M. Shur, M. Strelets, and P. Spalart. "Detached-eddy simulations past a circular cylinder." *Flow, Turbulence and Combustion* 63(1-4) (2000), pp. 293–313 (cit. on p. 122).

[131] S. Fontanesi, S. Paltrinieri, and G. Cantore. "CFD Analysis of the Acoustic Behavior of a Centrifugal Compressor for High Performance Engine Application." *Energy Procedia* 45(0) (2014). ATI 2013 - 68th Conference of the Italian Thermal Machines Engineering Association, pp. 759–768. DOI: 10.1016/j.egypro.2014.01.081 (cit. on p. 122).

[132] R. van Rennings, K. Shi, S. Fu, and F. Thiele. "Delayed-Detached-Eddy Simulation of Near-Stall Axial Compressor Flow with Varying Passage Numbers." In: *Progress in Hybrid RANS-LES Modelling*. Ed. by S. Fu, W. Haase, S.-H. Peng, and D. Schwamborn. Vol. 117. Notes on Numerical Fluid Mechanics and Multidisciplinary Design. Springer Berlin Heidelberg, 2012, pp. 439–448. ISBN: 978-3-642-31817-7. DOI: 10.1007/978-3-642-31818-4_38 (cit. on p. 122).

[133] A. J. Torregrosa, P. Fajardo, A. Gil, and R. Navarro. "Development of a non-reflecting boundary condition for application in 3D computational fluid dynamic codes." *Engineering Applications of Computational Fluid Mechanics* 6(3) (2012), pp. 447–460. DOI: 10.1080/19942060.2012.11015434 (cit. on p. 124).

[134] L. J. Eriksson. "Higher order mode effects in circular ducts and expansion chambers." *The Journal of the Acoustical Society of America* 68 (1980), p. 545. DOI: 10.1121/1.384768 (cit. on p. 124).

[135] P. Welch. "The use of fast Fourier transform for the estimation of power spectra: a method based on time averaging over short, modified periodograms." *Audio and Electroacoustics, IEEE Transactions on* 15(2) (1967), pp. 70–73 (cit. on p. 124).

[136] K. Holland and P. Davies. "The measurement of sound power flux in flow ducts." *Journal of Sound and Vibration* 230(4) (2000), pp. 915–932. DOI: 10.1006/jsvi.1999.2656 (cit. on p. 125).

[137] I. Tomita, B. An, and T. Nanbu. "A new operating range enhancement device combined with a casing treatment and inlet guide vanes for centrifugal compressors." In: *11th International Conference on Turbochargers and Turbocharging*. Ed. by I. o. M. Engineers. Oxford: Woodhead Publishing, 2014, pp. 79 –87. ISBN: 978-0-08-100033-5. DOI: 10.1533/978081000342.79 (cit. on p. 128).

[138] B. Semlitsch and M. Mihaescu. "Flow phenomena leading to surge in a centrifugal compressor." *Energy* 103 (2016), pp. 572 –587. ISSN: 0360-5442. DOI: 10.1016/j.energy.2016.03.032 (cit. on p. 128).

[139] D. Evans and A. Ward. "The reduction of turbocharger whoosh noise." In: 8^{th} *International Conference on Turbochargers and Turbocharging*. IMechE. 2006 (cit. on p. 136).

[140] E. P. Trochon. "A new type of silencers for turbocharger noise control." *SAE Technical Paper* 110(6) (2001), pp. 1587–1592. DOI: 10.4271/2001-01-1436 (cit. on p. 136).

[141] G. Gaudé, T. Lefèvre, R. Tanna, K. Jin, T. J. B. McKitterick, and S. Armenio. "Experimental and computational challenges in the quantification of turbocharger vibro-acoustic sources." In: *Proceedings of the 37th International Congress and Exposition on Noise Control Engineering 2008*. Vol. 2008. 3. Institute of Noise Control Engineering. 2008, pp. 5598–5611. ISBN: 978-1-60560-989-8 (cit. on p. 136).

[142] R. Kabral and M. Abom. "Investigation of turbocharger compressor surge inception by means of an acoustic two-port model." *Journal of Sound and Vibration* 412 (2018), pp. 270–286. ISSN: 0022-460X. DOI: 10.1016/j.jsv.2017.10.003 (cit. on p. 136).

[143] C. Wang, L. Wang, H. Zhao, Z. Du, and Z. Ding. "Effects of superheated steam on non-equilibrium condensation in ejector primary nozzle." *International Journal of Refrigeration* 67 (2016), pp. 214 –226. ISSN: 0140-7007. DOI: 10.1016/j.ijrefrig.2016.02.022 (cit. on p. 150).

[144] I. Roumeliotis and K. Mathioudakis. "Analysis of moisture condensation during air expansion in turbines." *International Journal of Refrigeration* 29(7) (2006), pp. 1092 –1099. ISSN: 0140-7007. DOI: 10.1016/j.ijrefrig.2006.03.001 (cit. on p. 150).

[145] O. Leufvén and L. Eriksson. "A surge and choke capable compressor flow model – Validation and extrapolation capability." *Control Engineering Practice* 21(12) (2013), pp. 1871 –1883. ISSN: 0967-0661. DOI: 10.1016/j.conengprac.2013.07.005 (cit. on p. 150).

[146] X.-J. Yu and B.-J. Liu. "Stereoscopic PIV measurement of unsteady flows in an axial compressor stage." *Experimental Thermal and Fluid Science* 31(8) (2007), pp. 1049 –1060. ISSN: 0894-1777. DOI: 10.1016/j.expthermflusci.2006.11.001 (cit. on p. 151).

[147] S. K. Dahikar, M. J. Sathe, and J. B. Joshi. "Investigation of flow and temperature patterns in direct contact condensation using PIV, PLIF and CFD." *Chemical Engineering Science* 65(16) (2010), pp. 4606 – 4620. ISSN: 0009-2509. DOI: 10.1016/j.ces.2010.05.004 (cit. on p. 151).

[148] C. Espinoza, M. Simmons, F. Alberini, O. Mihailova, D. Rothman, and A. Kowalski. "Flow studies in an in-line Silverson 150/250 high shear mixer using PIV." *Chemical Engineering Research and Design* (2018). ISSN: 0263-8762. DOI: 10.1016/j.cherd.2018.01.028 (cit. on p. 151).

[149] A. Darisse, J. Lemay, and A. Benaïssa. "Investigation of passive scalar mixing in a turbulent free jet using simultaneous LDV and cold wire measurements." *International Journal of Heat and Fluid Flow* 44 (2013), pp. 284 –292. ISSN: 0142-727X. DOI: 10.1016/j.ijheatfluidflow.2013.06.012 (cit. on p. 151).

[150] A. Mychkovsky, D. Rangarajan, and S. Ceccio. "LDV measurements and analysis of gas and particulate phase velocity profiles in a vertical jet plume in a 2D bubbling fluidized bed: Part I: A two-phase LDV measurement technique." *Powder Technology* 220 (2012). Selected Papers from the 2010 NETL Multiphase Flow Workshop, pp. 55 –62. ISSN: 0032-5910. DOI: 10.1016/j.powtec.2011.09.027 (cit. on p. 151).

"We can appreciate the entire journey by looking back at how far we have come."

Antichamber.